Fabrication of nc-Si Single-Junction Thin-Film Solar Cells on Flexible Aluminium Substrates

Arvind Ganesh Murali

August 2021

TU Delft

Fabrication of nc-Si Single-Junction Thin-Film Solar Cells on Flexible Aluminium Substrates

by

Arvind Ganesh Murali

to obtain the degree of Master of Science
at the Delft University of Technology,
to be defended publicly on Monday August 30, 2021 at 11:00 AM.

Student number:	5019109	
Project duration:	November 18, 2020 – August 30, 2021	
Thesis committee:	Prof. Dr. Ir. A.H.M. Smets,	PVMD, TU Delft
	Dr. Ir. A. Shekhar,	DCE&S, TU Delft
	Dr. G. Limodio,	PVMD, TU Delft

TU Delft

Preface

This thesis project marks the end of my time as a master student at TU Delft. After completing my bachelor studies in mechanical engineering in India, I choose to move to a foreign country for the first time in my life for my masters. I choose the sustainable energy technology master at TU Delft, as I wanted to contribute to the transition to renewables. I learnt a lot about renewable energy during the course of my masters and solar energy was the most fascinating source of energy for me. So, I decided to work on my thesis in this growing field.

I was having a lot of confusion picking the right thesis topic. But after having a meeting with Dr. Gianluca Limodio and Prof. Arno Smets, I wanted to be a part of the FlamingoPV projects. I am grateful for having this opportunity to learn about thin-film cells and also for the hands-on experience of developing solar cells which I could not have gained from any textbook.

First of all, I would like to thank Dr Gianluca Limodio who was my daily supervisor. He was always available on short notice, even on weekends. My apologies to him for processing thesis-related questions even when he was on holiday. I would also like to thank Prof. Arno Smets for his valuable input during the meetings and also for being open to approaching him in his office with a question. I also would like to thank him for setting up team bonding sessions with the FlamingoPV and DISCO students, which was a major stress buster during the tough COVID period.

In general, I would like to thank everyone from the PVMD and EKL groups. A special thanks to Govind Padmakumar for placing my sample holders inside the machine when I was unavailable. I would also like to thank Dr. Davide Bartesaghi and Dr. Edward Hammers from HyET solar for helping me throughout my thesis project at HyET. Moreover, I would like to thank Dr. Marlies Nijemeisland for allowing me to use the raman setup at their faculty.

Finally, I would like to thank all my family and friends who have provided me with emotional support over the last couple of years. This brings an end to my master studies and I enjoyed my time as a student at TU delft. I hope to contribute to the growing success of the PV industry from the knowledge gained through my masters.

Arvind Ganesh Murali
Delft, August 2021

Abstract

Thin-film solar cells are second-generation solar cells and they are gaining more traction than the first-generation c-Si solar cells. This is due to the advantages they have over conventional solar cells. The advantages are that they are lightweight, flexible, cheaper and also have better aesthetics than conventional solar cells. Thin-film cells are being processed on a flexible aluminium substrate at HyET Solar which is a Netherlands based company. Their processing technique involves depositing thin-film silicon solar cells on a temporary flexible aluminium substrate. The cells are laminated on a plastic carrier foil and the Al substrate is etched away.

HyET solar produces tandem and amorphous single-junction solar cells. For their tandem solar cells, the bottom layer is crystalline. Hence, single-junction crystalline silicon cells are developed at TU Delft to incorporate them into the tandem modules at HyET solar. The crystalline silicon cells deposited at TU Delft are characterized using SEM and raman. The cells deposited at Delft are processed at HyET solar and characterized.

Upon characterization, the crystalline fraction and deposition rates increase with an increase in deposition power in the intrinsic layer. The crystalline fraction and deposition rate of a cell does not change by changing the cell thickness of the i-layer. The cell characteristics also change with a change in the silane flow rate in the i-layer. The optimal deposition power with an optimal crystalline fraction was 40W and the corresponding silane flow rate was 3.3 sccm. The deposition rate for a 40W deposition power was 0.41 nm/s. Cells deposited using these parameters were then processed at HyET solar.

The cells developed at HyET Solar was shunted. The cause of the shunts was critically analyzed and depositing an amorphous n-layer with a thickness of 80nm seemed to get rid of the shunts. The JV characteristics of the cell were not significant under illumination but the cells displayed diode behaviour when measured in the dark (dark JV). All the deposition parameters except for the deposition time (thickness of deposition) have been optimized for an nc-Si single-junction cell. Further dedicated research on thin-film silicon cells can be performed to improve the electrical characteristics of the cell.

Contents

List of Figures

List of Tables

Nomenclature

Symbols

$:H$	hydrogenated
η	efficiency
$\mu - Si$	microcrystalline silicon
$°C$	degree Celsius
$a - Si$	amorphous silicon
a	amorphous
Ag	silver
Al	aluminium
B	boron
$c - Si$	crystalline silicon
C	carbon
Cd	cadmium
Cr	chromium
$e-$	electron
eV	electron volt
Ga	gallium
GW	giga watt
H	hydrogen
$i-$	intrinsic
I	current
In	indium
$In_2O_3:H$	hydrogen doped indium oxide
J	current density
KWh	kilo watt hour
MHz	mega hertz
Mo	molybdenum
Na	sodium
$nc - Si$	nanocrystalline silicon
nc	nanocrystalline

nm nanometer

O oxygen

P phosphine

P_{in} input power

rpm revolutions per minute

$sccm$ standard cubic centimeters per minute

Si Silicon

$SnO_2 : F$ fluorine doped tin oxide

Te tellurium

V voltage

Zn zinc

$ZnO : Al$ aluminium doped zinc oxide

$Zno : B$ boron doped zinc oxide

Abbreviations

AM air mass

$APCVD$ atmospheric pressure chemical vapour deposition

AZO aluminium doped zinc oxide

$CIGS$ copper, indium, gallium and selenium

CoF copper on foil

DC direct current

DPC deposition chamber

EKL else kooi laboratory

EQE external quantum efficiency

ESP electrical sustainable power

FF fill factor

$FlamingoPV$ flexible lightweight advanced materials in next generation of photovoltaics

$FTIR$ fourier transform infra-red

FTO flourine doped tin oxide

$HyET$ high yield energy technology

IPA isopropanol

IQE internal quantum efficiency

IR infra-red

LA longitudinal acoustic

$LCOE$ levelised cost of electricity

$LPCVD$ low pressure chemical vapour deposition

$MOCVD$ metal oxide chemical vapour deposition

MPP maximum power point

MST micro surface texture0

OC open circuit

$PECVD$ plasma enhanced chemical vapour deposition

PV photovoltaic

$R2R$ roll to roll

RF radio frequency

SC short circuit

SEM scanning electron microscope

TA transverse acoustic

TCO transparent conductive oxide

TO transverse optical

TU technishe Universiteit

VHF very high frequency

1

Introduction

Many worldwide issues are caused by our huge reliance on fossil fuels as a source of energy. Their unequal distribution over the globe has caused political and economic issues, as well as impeding progress and triggering (military) conflicts [1]. Furthermore, the supply of fossil fuels is finite, and even if fresh deposits are discovered, they will eventually be depleted. As a result, it is critical to replace these energy sources with other inexhaustible, widely available, affordable and safe alternatives.

The use of renewable sources of energy, for this reason, has been on the rise over the last few years. Solar energy is one of the most accessible renewable energy sources which can be converted into electricity by photovoltaic (PV) cells and its market also has been burgeoning over the last decade. The global installed capacity of PV has increased drastically over the last decade as shown in the figure 1.1. The total installed capacity of photovoltaics is around 713.97 GW in 2020 [2]. The utility-scale solar PV costs have been reduced over the last ten years and the levelised cost of electricity (LCOE) for the same is 0.127 $/kWh in the Netherlands in 2018 as shown in figure 1.2 [3]. The reduction in cost has helped the solar PV grow over the years and compete with the non-renewables which were prominent in the energy market.

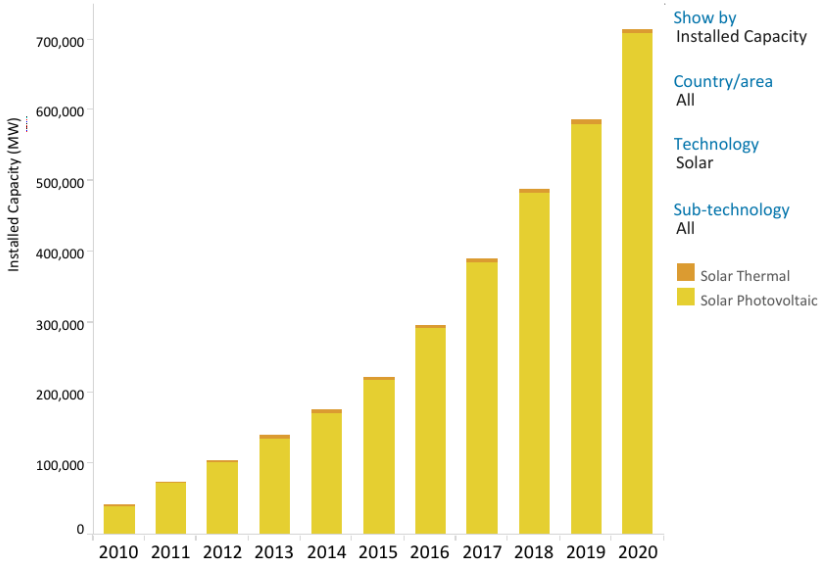

Figure 1.1: Global PV installed capacity trend over the last decade [2]

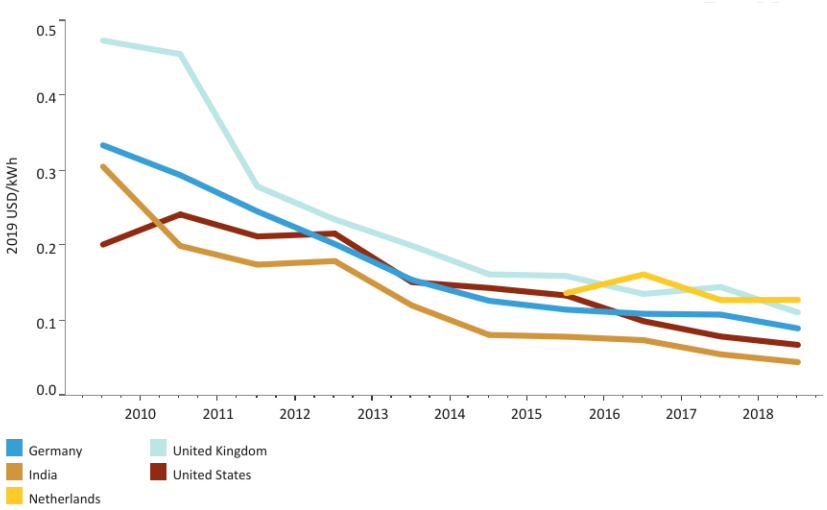

Figure 1.2: Weighted-average LCOE of utility-scale PV over the last decade by country [3]

1.1. Thin-film solar cells

Thin-film solar cells are the second-generation of solar cells and it is one of the leading technologies in the PV field. The primary concept behind thin films is to reduce the amount of material required to produce energy. The thin-film cells are also pliable and lightweight. The thickness of these cells is in the micrometer range which is far lower than the conventional solar cells.

Just like their thickness the efficiencies of thin-film cells are lower than that of first-generation solar cells [4]. Even though their efficiencies are lower there are some advantages that thin-film cells have over the first-generation cells. They are:

- As the name suggests the thin-film cells have lower material costs due to their reduced size.
- They have a lower environmental impact since they require less silicon.
- Thin-film cells are deposited using plasma-enhanced chemical vapour deposition (PECVD). This process is faster and cheaper than the production process for first-generation cells.
- Does not require mounting systems to install the cells and hence the installation costs are also lower.
- Its flexibility and lightweight makes it easier to integrate the cells in buildings (Building-integrated photovoltaics). The aesthetically pleasing nature of the thin films also is an added advantage.
- Thin-film modules are not influenced by the temperature as much as the conventional solar cells. The first-generation solar cells drop in performance above 25°C [5].

1.2. FlamingoPV (Flexible Lightweight Advanced Materials In Next Generation Of PhotoVoltaics) project

FlamingoPV projects stand for Flexible lightweight advanced materials in the next generation of photovoltaics. This is a project undertaken by TU Delft in association with HyET solar. HyET solar is a company in the Netherlands that produce flexible thin-film solar cells. They currently produce tandem and amorphous silicon modules. Their current amorphous silicon modules have an efficiency of 7%.

Here at the TU Delft, there are excellent facilities in the else kooi laboratory (EKL) to produce amorphous and nanocrystalline silicon solar cells. There have been several groundbreaking research that has been done in the EKL which makes TU Delft the perfect partner for HyET solar. The goal of this research in TU delft is to implement the findings to the HyET solar production process.

The aim of the FlamingoPV projects is to improve the efficiency and production time of the thin-film solar cells and implement them into the HyET solar production process. The work undertaken at EKL and HyET by the students for the FlamingoPV projects is done under the supervision of Dr. Gianluca Limodio and Dr.Ir. Arno Smets.

HyET solar uses Aluminium as their substrates and hence the cells are deposited on the same. The Aluminium substrates are provided by HyET solar which are cut into 10 ×10 cm^2 pieces. Various experiments and research on the transparent conductive oxide (TCO), tandem, triple junctions, amorphous and nanocrystalline single-junction cells are carried out on those substrates. First, the TCO which is aluminium-doped zinc oxide (AZO) is deposited on the substrate. The TCO adopts the micro-sized features of the substrate and has a good micro surface texture (MST) for efficient light trapping. Then the active layers are deposited in p-i-n configuration on the same. Then the final processing of the cell is done which includes: laser scribing then back contact sputtering, annealing and etching.

Then the results from the characterization of the cells are to be integrated into the a-Si/nc-Si tandem solar cells which are being produced at HyET solar.

1.3. HyET solar production process

HyET solar is a company based in Arnhem, Netherlands. They were founded in 2012 and they produce thin-film a-Si single-junction and tandem solar cells. They use a special roll to roll (R2R) production process to produce the cells.

Aluminium foils are used as temporary substrates, which are passed through deposition chambers in the R2R process. These processes are automated and homogeneous depositions are made continuously by just supplying new aluminium foils. Aluminium foils are used as the substrate as they are suitable for high process temperatures required to deposit high-quality TCOs. The TCO which is Fluorine-doped Tin Oxide (FTO) is deposited on the aluminium substrate using atmospheric pressure chemical vapour deposition (APCVD) at high temperatures between 500°C and 550°C. Deposition rates up to 100nm/s are achieved and the TCO is homogeneously deposited. Then the silicon layers are deposited in p-i-n superstrate configuration using plasma-enhanced chemical vapour deposition (PECVD). These depositions are done at a radio frequency (RF) of 13.5 MHz and substrate temperature may reach up to 200°C [6]. Currently, HyET solar produces single-junction a-Si and a-si/µc-Si tandem solar cells in the configuration mentioned above.

After deposition, laser scribing (P1 P2) is done to define the active area. After this, a TCO fill ink is poured at the scribes to insulate the active layers. The back contact (AZO) is then sputtered in the R2R system using a DC magnetron sputtering system. The TCO filler ink is then removed to set apart the back contact. Then the cell is laminated on the back contact surface by using an adhesive and a mechanical press to completely laminate it. The temporary aluminium substrate is then removed by wet chemical etching. Finally, the polymer encapsulation is done before making the bus bar connection [6]. This can be better understood from the figure 1.3.

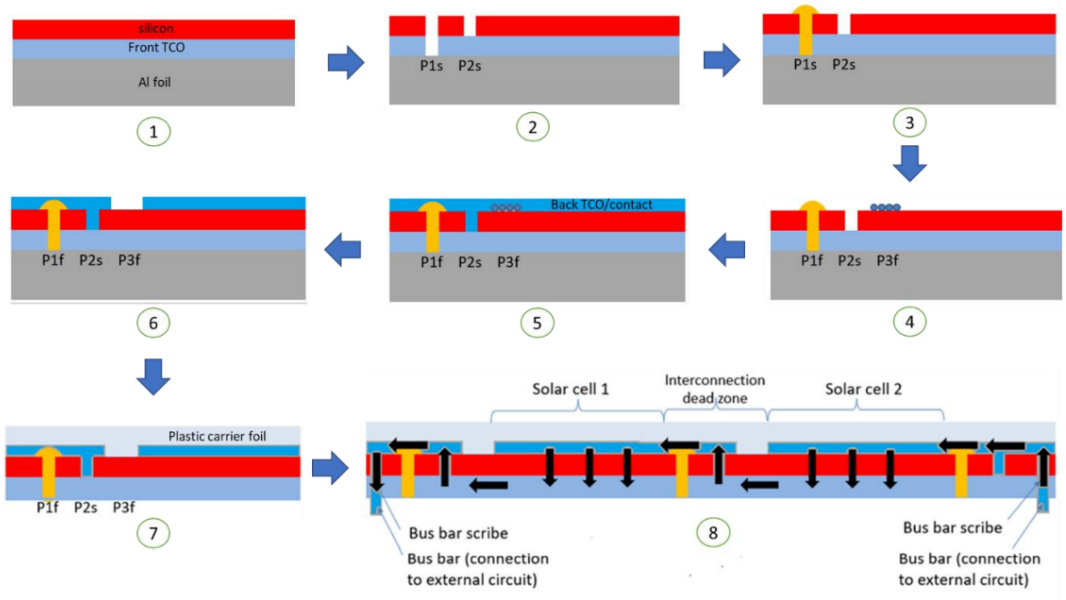

Figure 1.3: The R2R production process at HyET solar [7]

2

Aim and outline

The aim and the outline of the thesis include optimizing the deposition conditions for the deposition of single-junction nanocrystalline silicon thin-film solar cells on flexible aluminium substrates. This also would help HyET solar in the future with their roll-to-roll production of tandem and triple junction cells. Some of the research questions that will be answered in this thesis are:

- Does the cell characteristics change for a change in deposition power in the intrinsic layer and what is the optimal deposition power?
- Does the cell characteristics change with the thickness of the intrinsic layer for the same deposition power?
- Does the cell characteristics change by varying the silane flow rate in the intrinsic layer?
- Can nc-Si single-junction cells be processed using HyET Solar processing technique?
- What would be the optimal deposition time and thickness for the intrinsic crystalline silicon?

Now that the reader has been introduced to the scope of the project, chapter 3 reviews the current thin-film technologies available in the market. In chapter 4, the machines used for the fabrication of nc-Si single-junction solar cells are discussed. In chapter 5, a detailed explanation of the steps taken to develop thin-film cells and the results obtained are discussed. This is followed by a short conclusion of this thesis work and recommendations for future research on nc-Si single-junction thin-film solar cells on flexible Al substrates.

3

Review of thin-film solar cells

The basic principle underlying thin-film solar cells is similar to first-generation solar cells. In this chapter, the thin-film solar cell properties are reviewed and the current technologies in thin-film production are discussed.

3.1. Crystalline and amorphous silicon

If we look at a crystalline silicon lattice, the arrangement of the atoms is repetitive. This indicates the long-range order and symmetry of the lattice. This lattice arrangement can be differentiated as monocrystalline silicon or multicrystalline silicon. The monocrystalline silicon structure is repetitive or continuous. The monocrystalline silicon cells are unbroken with no grain boundaries in the bulk and its edges. Unlike monocrystalline silicon, multicrystalline silicon which is also known as polycrystalline silicon structure has some grain boundaries. The grain boundaries make the multicrystalline silicon lattice-mismatched and lead to several defects at the grain boundary. Due to these defects, the charge-carrier lifetime of multicrystalline silicon is lower than that of monocrystalline silicon. The larger the charge-carrier lifetime, the larger the band gap utilization and larger will be the open-circuit voltage of the cell. Since the monocrystalline silicon has no grain boundaries the charge-carrier lifetime is larger and high open-circuit voltages can be achieved as well [8]. The mono and multicrystalline structure can be further understood from figure 3.1 shown below.

Crystalline silicon is an indirect bandgap material that requires a change in momentum or energy to excite an electron from its valence band to the conduction band. The bandgap of crystalline silicon is 1.012 eV. This shows that it has a low absorption coefficient and requires the light to penetrate deeper into the silicon wafer for the electron-hole recombination which is caused by the absorption of photons.

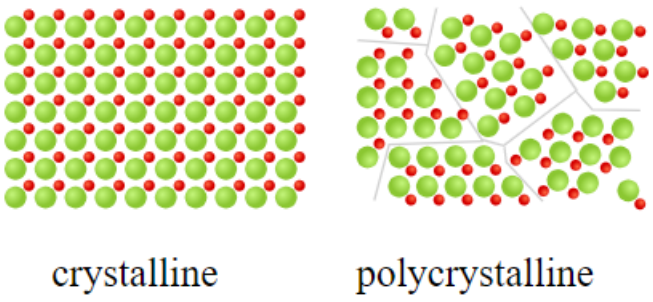

Figure 3.1: The monocrystalline cell lattice is shown on the left and the multicrystalline cell lattice is on the left [9]

Therefore, to absorb at least 90% of the photons, the crystalline silicon cells must be at least 230 µm thick [8]. In practice, this thickness can be reduced by inducing surface textures and good back contact to increase the optical path length of light inside the cell.

In contrast to crystalline silicon, the amorphous silicon cell structure is not repetitive. It does not have a long-range order nor is it symmetrical as shown below in the figure 3.2. All the silicon atoms are not bonded together and they have many dangling bonds and defects. The amorphous silicon has to be passivated with hydrogen atoms (a-Si:H) before using them in solar cells as it reduces the defects. The amorphous silicon is a direct bandgap material with a bandgap between 1.6 and 1.8 eV. Since they are direct bandgap material, they do not need external force or momentum to move an electron from the valence to the conduction band, unlike crystalline silicon cells. Therefore, the absorption coefficient of a-Si is more than that of crystalline silicon in the visible spectrum. Since their absorption coefficient is larger, thinner amorphous wafers can absorb similar spectra compared to the thicker crystalline wafers which are required [8].

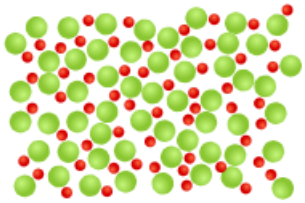

Figure 3.2: Amorphous silicon cell lattice [9]

The crystalline fraction in a silicon wafer can be varied by changing the deposition conditions. This is done by changing the silane concentration in the source gas mixture [10]. This was observed when changing the silane concentration from 2%-10%. The cells were initially in the crystalline phase with no grain boundaries and as the concentration reached up to 6%-10% the grain boundaries started appearing which indicated the amorphous phase. This transition process is shown below in the figure 3.3. The amorphous phase obtained is not the hydrogenated a-Si:H used in the solar cells, but the formation of these grain boundaries will affect the optical and electrical properties of the cell [11]. The best nanocrystalline silicon cell in practice has a lattice similar to that of an amorphous-crystalline silicon lattice in the transition phase with a crystalline fraction close to 60% [8]. This shows that the nanocrystalline crystalline silicon cell is a mixed phase material. More information on how the crystalline fraction is calculated using raman spectroscopy is further explained in the section 4.4.

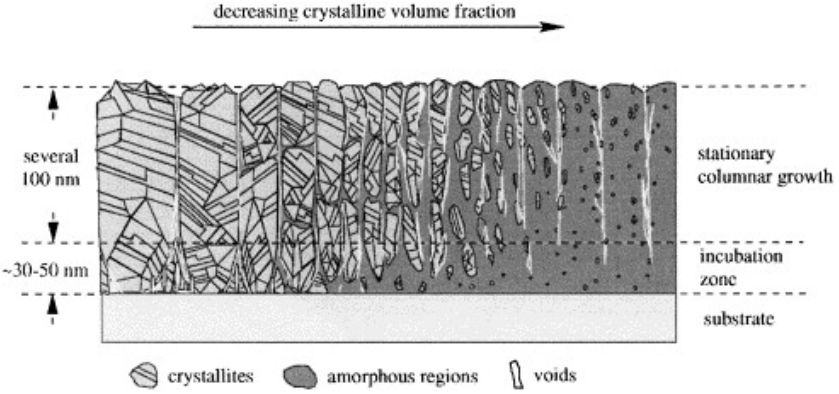

Figure 3.3: Phases of thin-film silicon with the crystalline structure on the left and amorphous on the right [11]

3.2. Hydrogenated nanocrystalline silicon solar cell

The current research in nanocrystalline cells is mainly directed towards improving the reliability of the cell over light-induced degradation and increasing their spectral response beyond the infrared range. The micro or nanocrystalline silicon cells are now majorly used as bottom cells in tandem and triple-junction solar cells. Studying and improving the properties of the crystalline silicon cells and implementing them on the tandem and triple junction cells is important. There are different layers in an nc-Si:H single-junction cell. The properties of these layers are discussed in detail below.

3.2.1. TCO properties

The working of the nanocrystalline silicon single-junction cells is similar to the other single-junction cells. The light first enters the cells through the TCO which is abbreviated as transparent conductive oxide which acts as the front contact of the cell. The front TCO is effectively used to couple light onto the active layers through the p-layer. The front TCO is textured accordingly to scatter light to increase the average path length of the photon [8]. Increasing the path length also increases the absorption in the absorber layer and hence the efficiency. The TCOs are also transparent in the visible spectrum and hence they are used as the topmost layer of the cell. They also have very good electrical properties such as good electrical conductivity and their general operation is similar to that of semiconductors [12]. TCOs are also used as back contacts or back reflectors with a metal (generally Ag or Al).

The TCOs need to be designed effectively to improve the efficiency of the cells. Hence most commonly used TCO materials at the moment are fluorine-doped tin oxide (SnO_2:F, FTO), aluminium-doped zinc oxide (ZnO:Al, AZO), hydrogen-doped indium oxide (In_2O_3:H), boron-doped zinc oxide (ZnO:B) and indium tin oxide [8]. The TCO is generally deposited using atmospheric pressure chemical vapour deposition (APCVD), sputtering , low-pressure chemical vapour deposition (LPCVD) or metal-organic chemical vapour deposition (MO CVD). The TCO material needs to be highly transparent and conductive. The material which has the best trade-off between transparency and conductivity was found out to be indium tin oxide [13]. Since indium is a rare earth metal, it is very costly and is not abundantly available. The most abundantly available TCO materials with a good trade-off between transparency and conductivity, which are commonly used in practice are FTO and AZO [8].

3.2.2. P-i-n layer properties

The p, i and n layers are the most important part of the cell. In a nanocrystalline silicon solar cell, the p-layer is the first doped layer after the front contact. The light that enters the p-layer does not absorb the light and manages to transmit most of the light onto the intrinsic layer [14]. For that, the p-layer should have a wide bandgap and a very thin layer. The thin layers reduce the series resistance required to absorb the light to transmit most of them to the intrinsic layer. High conductivity of the layer also leads to lower series resistance. After the p-layer the light enters the absorber layer where the collection and separation of charge carriers take place. The absorber layer is intrinsic in this case. After the absorber layer, the n-layer is deposited. The n-layers also must be highly conductive to obtain solar cells with high fill factors and efficiencies [14].

The light enters the cell through the TCO which directs the light onto the active layers. The p-layer is highly conductive and do not absorb most of the light. The carrier separation and generation from the incident light then takes place at the intrinsic absorber layer. This happens due to the internal electric field in the cell caused due to the built-in potential between the doped p and n-layers. Since they are thin-film cells, the lifetime of photogenerated carriers and drift length are low. The high lifetime and drift length of these carriers lead to better absorption of the light spectrum. These are enhanced by the TCOs at the front and back contact [14].

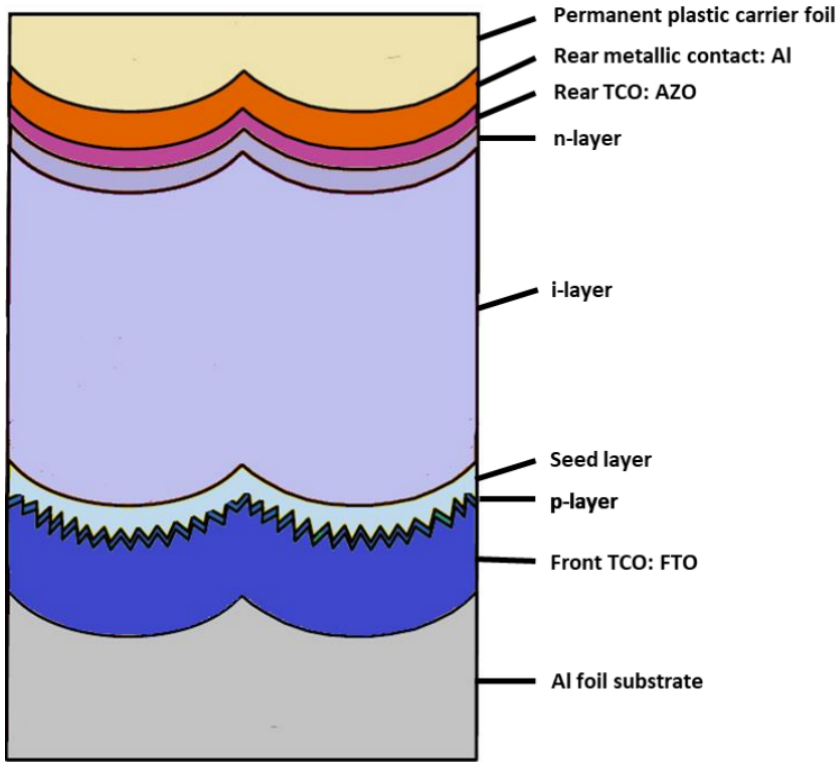

Figure 3.4: Different layers in a nanocrystalline silicon thin-film cell [15]

3.3. Cell configurations

The nanocrystalline single junction cells have different configurations. The cells are deposited on a substrate (Aluminium in this case). First, a front TCO is deposited on top of the Al substrate. The TCO which HyET incorporates is FTO, since APCVD is unavailable at the EKL facility, AZO sputtered on top of the Al substrate which acts as the front TCO. Then a 16 nm thick p-layer (p-nc-SiO_x:H) is deposited. The front TCO and the p-layer do not absorb the light intended for the absorber layer. After these layers, a (i-nc-Si:H) intrinsic layer with thickness around 0.5 µm to 2.5 µm is deposited. Then an n-layer (n-a-SiO_x:H or n-nc-SiO_x:H) is deposited. The n-layer thicknesses are also in the nanometer range. An 80nm thick AZO is sputtered on top of the n-layer which acts as the back TCO. That is followed by a 300nm thick Al back contact. The different layers in a nanocrystalline silicon cell deposited is shown in figure 3.4.

The nanocrystalline silicon cells can be deposited in two different configurations. The two configurations are namely substrate and superstrate configurations. In superstrate configuration, firstly, the front TCO is deposited on a substrate such as glass through which the light enters the cell. Later the p-i-n layers are deposited and then the back TCO and the back contacts are deposited. In the superstrate configuration, a good p-i layer interface is required to grow high-quality nc-Si cells. A good p-i layer interface helps in hole collection. Electrons have a higher charge carrier lifetime and mobility than holes. So, the presence of any defects in the p-i interface may lead to recombination of the holes and carriers before the charge carrier collection in the absorber layer. Hence a good p-i interface is required for a cell deposited in superstate configuration. This deposition is quite challenging. Hence, a seed layer is generally deposited after the p-layer to improve the p-i layer interface. The seed layers in some cases are also integrated with the p-layer. The difficulty in depositing a high-quality p-i interface in superstrate configuration arises due to texturing of the substrate. In HyET solar the cells are deposited in the superstrate configuration but depositions are performed on a temporary Al substrate which is etched away. Aluminium is used as the temporary substrate since they are sturdy and can withstand high-temperature depositions. The deposition carried out at HyET using the temporary superstrate has the following configuration as shown in figure 3.5a.

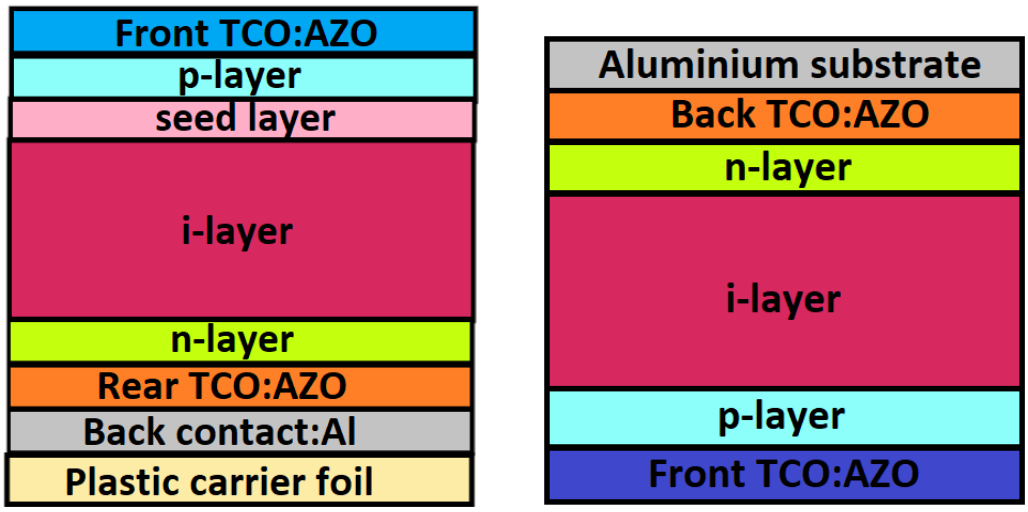

(a) Superstrate layer configuration followed by HyET

(b) Substrate layer configuration

Figure 3.5: Superstrate and substrate layer configuration

The other cell configuration is the substrate configuration. In the substrate configuration, the back TCO is deposited first after which the n-i-p layers are deposited respectively. The front TCO and front contacts are deposited after the silicon layers. The substrate acts as the back contact in this configuration. The p-layer is deposited after the i-layer. Hence, the cells in substrate configurations have a good p-i layer interface. The substrate configuration can be better understood from the figure 3.5b.

3.4. Current thin-film technologies

Thin-film silicon solar cells are the second-generation of solar cells. The thin films became popular as early as the 1970s. Thin-film chips were used in solar calculators from that period. The doped µc-Si:H was first deposited by Usui and Kikichi in 1979 [16]. Ever since, thin-film technologies have seen massive growth. There are various thin-film technologies that are under research at the moment. But the most commonly used thin-film technologies include cadmium telluride (CdTe), copper indium gallium selenide (CIGS) and the a-Si/µc-Si tandem cells.

CdTe cells are the second most commonly used thin-film material after silicon. It contributes to around 5% of the world market [17]. CdTe cells can be produced faster and cheaper than crystalline silicon cells making them a very good alternative. Cadmium is abundant in nature. It is a byproduct of mining, but Tellurium is a rare earth metal that makes it difficult to produce in large quantities. The CdTe is a II-IV semiconductor material where every Cd atom is connected to four Te atoms and vice versa in the zincblende lattice structure of CdTe [17]. CdTe cells are deposited using the closed-space sublimation method. The CdTe cells are deposited in the following manner as shown in the figure 3.6a. The TCO is deposited on a glass substrate after which the n-layer CdS is deposited. Then a p-CdTe layer is deposited and its thickness is usually in the micrometre range. The back layer is deposited on top of aluminium or molybdenum. CdTe is a direct bandgap material with a bandgap of around 1.4-1.5 eV [17]. This is almost the optimum bandgap for converting the photons to electricity making it better than that of silicon. The record efficiency of the lab scale CdTe solar cells is around 22.1% produced by the American company first solar [17]. The CdTe also has its disadvantages. Tellurium is a rare earth metal, increasing its cost of production. Also, the Cd is toxic and has to be controlled during its production.

CIGS solar cells are also one of the most used alternatives to silicon in PV modules. CIGS cells contain chalcogen anions namely copper, indium, gallium and selenium, All the anions are from group 6. They also act as semiconductors. CIGS is also direct bandgap material like CdTe with a bandgap around 1-1.7 µm. Since they are direct bandgap materials, they have a very high absorption coefficient.

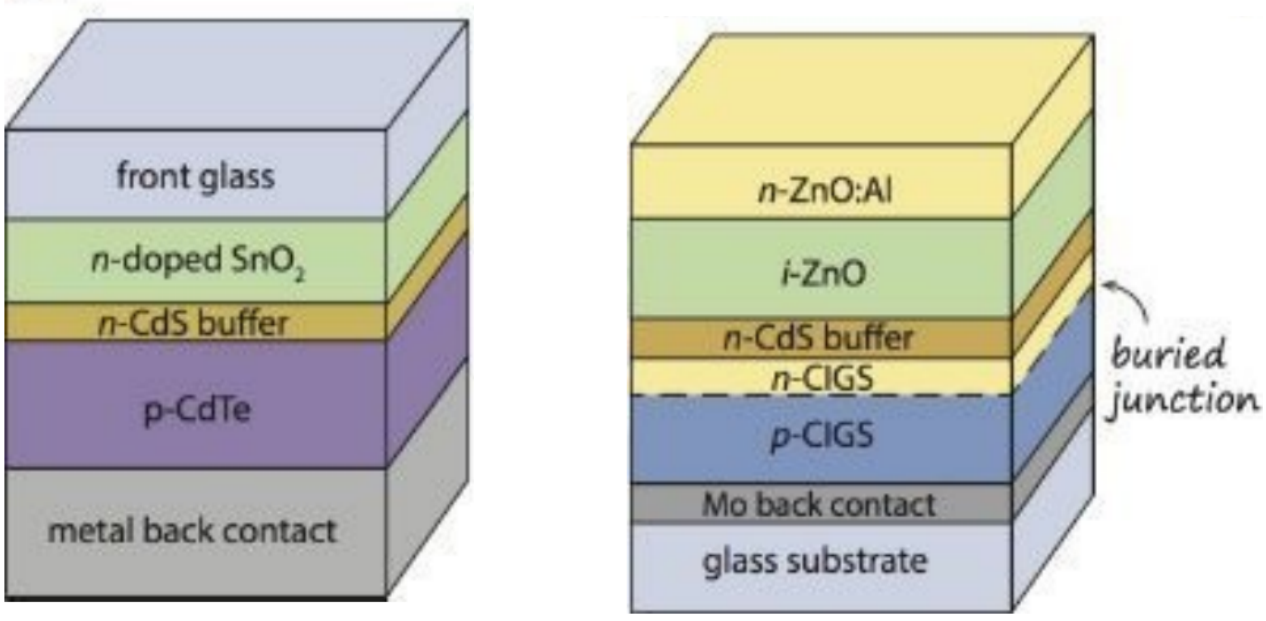

(a) CdTe cells [8] (b) CIGS cells [8]

Figure 3.6: CdTe and CIGS layer structures [8]

CIGS cells are usually deposited on a soda-lime glass substrate and then a molybdenum back contact is deposited on it. The sodium from the soda-lime substrate travels through the Mo layer onto the p-layer. This is done so that the sodium can passivate the grain boundary defects [18]. The p and n layers are deposited using 3 stage evaporation. The cells structure of the CIGS cells is shown in figure 3.6b. The record efficiency for the current CIGS thin-film cells is around 23.35%. These cells were deposited with an area of 1 cm^2 and they are produced by solar frontier [19]. CIGS also has its disadvantages. The effect of Ga and Na concentration is still under research. So, the reasoning behind lower efficiencies with higher Ga concentration is still a mystery.

Apart from the CdTe and CIGS the most commonly used thin-film material is silicon. The most important silicon cells are the a-Si modules. The properties of the same were discussed above in the section 3.1. The record efficiency of a-Si cells is 10.26% which was developed at Jülich Forschungszentrum [20].The layer structure for the same is shown in the figure 3.7a. The record efficiencies of a-Si cells produced on Al substrate at HyET is at 7%. In 1996, the Université de Neuchâtel developed the first solar cells constructed entirely of thin-film nanocrystalline layers with an efficiency of more than 7% [21]. The substrate and superstrate-type cells were constructed and both of them had an efficiency of 7%. After this most of the research in the nc-Si cells have been on improving the cell characteristics to integrate them in tandem or triple junction cells. The record efficiencies of a-Si/µ-Si micromorph cells is at 12.6% which was again produced at Université de Neuchâtel as well [22]. The cell structure of the record efficiency cell is as shown in the figure 3.7b. The record efficiency of the micromorph tandem cells produced at HyET is at 10.9%.

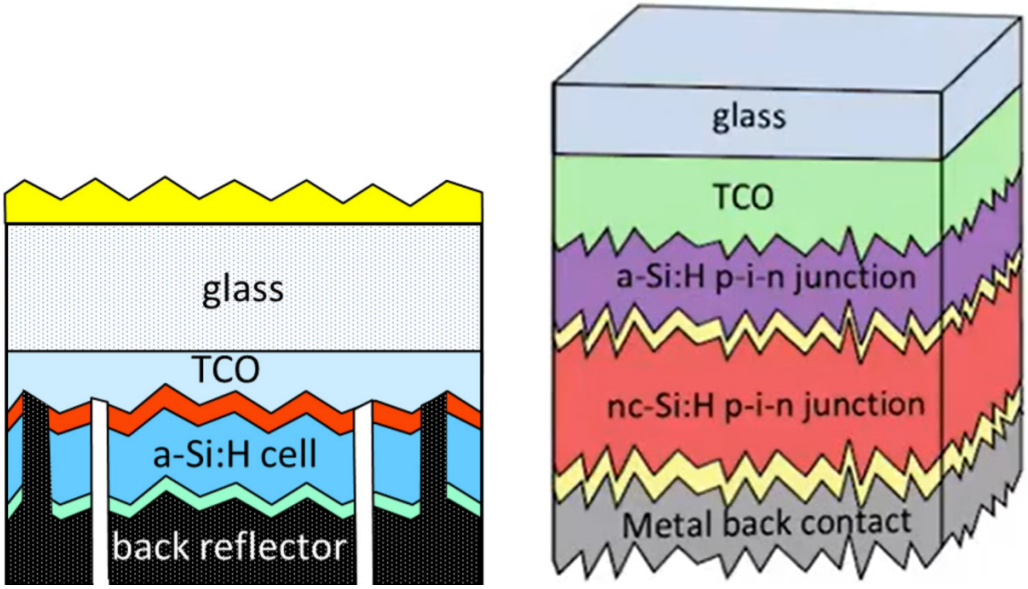

(a) a-Si thin film cell [20]

(b) Micromorph thin film cell [23]

Figure 3.7: The layer structure of the record a-Si and micromorph cells produced

4

Experimental methods

In this chapter, various equipment used at EKL and HyET is listed below. The working principle and working parameters of all the deposition and characterization equipment are also discussed in this chapter.

4.1. Plasma enhanced chemical vapour deposition

It is one of the important processes which are used for thin film deposition. It is one of the fastest technologies used to deposit thin-film silicon. PECVD is also used at TU Delft and HyET to deposit amorphous and crystalline silicon. The PECVD as the name suggests uses plasma from the ionized source gases for its operation. For the p-doped layers, diborane (B_2H_6) is mixed in the source gas for its deposition. Similarly, for n-doped layers phosphine (PH_3) is used. In addition to these chemicals, carbon dioxide (CO_2) and methane (CH_4) are used to deposit the nc-SiO_x:H layers. The source gases used for depositing the i-layers are silane (SiH_4) and hydrogen (H_2).

Coming to its operation, a very high frequency (VHF) generator is used to create a plasma between the electrodes in the deposition chamber. The ions and free radicals generated in the plasma are propelled towards the substrate. When they come in contact with the substrate the deposition on the substrate takes place and the layers are formed [24]. Although the reactions are performed under vacuum the deposition conditions can be controlled [25]. For example, chamber pressure, power, gas flow rate can be played with to optimize the deposition. The figure 4.1 shows a schematic diagram of a typical PECVD chamber used at TU Delft.

The PECVD process offers many advantages. It is one of the fastest deposition techniques. The depositions are good and uniform. The depositions have less porosity and also the depositions offer good adhesion with the substrate. Another advantage of PECVD is that it can be operated at lower temperatures than the other deposition techniques. Controlling the PECVD process parameters can enable the user to customize the cell according to the needs of the user. Optical, electrical and mechanical properties can also be customized [26]. It also produces some toxic byproducts during production which is a disadvantage. Another disadvantage is that it is not cheap.

The PECVD equipment at the EKL at TU Delft is named AMIGO. This machine has 6 different deposition chambers. The 6 deposition chambers are namely DPC1, DPC2, DPC3, DPC4, DPC5 and DPC6. In DPC1, the p-layer is deposited, DPC2 is for n-doped layers, DPC3 for amorphous intrinsic layers, DPC4 for crystalline intrinsic layers, DPC5 is for a-SiGe:H and Ar plasma treatment and in DPC6 the front TCO is sputtered using RF magnetron sputtering. This machine can be operated manually and the processes can also be automated. This automation can be done by making changes to an excel file that contains different time-controlled steps in each row with different deposition parameters in each column. This excel file can be altered to make a robot arm move the samples to the different chambers and also is used to set the deposition parameters for the respective chamber. Automation saves a lot of time as manually doing these processes will be a huge task and time consuming. The

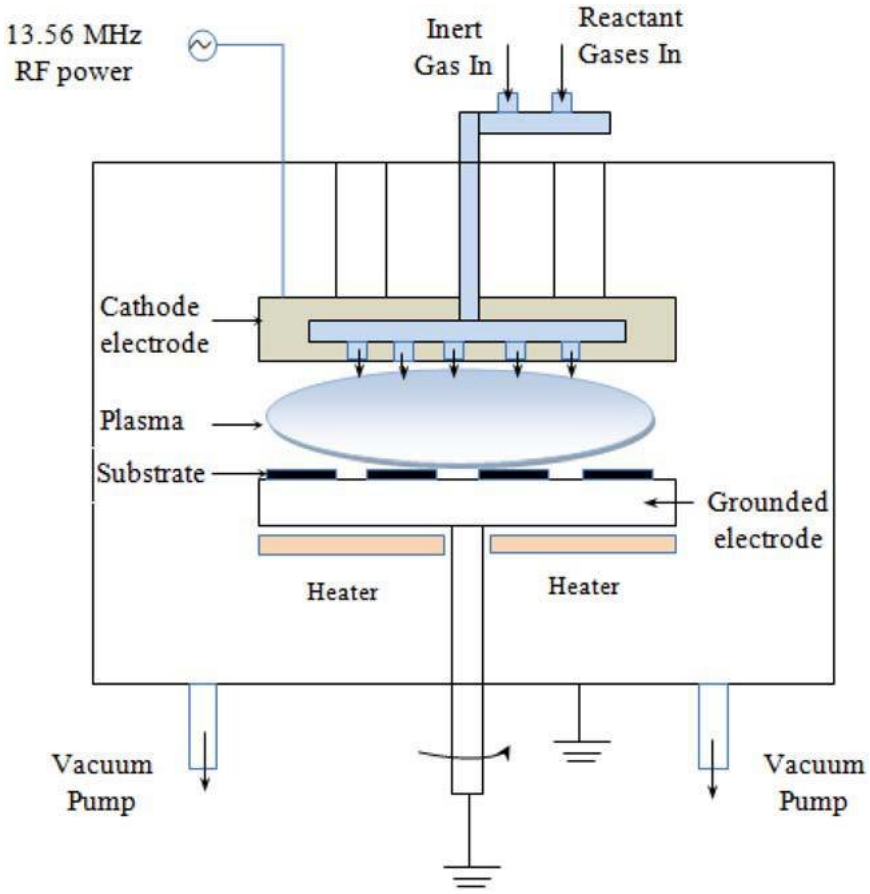

Figure 4.1: Schematic diagram of PECVD chamber [30]

load and tune capacitor values are important and they vary according to power, pressure and flow rate. The load and tune capacitors have to be set at the right value to obtain the desired deposition [27]. If the load and tune capacitors values are not optimized, the PECVD tool will have a high reflected RF power during deposition, which will affect the deposition on the sample [28]. In extreme cases, the plasma will not get ignited for deposition if the load and tune capacitors are not set at the right value.

The important deposition parameters that can be changed for improving the deposition are:

- **Gas flow rate:** The gas flow rate determines the volume of gas delivered to the plasma chamber. This can be varied to deposit different cells structures. For example, the silane concentration when higher than the hydrogen concentration would lead to amorphous silicon layer formation.

- **Deposition power:** This power is generated by the VHF generator. It is used to create the plasma required. Higher deposition power would lead to a higher deposition rate [28]. But at high power of deposition, there is higher ion bombardment on the substrate which would damage the surface [29].

- **Deposition pressure:** Varying the deposition power would lead to different materials being deposited. Increasing the pressure would decrease the ion energy. This would lead to non-existent or minimal deposition on the substrate [28]. Lower pressures also have a negative effect on the deposition. Hence a chamber pressure of 4 mbar is used to deposit the i-nc-Si:H on the Al substrate. This is considered the optimum and is followed throughout this thesis.

- **Deposition temperature:** Changing the deposition temperature also affects the deposition like the deposition pressure. A deposition temperature of 140°C is used throughout this thesis.

4.2. RF Magnetron sputtering

RF magnetron sputtering technique is used to deposit high-quality AZO as front TCO. This process is carried out in the DPC6 chamber of the AMIGO machine at EKL. Sputtering is a physical vapour deposition process. The sputtering in AMIGO for AZO takes place at an RF power of 13.56 MHz. As shown in the figure 4.2 the chamber has 2 parallel electrodes. The substrate is placed on one grounded electrode and the target ions are at the other electrode. For AZO the target ions are ZnO and Al_2O_3 at a 98:2 ratio respectively. The purity of these ions is 99.9%. The RF generator exerts an alternating electric field between the target and the electrode. This ionizes the inert gas [31]. The inert gas in this case is argon. The positive argon ions are propelled towards the substrate as a consequence, where they sputter the species from the target. As the name suggests a magnetic field is also applied during the process. This magnetic field is perpendicular to the electric field. As a result, the ion-current density increases as the magnetic field traps the electrons from bombarding the substrate [32]. Since the APCVD equipment is unavailable at the EKL the RF magnetron sputtering is used to deposit the front TCO which is AZO.

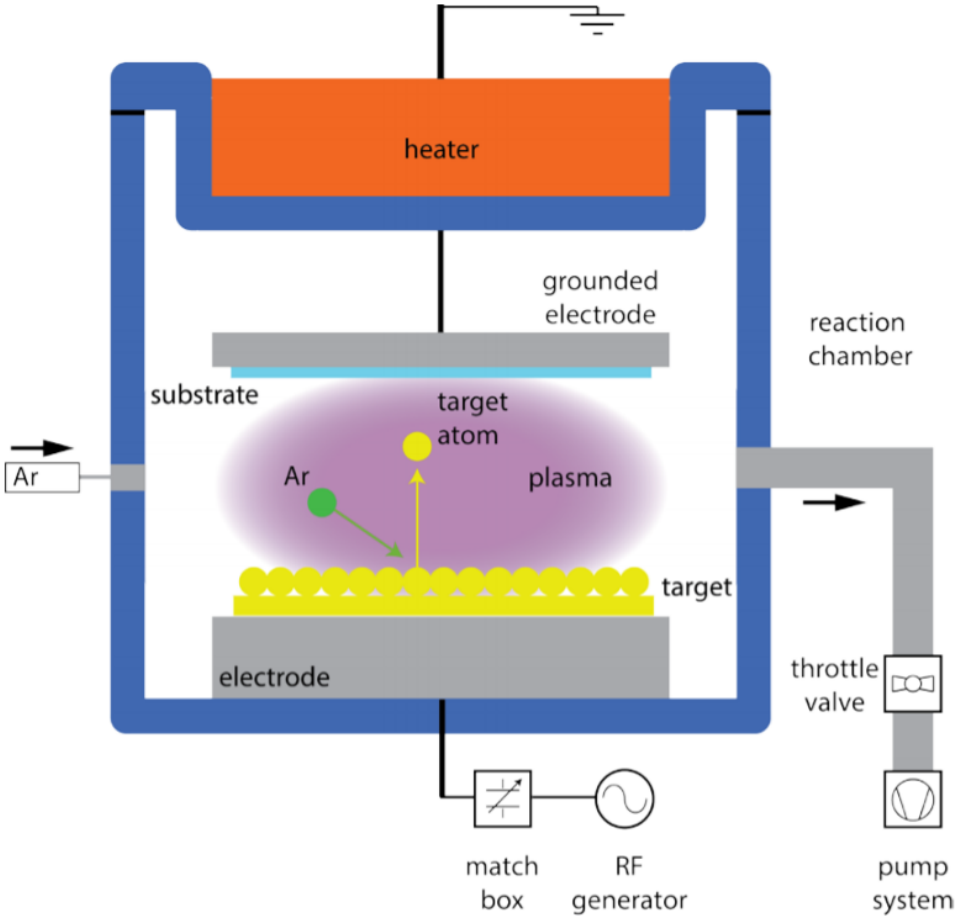

Figure 4.2: Schematic diagram of RF magnetron sputtering [32]

4.3. Metal evaporation

The back reflector is usually deposited at HyET using the sputtering machine. Since that equipment is not frequently available and easily accessible there is an alternative for depositing the Al back contact

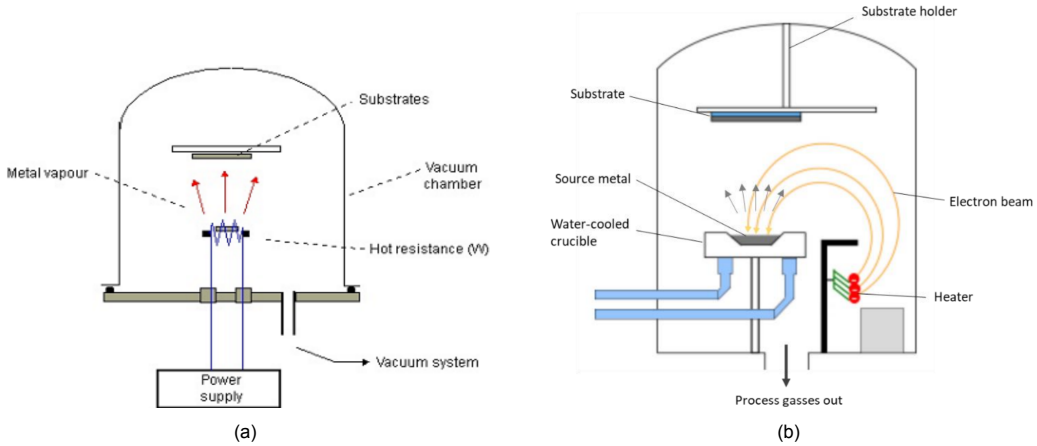

Figure 4.3: Schematic diagram of (a) thermal evaporation and (b) e-beam evaporation [32]

at the EKL. This setup is named PROVAC PRO500S and the process can be automated to achieve the desired deposition rates and thickness.

The deposition on the back reflector is performed using two types of metal evaporation. They are namely thermal and electron beam evaporation (e-beam). This evaporation is a physical vapour deposition technique. The principle behind these techniques is similar where the material is heated and is evaporated to get deposited onto the cold substrate. In the thermal evaporation technique, an electric current is supplied to a metallic boat. This metallic boat contains the metal to be deposited as the back reflector (Ag). The electric current warms up the metallic boat to its evaporation temperature. The evaporated back contact material is deposited on the cold substrate. This process is limited by the melting point of the filament [33]. Hence, very high temperatures of evaporation cannot be reached [32]. Usually, Ag is deposited using this technique. However, the e-beam process is not limited by temperature. Instead of a metallic boat, a crucible contains the evaporant (Al,Cr). This crucible is heated up by a magnetically focused high energy electron beam [32]. Similarly, the evaporated metal is deposited onto the cold substrate. The deposition chamber is under high vacuum. This reduces the risk of contamination from other substances in the air and also increases the mean free path of the electrons [32]. A schematic diagram of both thermal and e-beam evaporation is shown in the figure 4.3.

4.4. Raman spectroscopy

The raman spectroscopy is also used to characterize solar cells. This equipment was named after the famous Indian scientist CV Raman. He discovered the raman scattering effect and hence it was named after him. This spectroscopy technique works on inelastic scattering. As shown in figure 4.4, a monochromatic light source usually a laser light is focused on the cell. These photons from the laser upon interaction with the valence electrons in the cell scatters the light. This scattered light can either be scattered elastically or in-elastically. The wavelength or frequency of the inelastically scattered light is similar to the incident light. This is also called Rayleigh scattering. However, inelastic scattering occurs when the wavelength of the scattered light is lower or higher than that of the incident light. The vibrational energy of the bonds between atoms in the structure, also known as phonons, causes this change. The scattered light with higher energy than the incident light is called the stoke peak. While the scattered light with lower energy than the incident light is the anti-stokes peak. This inelastically scattered light is collected in a spectrometer while the elastically scattered light is filtered out by the notch filter. This light collected at the spectrometer is used to characterize the cells [14].

The raman spectroscopy measurements were made with a Renishaw Invia Reflex at the ESP lab, material physics lab and Kavli nano lab (Fig 4.5). The spectroscopy setups contain a green laser (514 nm) with a 180 °backscattering geometry. The red laser (633 nm) is available but is under repair. Having

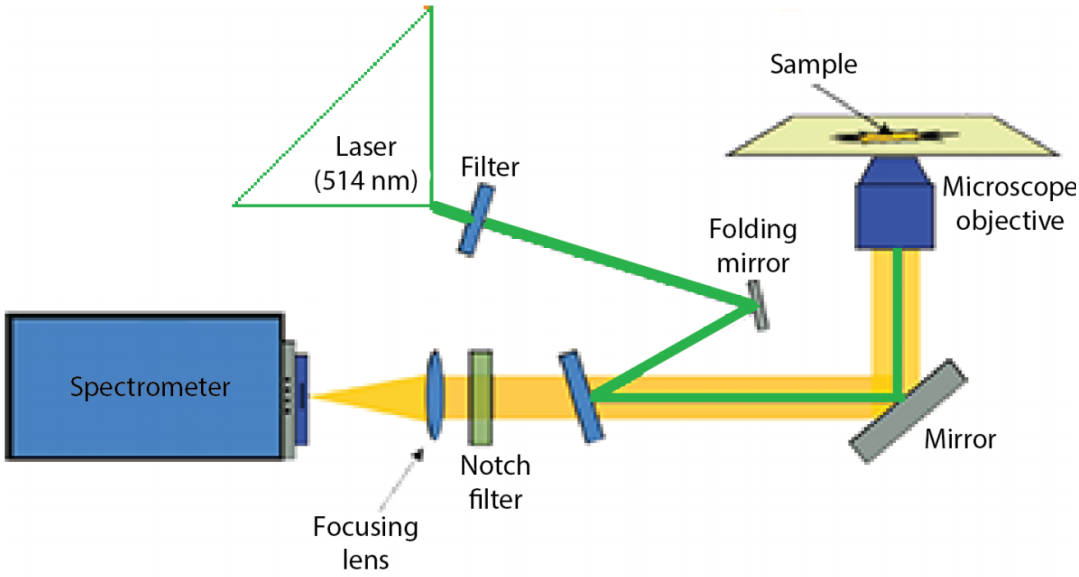

Figure 4.4: Schematic diagram of raman spectroscopy setup [32]

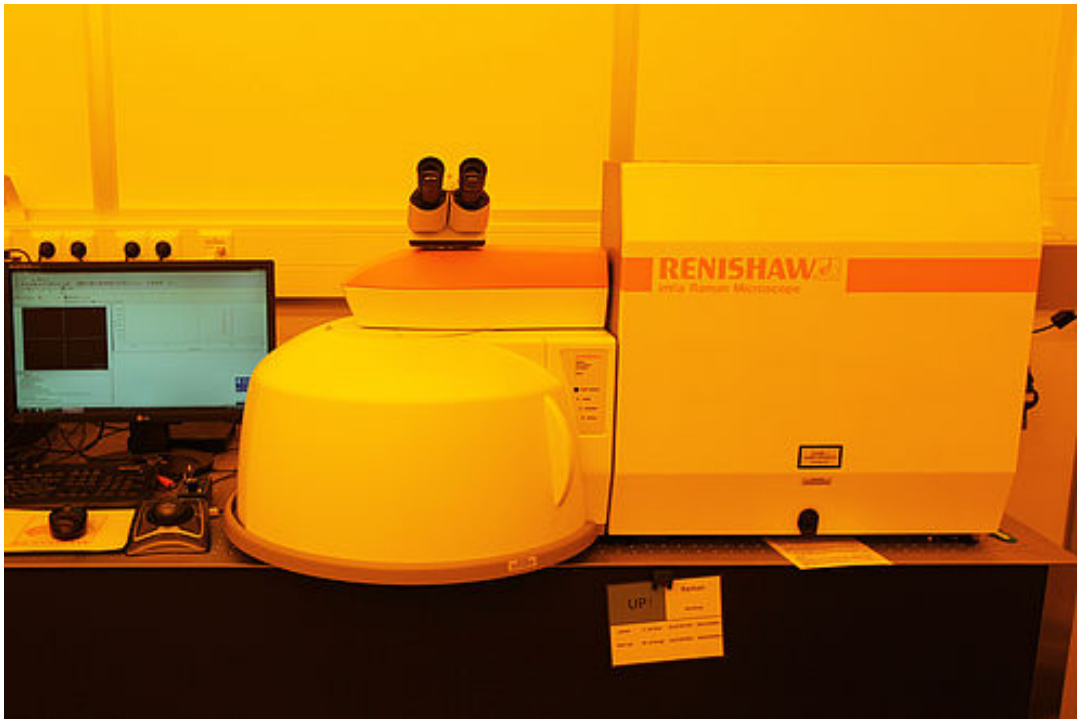

Figure 4.5: Raman spectroscopy setup at Kavli Nanolab

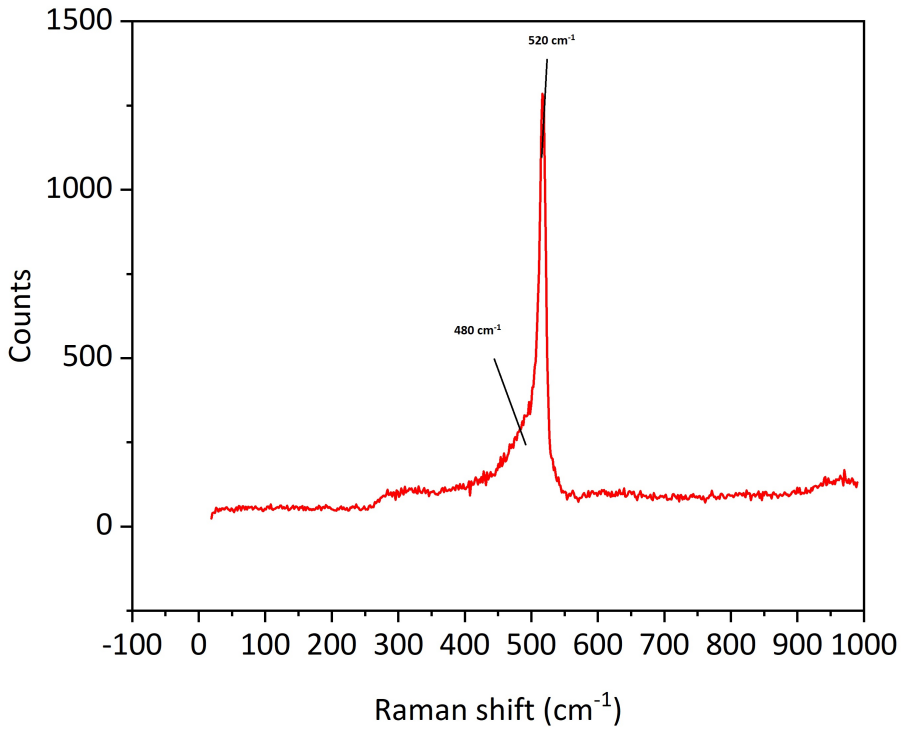

Figure 4.6: Raman spectrum between 0-900 cm^{-1} for a thin film nc-Si single-junction cell deposited on an Al substrate. The amorphous and crystalline properties can be identified at 480 and 520 cm^{-1}

2 different lasers would help probe deeper into the cells. A red laser can help determine the depositions at the start of the i-layer. The unavailability of the red laser is a disadvantage but similar measurements can also be made using a green laser. This microscope has a 25W argon laser functioning at 514 cm^{-1} with a wavenumber of 19450 cm^{-1} for the green laser. The spectral measurements can be made in the standard range wavelengths of 0-1000 cm^{-1} for determining the crystallinity of silicon [34]. And it can also be operated in the extended range from 1800-2300 cm^{-1} for analyzing the stretching modes of hydrogen [35]. The laser intensity can be varied from 0.001% to 100% but they are kept at an intensity of 5% while making the measurements. Exposure to high laser powers for a long period can crystallize the material, hence it is performed at an optimum intensity of 5%. The exposure time for standard measurements is 100s. If the measurements contain noise the time is increased to 150s to reduce the signal to noise ratio. The exposure time for measurements in the extended range is 300s, the exposure time is increased to 500s if required to reduce the signal to noise ratio. The samples were cut post-deposition to be able to make raman measurements. Since the samples were deposited on flexible aluminium substrates it was an arduous task to make the samples flat without damaging them in the process. This is done since flat samples are suitable for making precise raman measurements.

As mentioned above the raman spectroscopy setup can be used to determine the crystalline and amorphous fractions of silicon. The transverse optics modes of amorphous and crystalline silicon can be found at 480 cm^{-1} and 520^{-1} respectively as shown in the figure 4.6 [34]. The importance of the crystalline fraction of material was discussed in section 3.1. This can be calculated using raman spectroscopy. There have been several different pieces of literature on how to calculate the same. The peak-fitting approach model was incorporated to find the crystalline fraction [36]. In this method, the amorphous contribution to the nanocrystalline silicon is fitted to three different Gaussian peaks in the range from 220-480 cm^{-1}. The three peaks are namely transverse acoustic (TA), longitudinal acoustic (LA) and transverse optical (TO). The TA peak of 220cm^{-1}, LA peak of 330^{-1} and TO peak of 480^{-1} as shown in figure 4.7 [14]. This is done to ensure the amorphous contribution is taken into account without the crystalline contribution. Similarly, the crystalline contribution peaks are found at 510 and

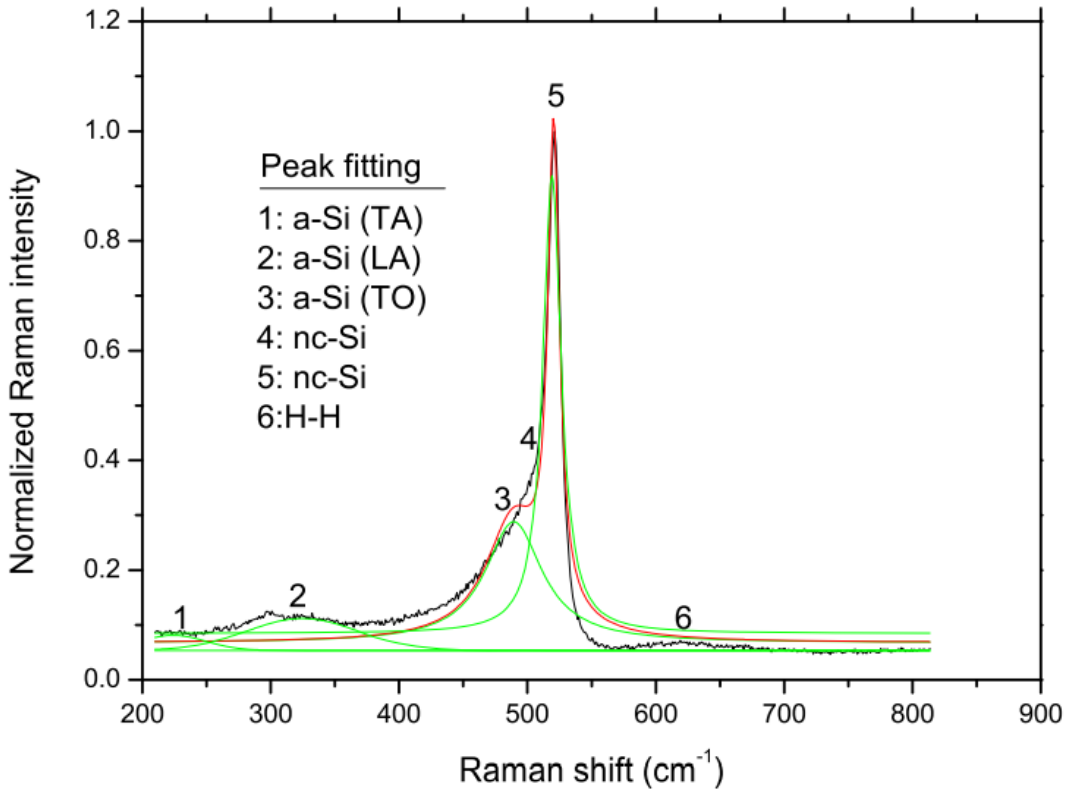

Figure 4.7: Raman spectrum used to fit peaks to identify the crystalline fraction [14]

520 cm^{-1}. They are TO peaks and they are fitted with two Lorentzian contributions [14]. After fitting the Gaussian and Lorentzian peaks the crystalline fraction is calculated using the following formula:

$$f(\%) = 100x\frac{I_{520} + I_{510}}{I_{520} + I_{510} + I_{480}} \tag{4.1}$$

Where I_{520}, I_{510} and I_{480} are the gaussian integrated at the wavenumbers 520,510 and 480 cm^{-1}. A Matlab script is used in this thesis to calculate the crystalline fraction by the above-described method. The disadvantage to this method is that it gives the crystalline fraction with respect to the amorphous part of the material.

The stretching modes of hydrides and the analysis of the bulk silicon hydrogen bonds are analyzed with measurements made in the extended range. This range is between wavenumbers 1800-2300 cm^{-1}. The information about the material can be analyzed with a set of peaks at several wavenumbers just like the measurements made in the standard range. If a twin peak is observed at 2100 cm^{-1} they are representative of porous material. The small peaks at wavenumber 2250cm^{-1} are representative of O-Si-H_x bonds as shown in the figure [35]. Since good quality solar cells with well passivated non-porous grain boundaries as discussed in the section 3.1 would have a single peak which would be characteristic of these cells as shown in figure 4.8.

The Raman setup at Kavli and ESP lab was down with a long-time repair. So, a modular raman setup that measures the intensity of the scattered light once for every 4 wavenumbers was used as an alternative for some measurements.

4.5. Fourier transform infrared spectroscopy

The most extensively used infrared spectroscopy approach is Fourier Transform Infrared Spectroscopy (FTIR). It can be used as an alternative for measuring the hydride stretching modes that can be deter-

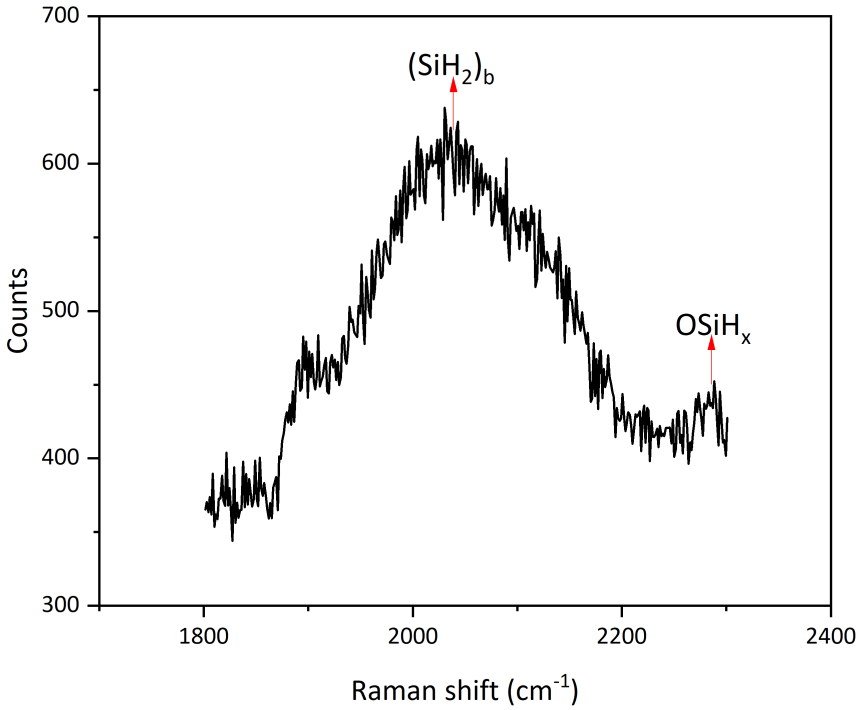

Figure 4.8: Labelled graph of the stretching modes of hydrides in silicon found in the extended range rama measurements

mined by raman spectroscopy. The various nc-SiO_x:H bonds can also be distinguished using this technique. Infrared absorption spectra reveal vibration modes of non-symmetric bonding arrangements. The working principle of this technique involves a Michelson interferometer and beam splitter as shown in figure 4.9. The source beam is split using a beam splitter onto a stationary mirror and a moving mirror. The beam reflected from these mirrors passes through the sample onto a detector. The superimposed beams at the detector are used to find the absorption spectrum. The absorption spectrum is calculated by the Fourier transform interference of the reflected beam. The number of measurements is increased to reduce the noise in the spectrum obtained [32].

In this case, a coherent light source is directed onto a sample after passing through the beam splitter and the mirrors. The light is first passed through a reference sample with just the laminated sheet and the TCO on top of it. Then the light is passed through the laminated sample. This is used to filter out the other transmittance spectrum obtained from other parts of the cell such as the lamination sheet and the glue used to laminate the sample. The measured transmittance at the detector as shown in figure 4.9 is converted to a spectrum using Fourier transform. This spectrum obtained generates an absorption versus wavelength graph. Various absorption peaks can be noticed in this graph. These absorption peaks at certain wavenumbers as shown in figure 4.10 correspond to different chemical bonds present in the sample. Thermo Electron Corp model Nicolet 5700 is used to make the FTIR measurements. Various vibrational modes of the sample and the quality of the bonds can be measured using the same.

4.6. Scanning electron microscopy

Scanning electron microscopy (SEM) is a microscopic technique used to analyze the deposited cell structure. The SEM uses a stream of electrons as the source. These electrons move towards the surface and bounce off the surface to produce secondary electrons. These secondary electrons are

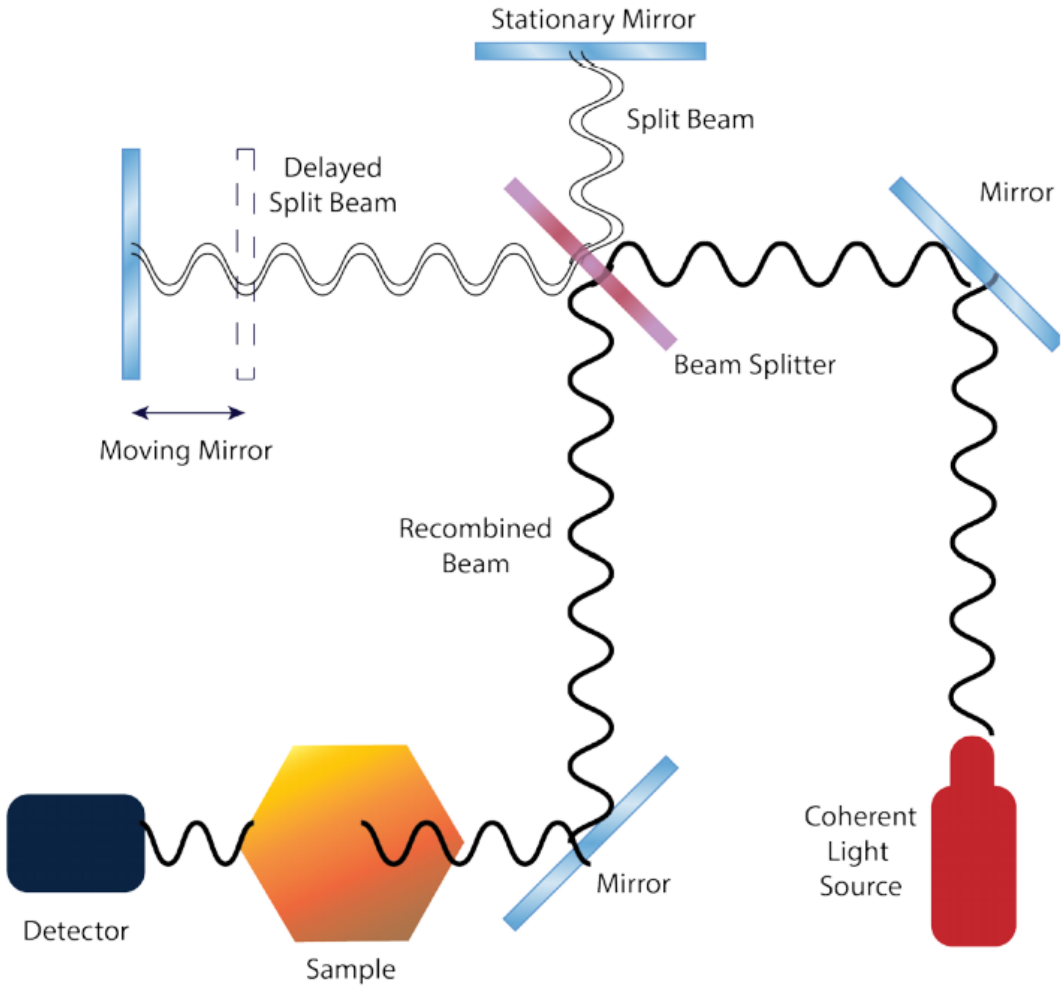

Figure 4.9: Schematic diagram of an FTIR setup and its components [32]

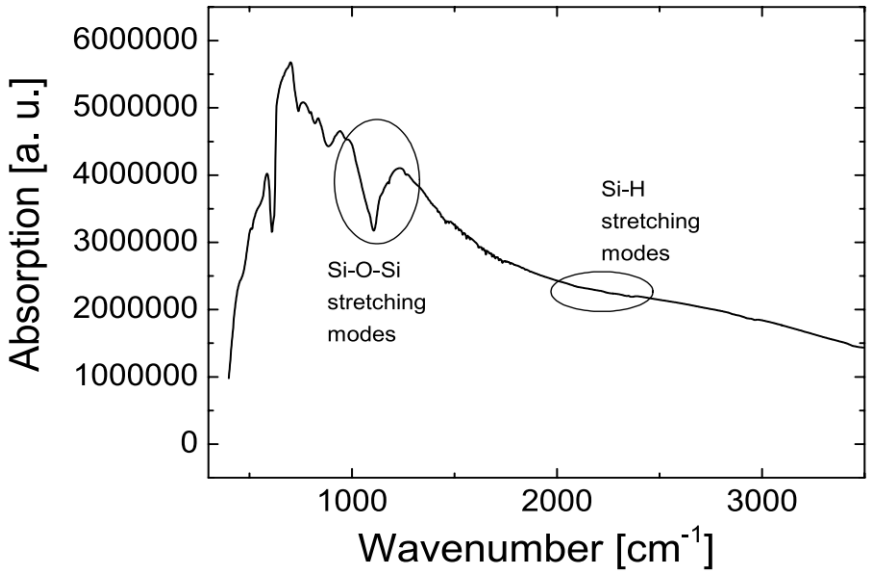

Figure 4.10: FTIR absroption spectrum for an nc-Si cell [32]

captured and used for imaging. The secondary electrons contain backscattered electrons, diffracted

backscattered electrons, photons, visible light and heat [37]. These measurements are made under a vacuum.

SEM imaging is an easy and non-destructive imaging technique. It is used to make clear images of the cross-sections of the cells. The user is able to magnify images up to the nanometer range. The deposition rates are also measured from SEM imaging. Apart from cross-sectional imaging, the surface of the cells can be pictured. The chemicals on the surface can be identified but the surface morphology cannot be analyzed using the SEM [38]. Only cross-sectional SEM imaging is done for this project. This is an arduous process as the cells deposited on the flexible aluminium substrates had to be cut according to the desired dimensions to fit inside an SEM machine.

4.7. Current-voltage characterization

The electrical performance of the cell is determined by analyzing the current-voltage characteristics of the cell under illumination. This illumination is performed using a solar simulator calibrated at the AM1.5 solar spectrum. The current-voltage characteristics of the cells measured in the dark is used to determine if the deposited cells work or if they are shunted. If the current-voltage curve obtained mimic a diode (if slope at V=0V is high) then it represents a working cell. If it mimics resistive (if slope at V=0V is low) behaviour then the cell is damaged [8].

From the I-V curve obtained from illuminated measurements the open-circuit voltage V_{oc}, short circuit current I_{sc}, maximum power point voltage V_{mpp}, maximum power point current I_{mpp} are obtained. As seen in the figure 4.11 V_{oc} is the voltage of the cell in open circuit condition when the current that flows through the external circuit is 0. Similarly, the I_{sc} is the current at short circuit condition when the applied voltage is 0. The V_{mpp} and J_{mpp} are the voltage and current density at the maximum power point respectively. The fill factor (FF) of the cell is then calculated using the equation 4.2 below.

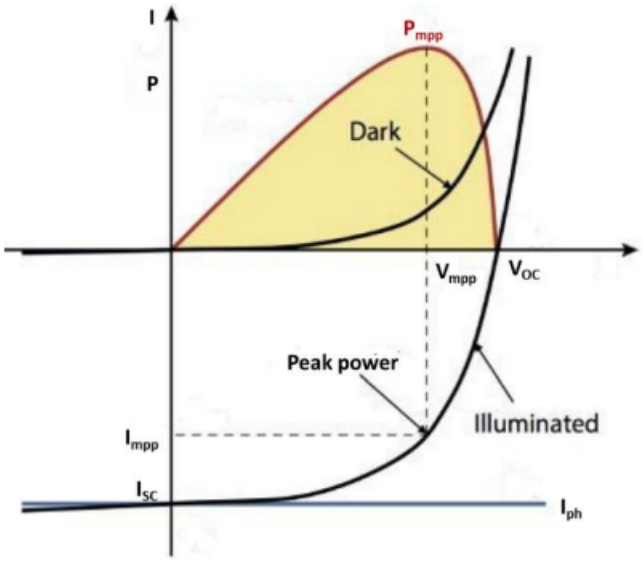

Figure 4.11: Dark and illuminated IV characteristics measured using a solar simulator [8]

$$FF = \frac{V_{\text{mpp}} \times I_{\text{mpp}}}{V_{\text{oc}} \times I_{\text{sc}}} \tag{4.2}$$

The efficiency of the solar cell is defined as the ratio of the electrical output of the cell to the solar energy incident on the cell. It is calculated as shown in equation 4.3 below.

$$\eta = \frac{V_{\text{mpp}} \times I_{\text{mpp}}}{P_{\text{in}}} = \frac{V_{\text{oc}} \times I_{\text{sc}} \times FF}{1000 W/m^2} \tag{4.3}$$

4.8. External Quantum Efficiency

EQE is defined as the ratio of the number of charge carriers collected at the solar cell terminal to the number of photons incident on the solar cell [39]. It is an important tool to determine the performance of a solar cell. EQE indicates how the solar cell behaves to incident monochromatic light and this also determines how a solar cell converts the light with different wavelengths into electricity. A chopper, monochromator and lock-in amplifier are the main components of an EQE setup. A suitable chopped monochromatic light for EQE measurements is generated using a monochromator and the chopper. This light is incident on the solar cell and the photogenerated current is measured and subsequently, the EQE is calculated. A typical EQE curve at different wavelengths for a solar cell is shown in the figure 4.12.

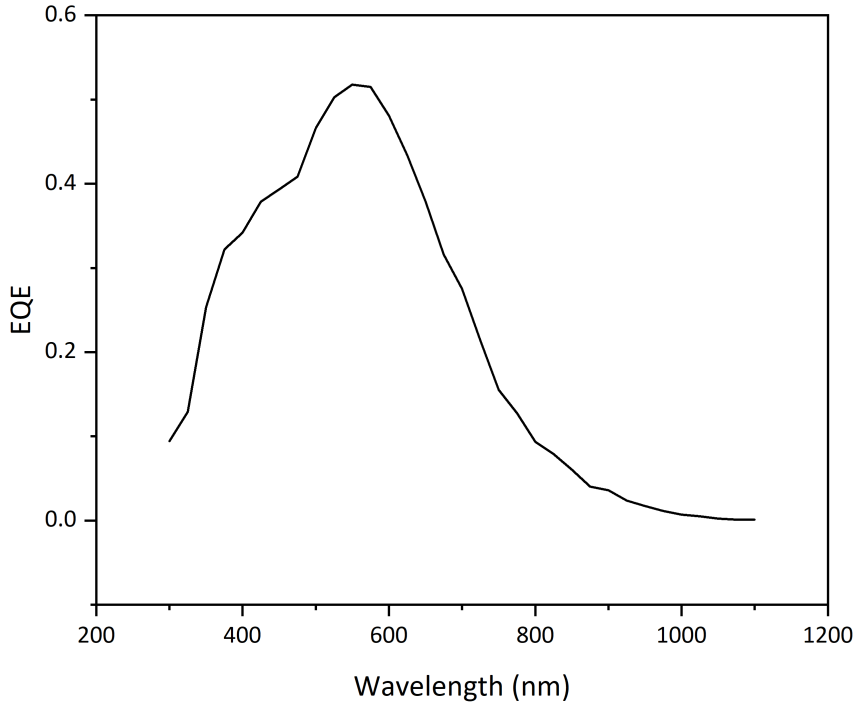

Figure 4.12: Standard EQE v/s wavelength plot

4.9. Reflectance

A PerkinElmer®Lambda 1050 setup is used to make reflectance measurements. Transmittance can also be calculated using the same device but since the solar cells are not transparent, only the reflectance measurements are made.

The samples are placed in the sample holder. The wavelength range is chosen for the incident monochromatic light from 300-1100nm wavelengths. The reflectance values are calculated at every 5nm wavelengths in the 300-1100nm range. The incident light is passed through a double monochromator which filters out the unwanted light and this light is made to fall on the solar cell. The cell reflects this light onto an integrating sphere coated with highly diffusive reflective material, which deflects the

light until they reach the detectors inside the sphere. The detected reflected light is used by the software to plot a reflectance vs wavelength function. Since the cells are not transparent, the transmittance is considered to be zero. Hence, the absorption can be calculated from the reflectance measurements made. The absorptance is obtained by subtracting the reflectance from 1 [40]. The internal quantum efficiency (IQE) which is defined as the ratio of the number of electron-hole pairs generated to the number of incident photons on the active layers can also be calculated. The IQE can also be calculated by the ratio of the EQE by the absorptance.

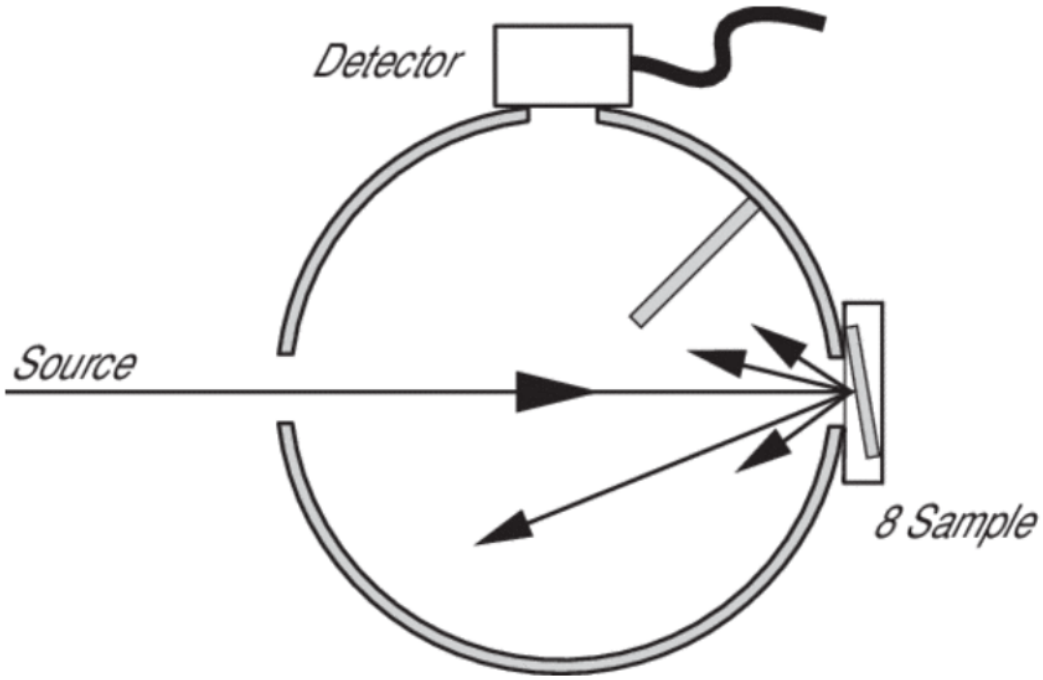

Figure 4.13: Schematic diagram of the reflectance measurements made using a spectrophotometer [41]

5

Results and discussion

In this chapter all the experiments performed and the corresponding results obtained are discussed. This chapter is split into the characterization of unprocessed cells performed at TU Delft and the characterization of the processed cells performed at TU Delft and HyET solar.

5.1. Power series

Initially, a power series was performed by varying the deposition RF power for the i-layer. It was performed to identify the optimal deposition rates for device grade crystalline thin-film intrinsic layers.

5.1.1. Initial deposition

A set of samples are deposited with deposition powers in the range of 25-80 W. The deposition RF power of the first sample was 25W after which the deposition power was increased by a factor of 10 from 30W until 80W. The cells are deposited in a p-i-n superstrate configuration. First, an AZO (front TCO) layer is deposited on top of the textured Al substrate. Then the sample is treated with Argon plasma to smoothen the roughness of the pyramids. Then the doped p-layer is deposited. Then a seed layer is deposited with ten fifty-second steps to ensure a good p-i interface is maintained. Then the remaining intrinsic layer and n-doped layer is deposited. The deposition parameters that were used for depositing the doped and active layers are as mentioned below in table 5.1. The silane and hydrogen flow rate during the i-layer deposition are kept constant at 3.3 sccm and 120 sccm respectively.

Layer	Deposition time (s)	Temperature (°C)	Pressure (mbar)	Power (W)
p-layer	1800	300	2.2	12
n-layer	720	300	1.5	11
i-layer	3810	300	4	25-80

Table 5.1: Power series deposition parameters

After the deposition, the cells are characterized which is discussed below.

Optimizing deposition rate

The deposited cells need to be characterized to analyze their properties. The change in deposition rate due to the change in deposition power can be determined by cross-sectional SEM imaging. The image

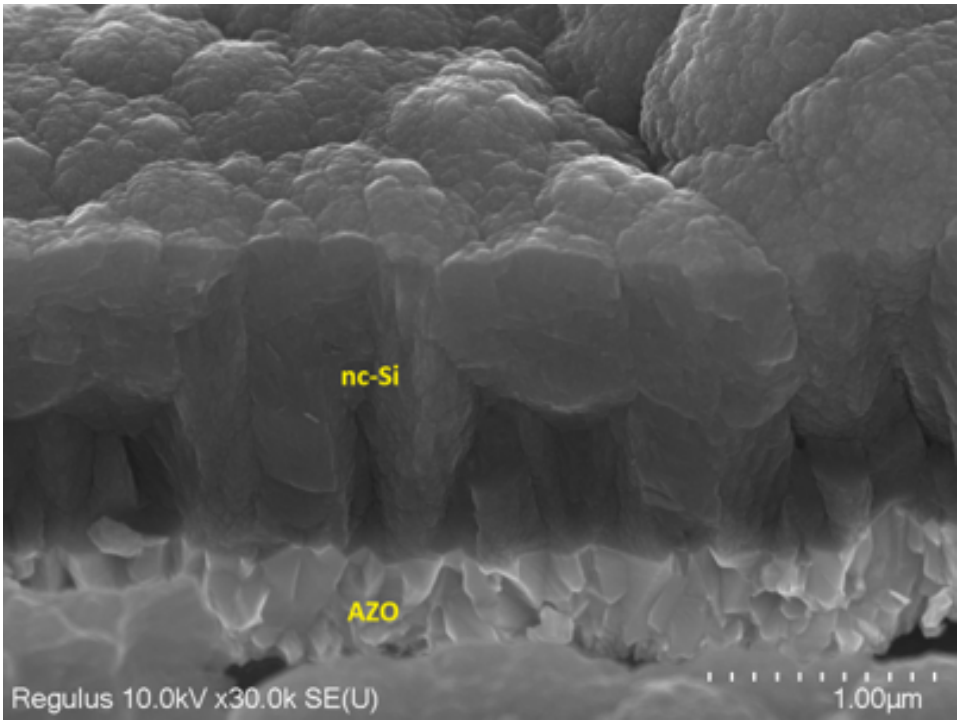

Figure 5.1: Labelled SEM image of an unprocessed cell deposited on an Al substrate

from the SEM is labelled as follows as shown in the figure 5.1. The bright white region is the TCO while the dark black region above the TCO is silicon. The cells are cut into small pieces to fit them inside the sample holder of the SEM device. The cross-section of the sample analyzed under the SEM is as shown in figure 5.2. The height of the silicon layers are measured from the SEM images for calculating the deposition rates. The length of the silicon layer is divided by the deposition time (3810 s) gives the deposition rate. The deposition rate is then compared for the different powers of deposition as shown below in the figure 5.3.

In figure 5.3, it can be seen that the deposition rate increases exponentially with the increase in power. At 25W (0.17W/cm^2) the deposition rate is very low at 0.23 nm/s while at 80W (0.55W/cm^2) the deposition rate is more than twice as large as the deposition rate at 25W. We can also see that the deposition rate increases a lot from 25W-40W (0.17-0.278W/cm^2) while the deposition rate after 40W until 70W (0.48W/cm^2) is almost quite stable and does not increase as much as it increases from 25-40W. It can also be noted that from figure 5.2 that at lower powers of deposition (25W and 30W) the surface of deposition looks far smoother than the depositions made at higher powers of deposition from 40-80W. There is a clear difference and this difference in surface texture is discussed below.

Material characterization

The cells after the SEM imaging are focussed under the raman microscope for characterization. The cells can be distinguished as amorphous or crystalline from the raman intensities observed from wavenumbers 0-1000 cm^{-1}. The raman intensities obtained for the respective raman shift in the aforementioned range is normalized to its maximum and plotted against the raman shift as shown in the figure 5.4. Measurements made using a different raman setup for the same cells and the results are discussed in appendix A.1.

It can be clearly seen from the figure that at a lower power of deposition (25 and 30W) the cells have a peak at 480 cm^{-1}. The cells also have a very flat line when normalized to its maximum which is characteristic of an amorphous material. At a higher power of deposition (40-80W) there is only a single peak around 510-520 cm^{-1} which is characteristic of crystalline material. The crystalline fraction of the material is also calculated as explained in section 4.4. The crystalline fraction change with the increase in power is shown in figure 5.5. We can see that the crystalline fraction increases as the power increases. While the crystallinity increases drastically from 25-40W. Beyond 40W the increase is fairly

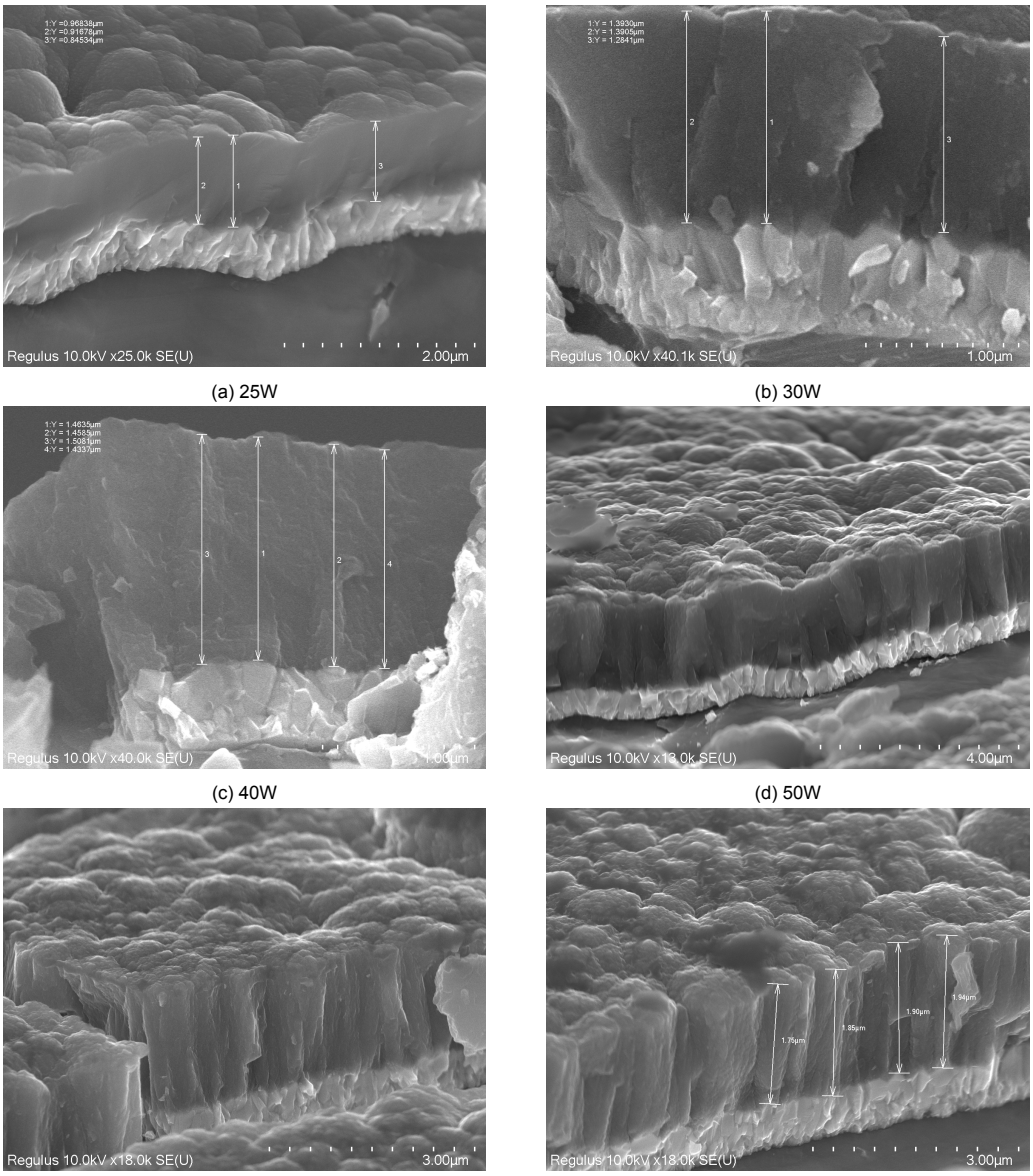

(a) 25W (b) 30W

(c) 40W (d) 50W

(e) 70W (f) 80W

Figure 5.2: SEM images of the initially deposited power series cells

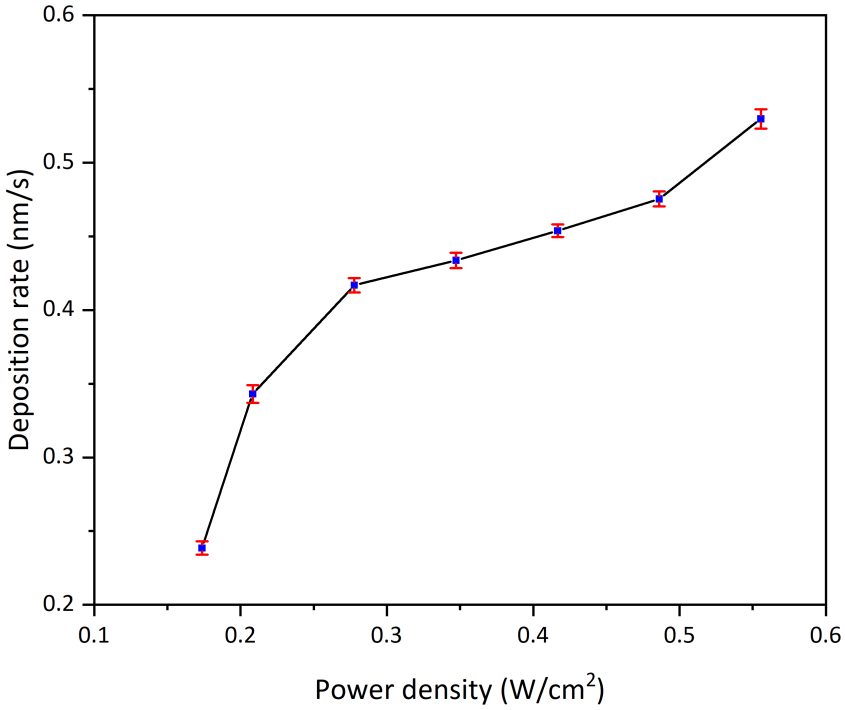

Figure 5.3: Deposition rate v/s power density with error bars for the initial power series deposition

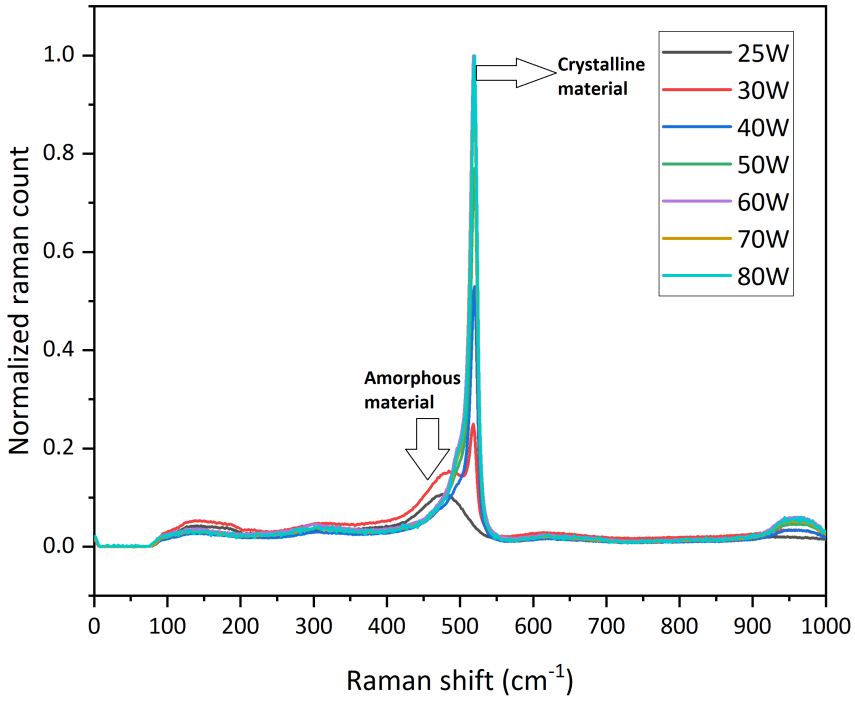

Figure 5.4: Normalized raman counts v/s Raman shift for the initial power series deposition measured using a green laser

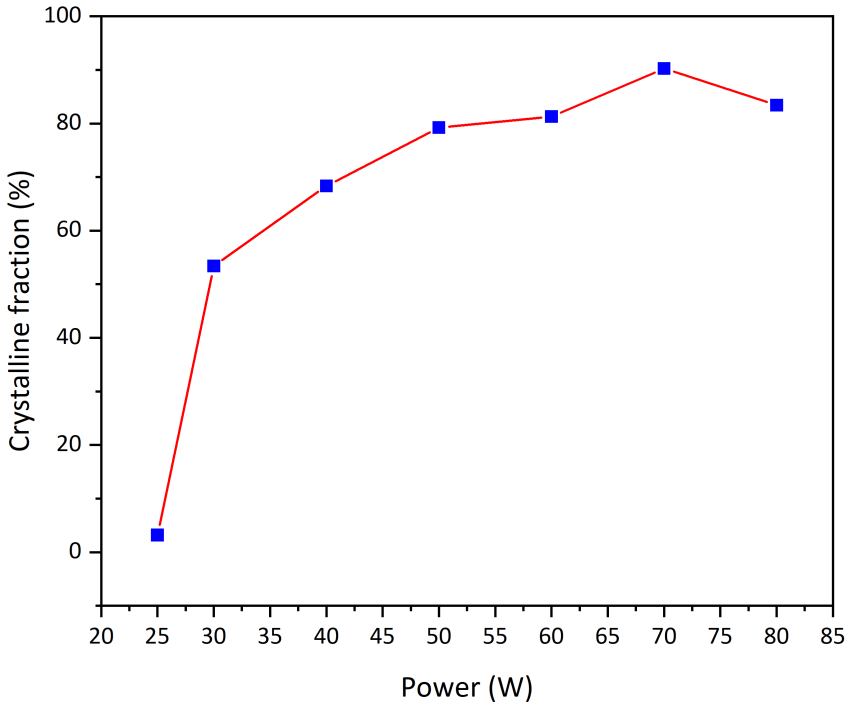

Figure 5.5: Crystalline fraction v/s Power for the initial power series deposition

constant. It is to be noted that at 40W the material shifts from amorphous to crystalline and also has a crystalline fraction of around 60% which is ideal for device grade materials.

It can also be seen in figure 5.2 at lower powers of deposition the cells have a smoother silicon surface. This might also be another indicator of amorphous material, while at higher powers of deposition the surface is not smooth, but instead the cell surface is rough and contains sharp peaks. This is a characteristic of crystalline silicon material. The results obtained from the SEM imaging are identical to the observation from raman spectroscopy.

The raman measurements were also made in the extended range from wavenumbers 1800-2400 cm^{-1} to analyze the hydrogen stretching modes. It can be seen from the figure 5.6 that all the cells deposited only have a single peak in the 2000-2200 cm^{-1} wavenumber range. This indicates that the cells are non-porous and also shows the presence of $(Si\text{-}H_2)_b$ bonds. The small peak around 2300 cm^{-1} corresponds to the $OSiH_x$ bonds. It can also be observed that the peak for amorphous materials (25, 30W) is around 2050 cm^{-1}, while the peak shifts to 2150 cm^{-1} for the crystalline material (50-80W). This trend is similar to the results obtained from the standard range raman measurement. It is also to be noted that even at higher deposition powers the cells have a strong silicon-hydrogen bond and do not crystallize completely. The intensity of the raman counts for the 30W sample is higher than the rest of the samples because the sample was measured over an increased exposure time. Increasing the exposure time reduces the signal to noise ratio.

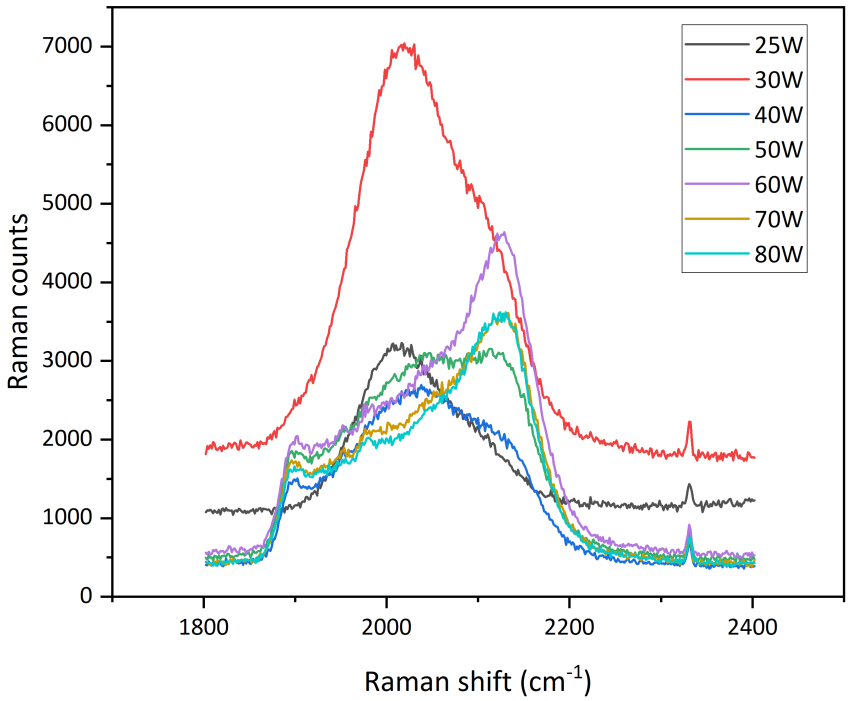

Figure 5.6: Raman counts v/s raman shift measurement for the initial power series deposition in the extended range for the stretching modes of hydrogen measured using a green laser

5.1.2. Second deposition

The initial deposition series was over a wide range of RF powers ranging from 25-80W. The cells were characterized and it was noticed that there is a transition from amorphous to crystalline material in the intrinsic layer while increasing the RF power from 30W to 40W. To find the exact RF power at which the deposited cells transition into crystalline material, another set of experiments was performed by changing the RF power from 35-45W and keeping the other parameters for the doped layers constant as mentioned in table 5.1. The parameters for the absorber layer are as mentioned in table 5.2. The hydrogen flow rate was also constant as mentioned in the first deposition at 120 sccm. After the deposition, the material characterization was performed.

Layer	Deposition time (s)	Temperature (°C)	Pressure (mbar)	Power (W)	Silane flow (sccm)
i-layer	3810	300	4	35-45	3.3

Table 5.2: Power series second deposition parameters

Optimizing deposition rate

The deposition rates of the power series performed from an RF power of 35-45W are obtained from SEM imaging. The SEM images are shown in figure 5.7. The deposition rate is calculated from these images are plotted against the RF power density of deposition as shown in figure 5.8. There is a constant increase in the deposition rate with an increase in power density as expected. But the change in deposition rate is negligible.

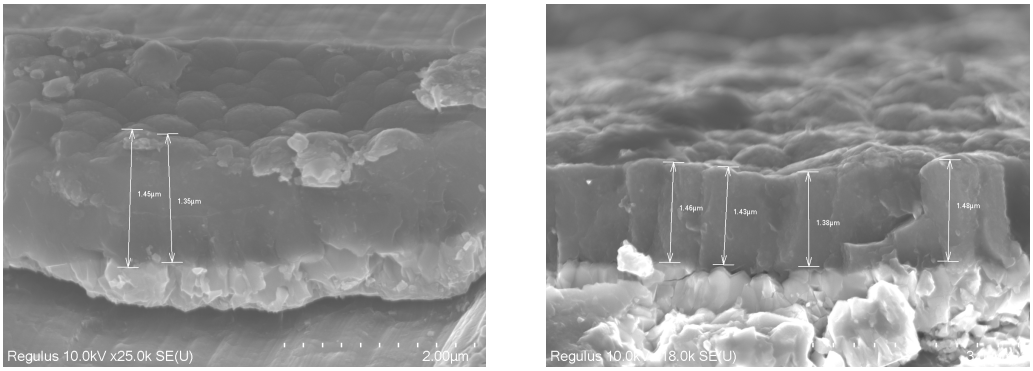

(a) 35W

(b) 38W

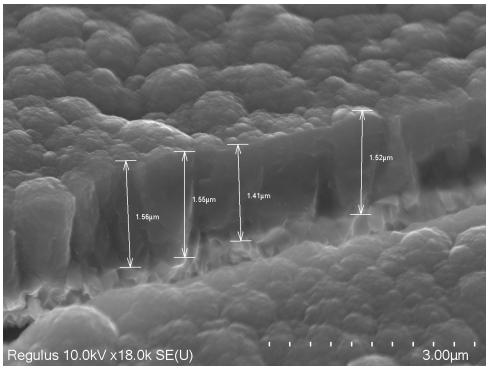

(c) 42W

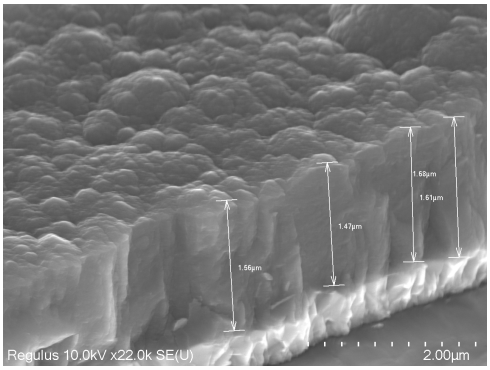

(d) 45W

Figure 5.7: SEM images of the second power series cells

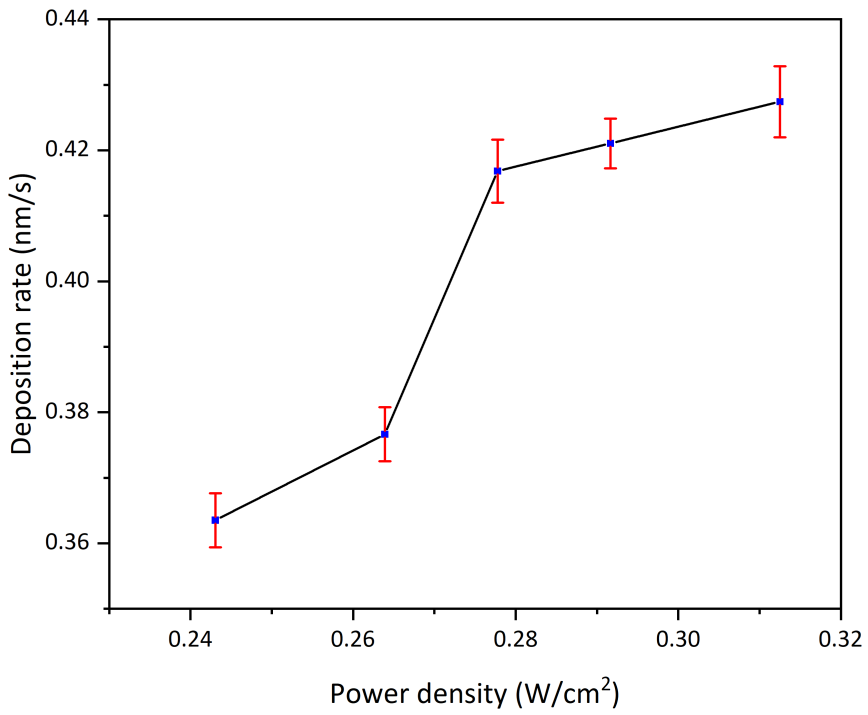

Figure 5.8: Deposition rate v/s power density for the second power series deposition

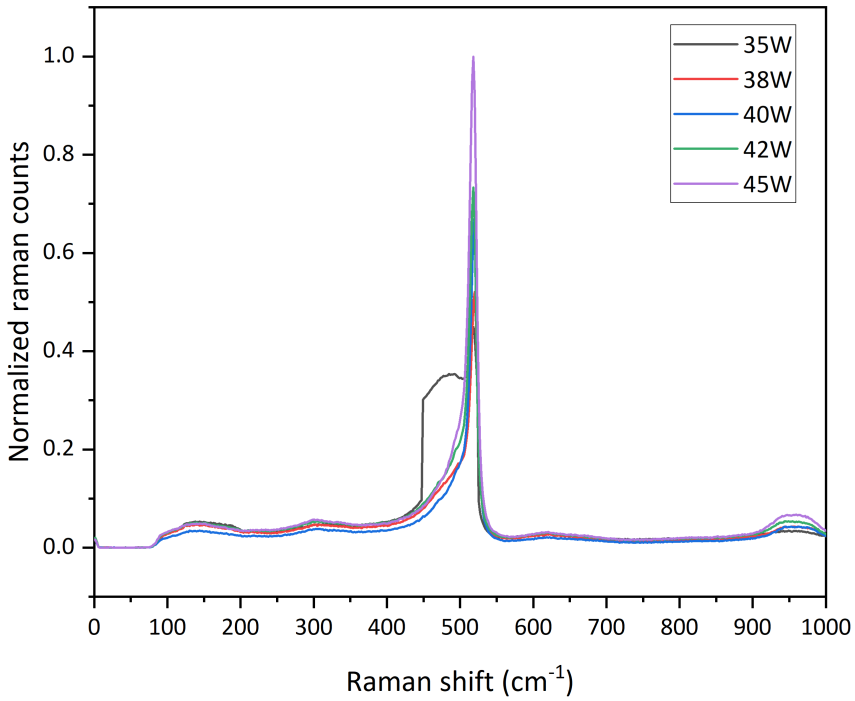

Figure 5.9: Normalized raman counts v/s raman shift for the second power series deposition measured using a green laser

Material characterization

The deposited cells are characterized under the raman microscope again. The 35W cell has a peak at 480 cm^{-1} as shown in figure 5.9. This is characteristic of an amorphous material while the cells above 35W do not have a peak at 480 cm^{-1} which are representative of crystalline material. The crystalline fraction of the 35W cell is lower than 50% which shows that it is amorphous. While the crystalline fraction of cells above 35W have a crystalline fraction above 50%. The 38W cell has a crystalline fraction slightly lower than an ideal crystalline fraction of 60%. But the crystalline fraction of 40,42 and 45W samples are fairly constant around 70%.

The extended range raman measurements were performed under the green laser to analyze the stretching modes of hydrogen. It can be clearly seen from the figure 5.11 that the 45W cell has a peak around 2150 cm^{-1}. As discussed in the extended range graph (figure 5.6) for the initial deposition, the 35-42W cells have a peak at 2050 cm^{-1} which were found in the amorphous cells. But the 45W cell has its peak at 2150 cm^{-1} which were found in the crystalline cells. These results are contradictory to the raman measurements made in the standard range where all the cells except the 35W cell displayed crystalline behaviour.

5.2. Thickness series

After analyzing the change in cell properties with the change in RF power of deposition, a thickness series was performed to analyze the change in the properties of a cell with the change in thickness of the i-layer. The thickness series was performed at an RF power of 25,50 and 80W. The thickness of the i-layer analyzed in this series is 0.5 µm, 0.9 µm, 1.5 µm, 1.65 µm and 2 µm. Analyzing the change in the crystalline fraction of the cell with the increase in thickness of deposition is one of the

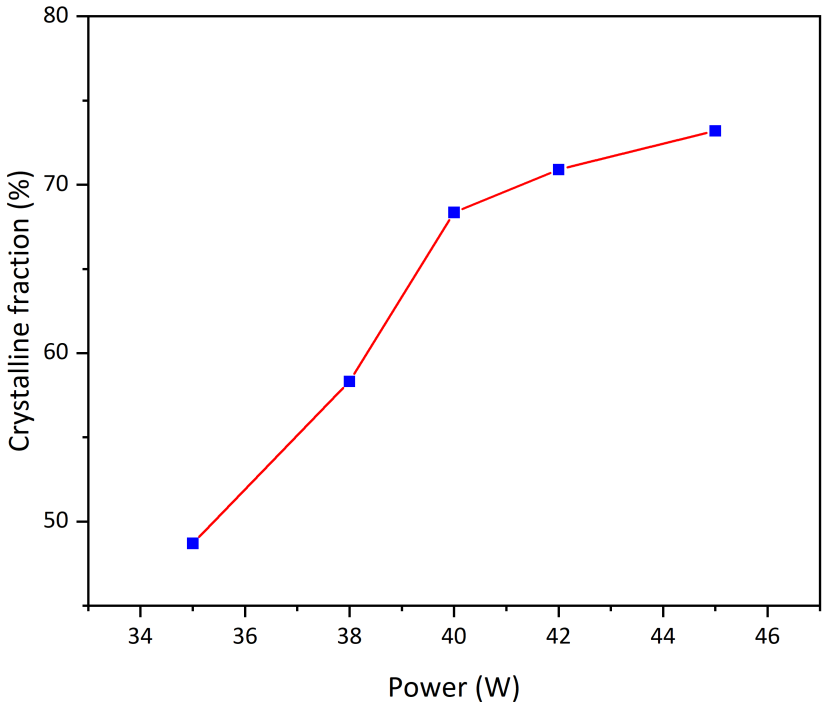

Figure 5.10: Crystalline fraction v/s power for the second power series deposition

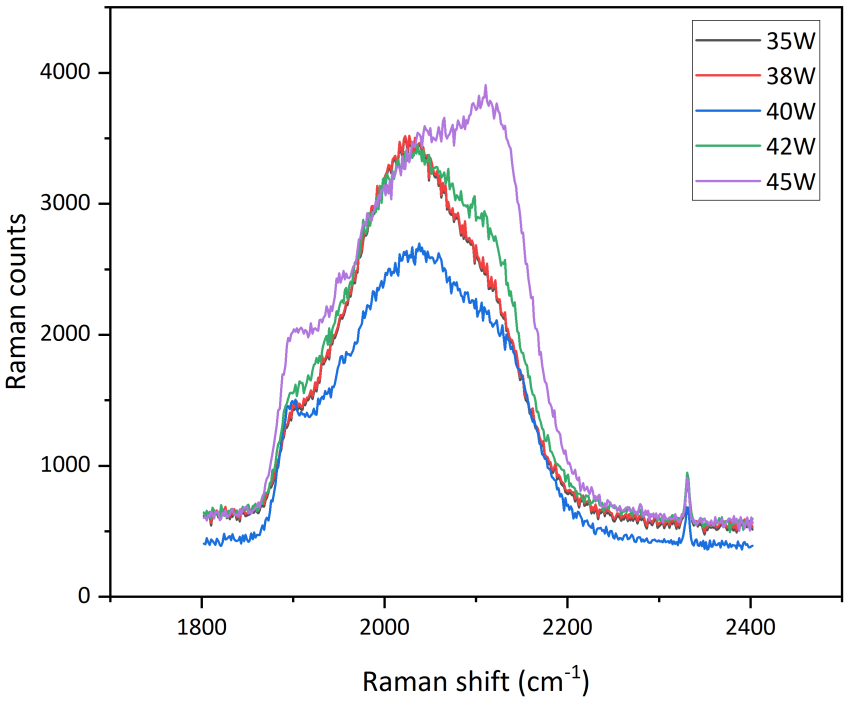

Figure 5.11: Extended range raman counts vs raman shift to analyze the stretching modes of hydrogen measured using a green laser

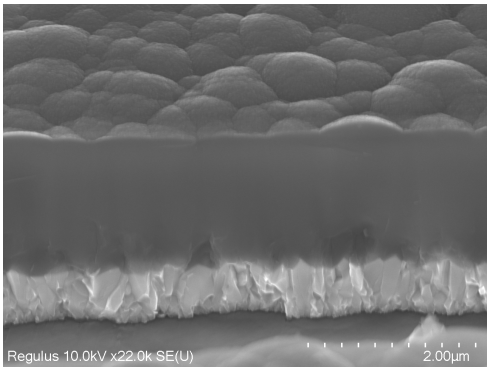

(a) 1.65 µm

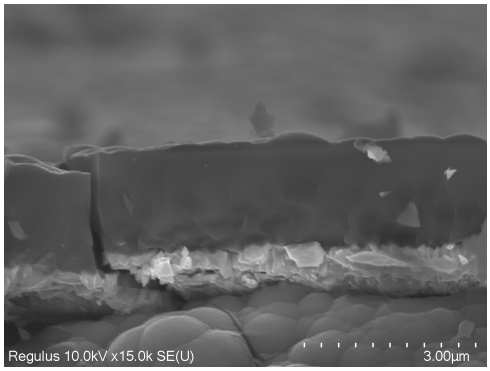

(b) 2 µm

Figure 5.12: SEM images of 25W thickness series cells

main objectives of this series. From the results obtained in section 5.1.1, the cell with RF power of 25W displayed amorphous properties, while the cell with 80W displayed crystalline properties and the 50W cell was in the transition phase. Hence, the change in cell properties for different materials can also be analyzed using this thickness series.

5.2.1. Deposition parameters

The deposition parameters are almost the same for the thickness series and only the deposition time was adjusted according to the thickness of the intrinsic layer. The deposition time was changed according to the deposition rates obtained from the section 5.1.1 for the respective deposition power. It was assumed that the deposition rates would remain the same with an increase in deposition time. The silane flow rate and hydrogen flow rate for the intrinsic layer were 3.3 sccm and 120 sccm respectively. The other deposition parameters are mentioned below in table 5.3.

Layer	Deposition time (s)	Temperature (°C)	Pressure (mbar)	Power (W)
p-layer	1800	300	2.2	12
n-layer	720	300	1.5	11
i-layer	1450-7290	300	4	25,50,80

Table 5.3: Thickness series deposition parameters

5.2.2. 25W thickness series

The deposition parameters are as described above and cells with a thickness of 0.9 µm, 1.5 µm and 1.65 µm and 2 µm were deposited for the same RF power of 25W. The cell deposited for 3810s at RF power of 25W in the i-layer in the power series had a thickness around 0.9 µm. It was assumed that cells deposited lower than this thickness would be amorphous and 0.5 µm thickness deposition was not performed. The cells are characterized after the deposition. Some SEM images of the cells are shown in the figure 5.12. It can be clearly seen from these images that even at a thickness of 2 µm the cell surface is smooth which is representative of the amorphous material. The deposition rates are also measured to check if there is any variation in the deposition rates obtained from the power series. But the deposition rates were analogous to the deposition rates obtained for 25W RF power in the power series. Apart from SEM imaging, the cells were characterized using raman spectroscopy.

These cells were characterized using raman spectroscopy. The raman results in the standard range (0-1000 cm^{-1}) is shown in the figure 5.13. It can be seen clearly from the figure that at all thicknesses of deposition, the cells have an amorphous incubation layer which is noticed from the peak at 480 cm^{-1}.

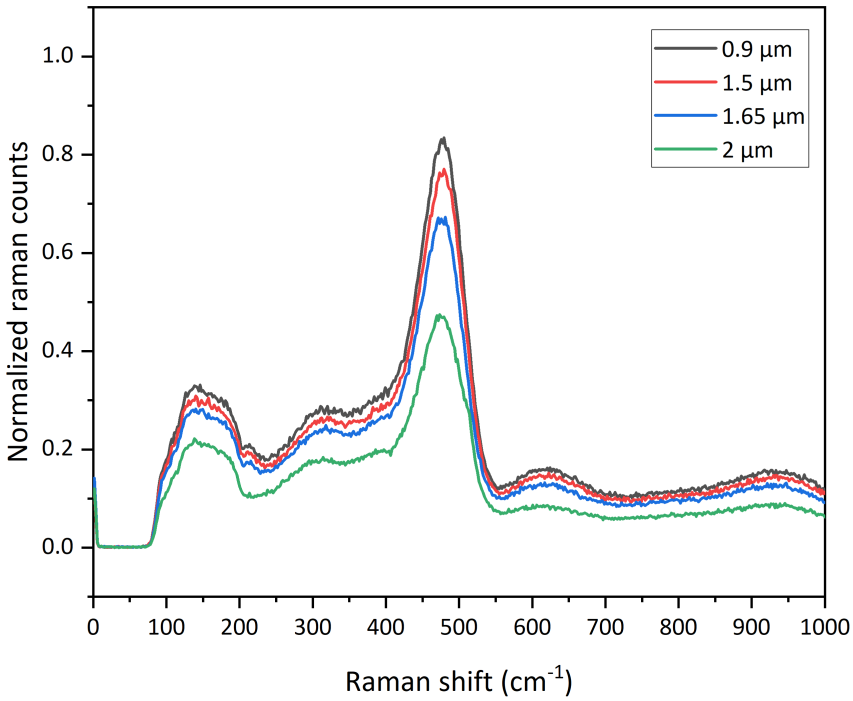

Figure 5.13: Normalized raman counts v/s raman shift for the 25W thickness series measured using a green laser

It can be concluded that the cells are completely amorphous, from the crystalline fraction obtained as shown in the figure 5.14. The crystallinity does not change with the increase in cell thickness and almost all the cells deposited have an amorphous incubation layer and the crystalline fraction suggests that the cells are amorphous in nature.

The extended range raman measurement performed under the green laser is shown in figure 5.15. All the cells have a peak at 2050 cm^{-1}. The amorphous materials in the section 5.1.1 had a peak at a wavenumber of 2050 cm^{-1}. If you compare the crystalline fraction and the standard range measurement, the extended range results cognate with the aforementioned results. So, we can conclude that the cell crystallinity does not change with the increase in thickness of deposition. From the extended range raman measurement, the presence of silicon hydrogen and silicon oxide bonds is observed in all the depositions.

5.2.3. 50W thickness series

The cells were deposited with thicknesses of 0.5 µm, 0.9 µm, 1.5 µm, 1.65 µm and 2 µm at an RF power of 50W. All other parameters are mentioned in table 5.3. The cells are characterized using SEM initially. The SEM images of the 50W thickness series cells are shown in figure 5.16. The cells deposited at a thickness of 0.5 µm do not have a smooth surface while analyzing the cross-sections using SEM. The surface of silicon observed under the SEM is not smooth which resemble crystalline material. Similar cross-sections are observed for cells with a thickness of 2 µm in the i-layer. The deposition rates were also analyzed from the SEM images and they were analogous to the deposition rates obtained for an RF power of 50W in the section 5.1.1. There was a slight difference in deposition rates but the difference was negligible. Cells are then analyzed under a raman microscope using a green laser.

For the standard range raman measurement, the cell properties did not change with the increase in thickness. It can be seen in the figure 5.17. All the cells deposited in this thickness series have a

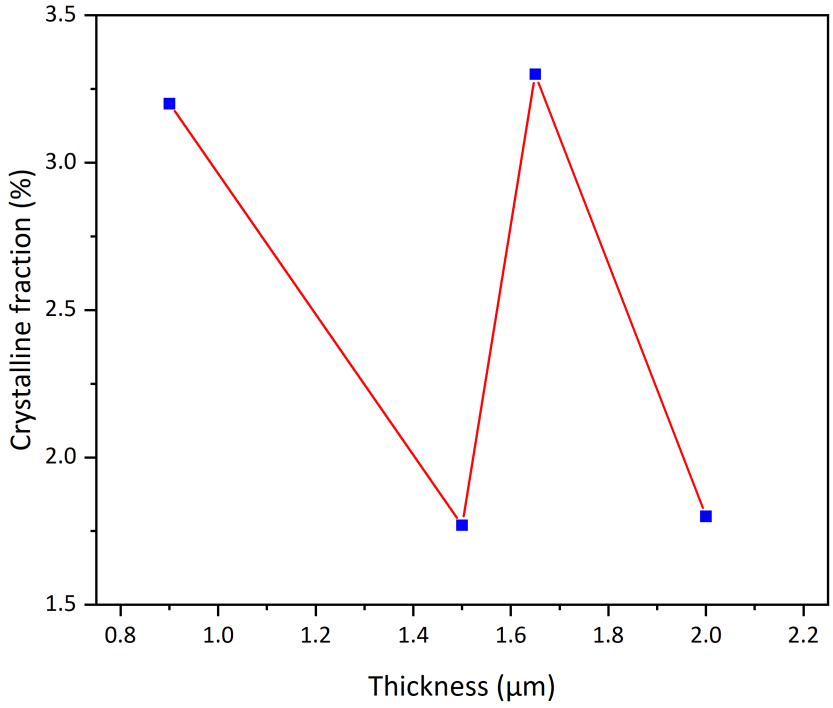

Figure 5.14: Crystalline fraction v/s thickness for the 25W thickness series measured using a green laser

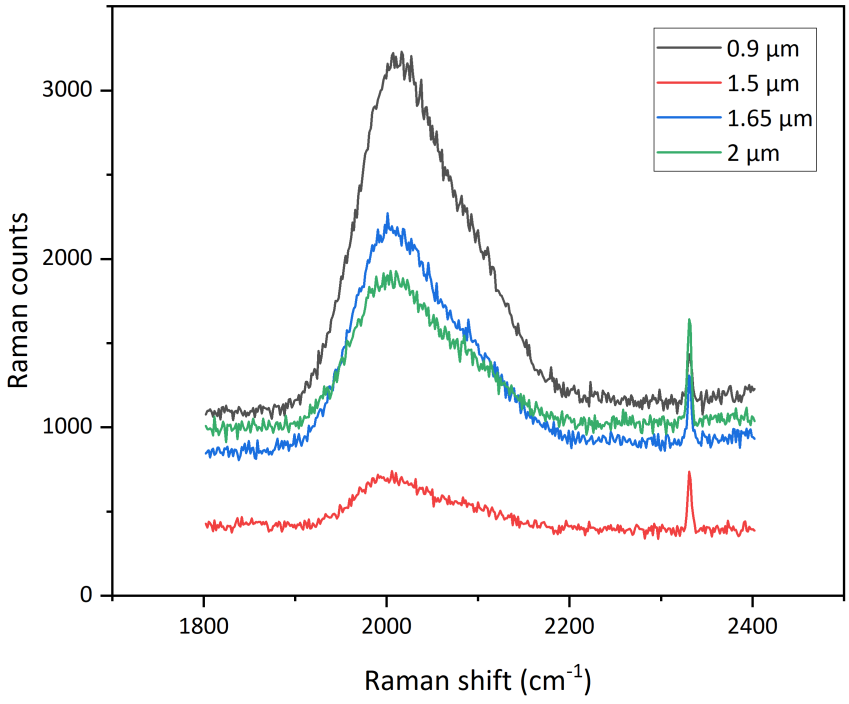

Figure 5.15: Extended range raman counts v/s raman shift for the 25W thickness series measured using a green laser

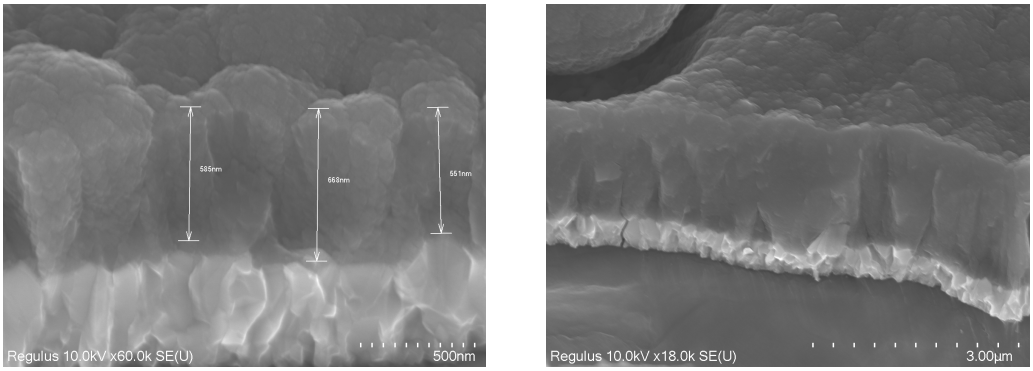

(a) 0.5 µm (b) 2 µm

Figure 5.16: SEM images of 50W thickness series cells

peak around 520 cm^{-1} which represent crystalline behaviour. Also, they do not have any amorphous incubation layer visible at a wavenumber of 480 cm^{-1}. The crystalline fraction calculated is shown in figure 5.18. The crystalline fraction increases with the increase in thickness. But the crystalline fraction decreases from a thickness of 1.65 µm to 2 µm. But the change in the crystalline fraction is negligible and all the deposited cells are within a small crystalline fraction range.

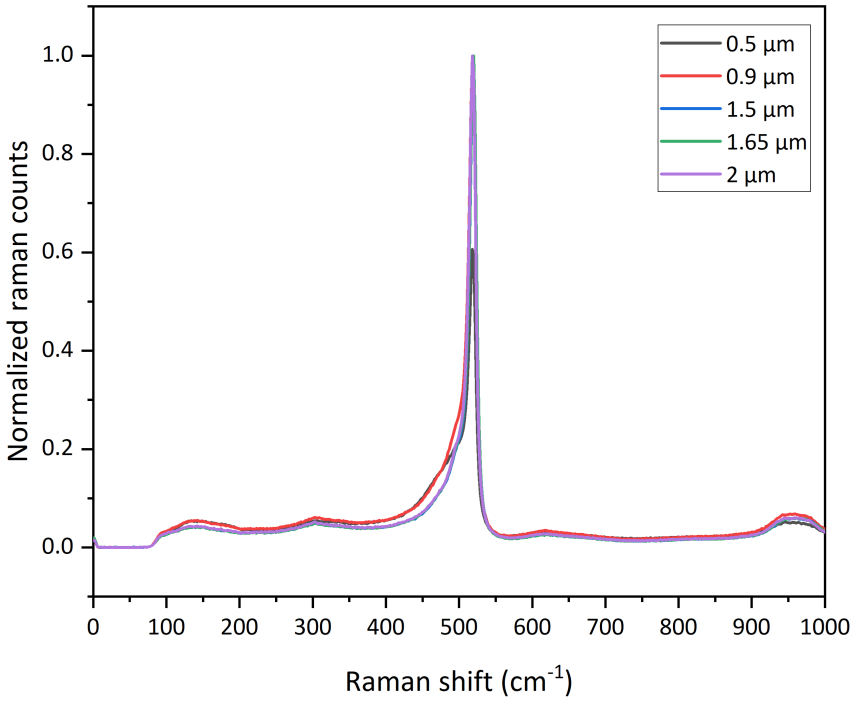

Figure 5.17: Normalized raman counts v/s raman shift for the 50W thickness series measured using a green laser

From the extended range measurements as seen in figure 5.19, even the cells deposited at a thickness of 0.5 µm have good silicon hydrogen bonds. But the cells deposited at 0.5 µm and 0.9 µm have a peak at a wavenumber of 2050 cm^{-1}. This peak was observed only for amorphous materials previously. This is contradictory to the results obtained from the standard range measurements. The cells with thickness of 1.5 µm and 1.65 µm contain multiple peaks at 2050 cm^{-1} and 2150 cm^{-1}. The presence of multiple peaks indicates that the cells are porous [35]. Other cells seem to be non-porous

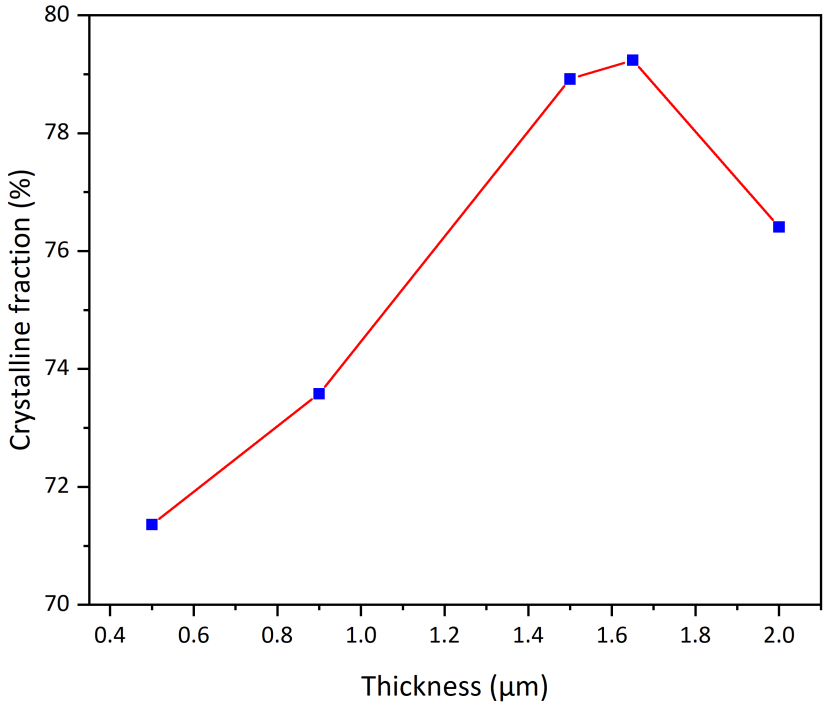

Figure 5.18: Crystalline fraction v/s thickness of i-layer for the 50W thickness series

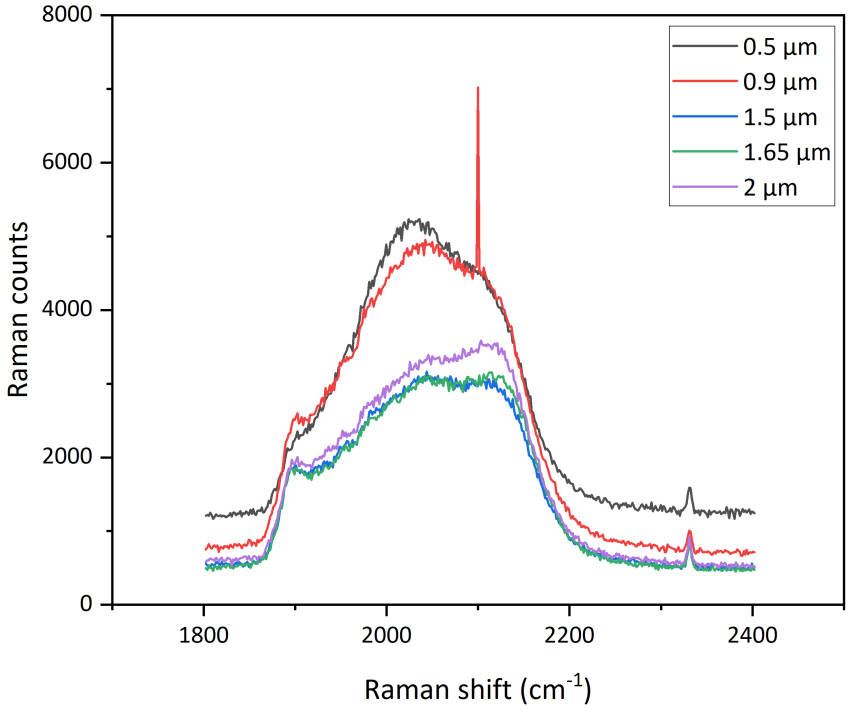

Figure 5.19: Raman counts v/s raman shift for 50W thickness series measured using a green laser

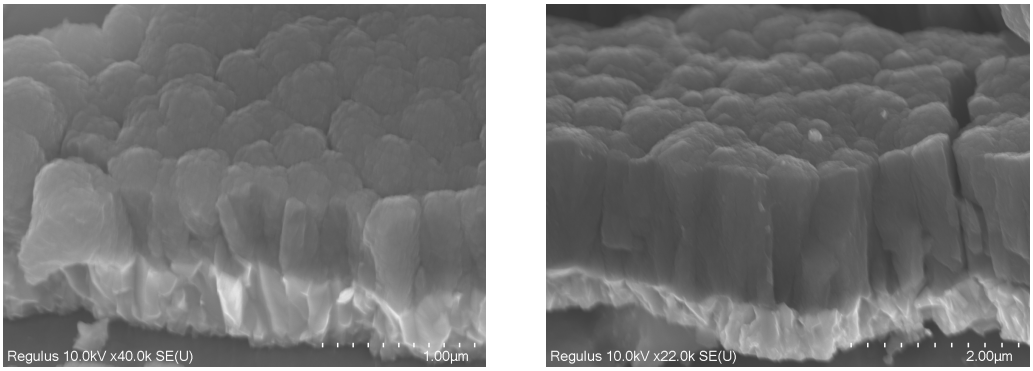

(a) 0.5 µm (b) 1.6 µm

Figure 5.20: SEM images of 80W thickness series cells

since they do not have multiple peaks. The cells deposited at a thickness of 2 µm has a peak at 2150 cm^{-1}.

5.2.4. 80W thickness series

The same thickness series was performed for a thickness of 0.5 µm, 0.9 µm, 1.5 µm, 1.65 µm and 2 µm at an RF power of 80W. The deposition parameters are mentioned in table 5.3. The cells are analyzed under the SEM, the deposition rates are measured and they correspond to the deposition rates obtained for an RF power of 80W in section 5.1.1. The cell cross-section, when viewed under the SEM, did not have a smooth surface which was found in cells that are amorphous. It can be seen in the figure 5.20a that even at a thickness of 0.5 µm the silicon has a sharp surface instead of a smooth surface. To prove this, the cells were measured under the raman microscope using a green laser over the standard range. The normalized raman intensity observed over the standard range is shown in figure 5.21. All the cells have a peak at a wavenumber of 520 cm^{-1}. This denotes that the cells are crystalline as they do not have a peak at a wavenumber of 480 $^{-1}$. The crystalline fraction calculated from the standard range raman measurement for the different thicknesses is shown in figure 5.22. It can be seen that there is an increase in crystalline fraction as the thickness increases. But as seen in the 25W and 50W thickness series of the cells, the change in crystalline fraction with the thickness is negligible.

Extended range raman measurements were made using a green laser to analyze the stretching modes of hydrogen. It can be seen in figure 5.23. The cells have a single peak which refers to non-porous high-quality material with good silicon hydrogen bonds. The cells also have the peak at a wavenumber of 2150 cm^{-1} which is found in most of the crystalline cells measured before. These results are similar to the results obtained from the aforementioned standard range raman measurement. The cells also have a peak at wavenumbers of 2350 cm^{-1} which corresponds to the silicon oxide present due to the silicon oxide in the n-layer.

Standard range raman measurements were made for the cells deposited for the thickness series using a modular raman setup and the results are discussed in the appendix A.2.

5.3. Varying silane concentration series

After analyzing the change in cell characteristics with a change in deposition power and thickness, the change in cell properties for a change in silane flow rate is analyzed. The silane flow rate is varied for the intrinsic layer. The hydrogen flow rate is kept constant throughout the deposition at 120 sccm and only the silane flow rate is varied. The silane flow rate is varied from 3.1 sccm (2.58%) to 3.9 sccm

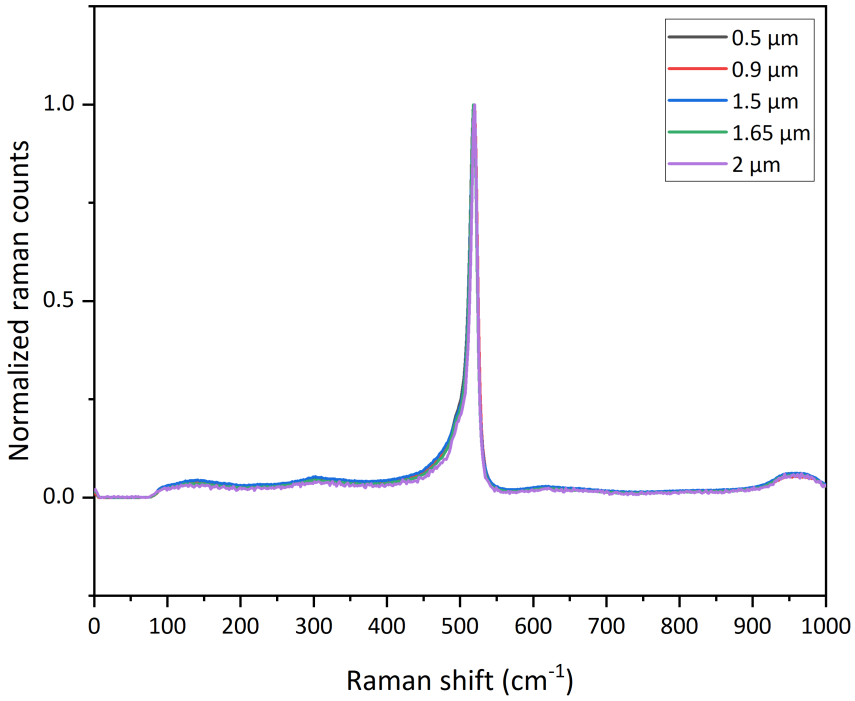

Figure 5.21: Normalized raman counts v/s raman shift for 80W thickness series measured using a green laser

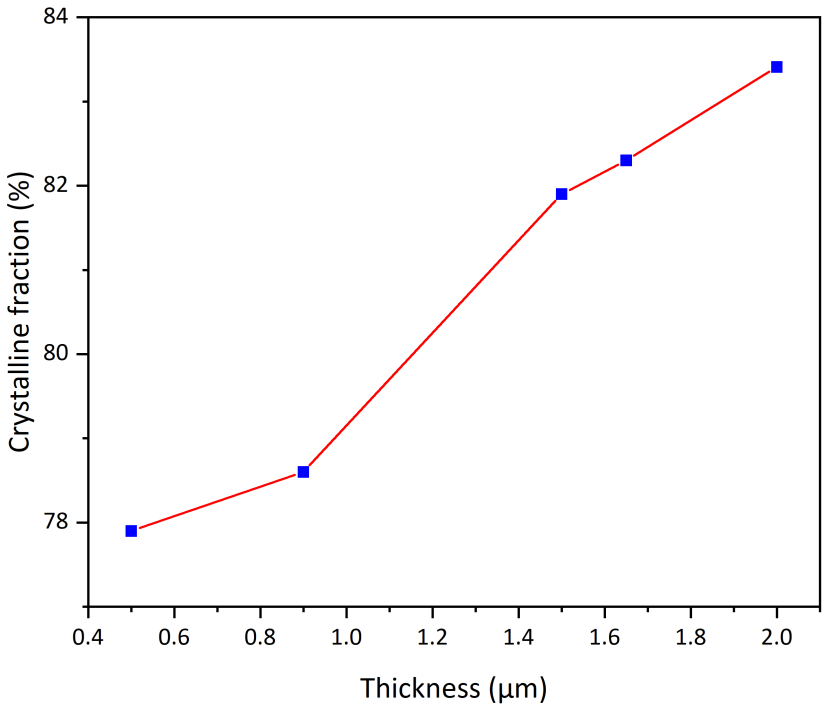

Figure 5.22: Crystalline fraction v/s thickness for the 80W thickness series

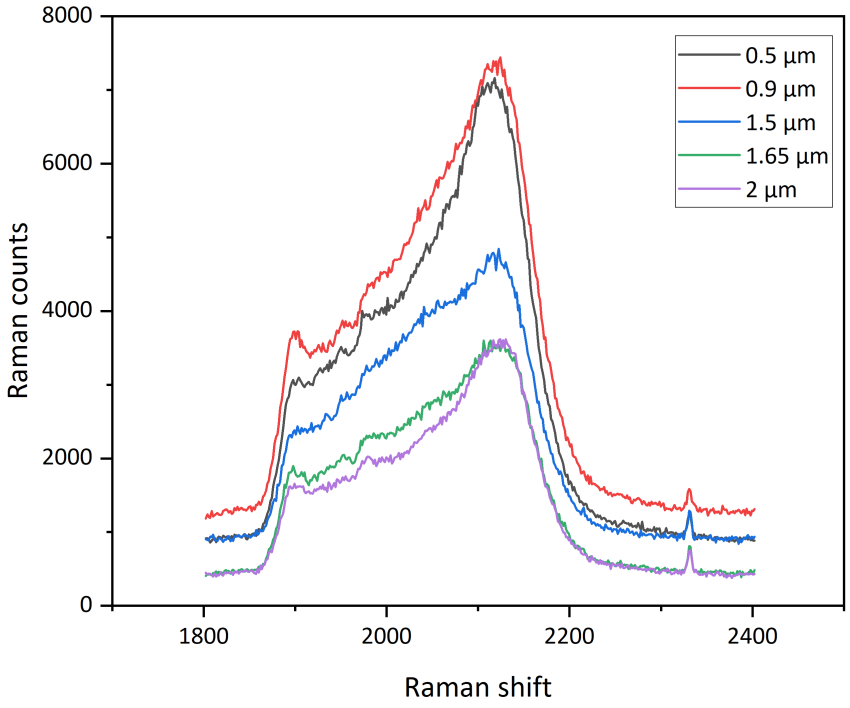

Figure 5.23: Extended range raman counts v/s raman shift for the 80W thickness series measured using a green laser

(3.25%) with an interval of 0.2 sccm. Analyzing the change in the crystalline fraction and deposition rates for a change in silane flow rate is one of the main objectives of this deposition.

5.3.1. Deposition parameters

The cells are deposited by varying the silane flow rate from 3.1-3.9 sccm as mentioned before. The RF power of deposition is kept constant at 50W throughout this series. All the other parameters were also kept constant and is mentioned below in table 5.4.

Layer	Deposition time (s)	Temperature (°C)	Pressure (mbar)	Power (W)
p-layer	1800	300	2.2	12
n-layer	720	300	1.5	11
i-layer	3810	300	4	50

Table 5.4: Silane flow rate series deposition parameters

5.3.2. Deposition rate

The cells deposited are first analyzed under the SEM. The cells observed under the SEM are shown in the figure 5.24. The height of the deposited layers is measured from the cross-sectional SEM images and then the deposition rates are calculated from it. The calculated deposition rates are then plotted against the silane flow rate as shown in figure 5.25. It can be clearly seen from the graph that there

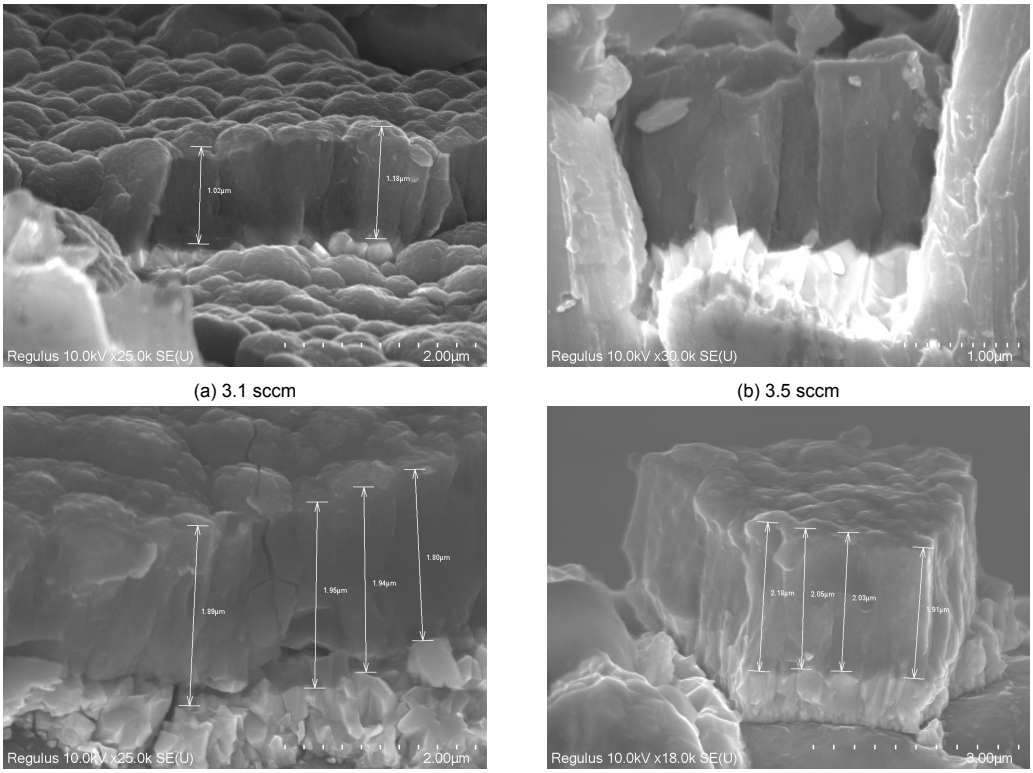

(a) 3.1 sccm (b) 3.5 sccm

(c) 3.7 sccm (d) 3.9 sccm

Figure 5.24: SEM images of the varying silane flow rate series

is an exponential rise in the deposition rate as the silane flow rate increases. Hence, increasing the silane flow rate increases the deposition rate for i-nc-Si:H.

5.3.3. Material characterization

The cross-section of the cells analyzed under the SEM is shown in figure 5.24. There is no difference in the surface of the silicon and all of them do not have a smooth surface which is characteristic of crystalline materials. The cells are also analyzed under the raman microscope using a green laser. The raman measurements was performed over the standard range and the values obtained are as shown in figure 5.26. All the cells have a peak at a wavenumber of 520 cm^{-1}. This behaviour is characteristic of crystalline silicon materials. The crystalline fraction was calculated from the standard range measurement and they are plotted against the silane flow rate as shown in figure 5.27. The crystalline fraction increases initially when changing the silane flow rate from 3.1 sccm to 3.3 sccm. Then the crystalline fraction decreases as the silane flow rate increases. The crystalline fraction is almost as low as 65% for a silane flow rate of 3.9 sccm. Hence, the crystalline fraction decreases with an increase in silane flow rate above 3.3 sccm.

The extended range raman measurements are performed under the green laser to analyze the stretching modes of hydrogen. For silane flow rates of 3.1 and 3.3 sccm the cells have multiple peaks as shown in figure 5.28. This is representative of porous material [35]. Some of the extended range measurements discussed under the section 5.2.3 also had some porous material. Both of these cells were deposited at a deposition power of 50W. The cells deposited at different RF powers do not have this porous behaviour observed in the extended range. The cells with a silane flow rate of 3.5,3.7 and 3.9 sccm do not have multiple peaks which represents non-porous material. The peaks are visible at a wavenumber of 2050 cm^{-1}. Only the materials that were characterized as amorphous in the standard range had peaks at a wavenumber of 2050 cm^{-1} in this thesis.

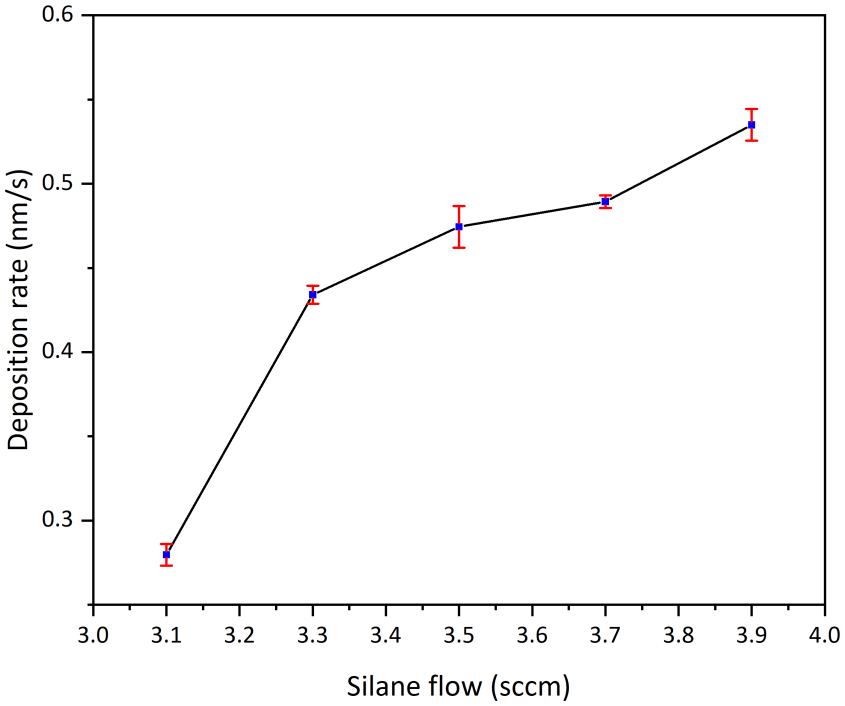

Figure 5.25: Deposition rate v/s silane flow rate for the varying silane flow rate series

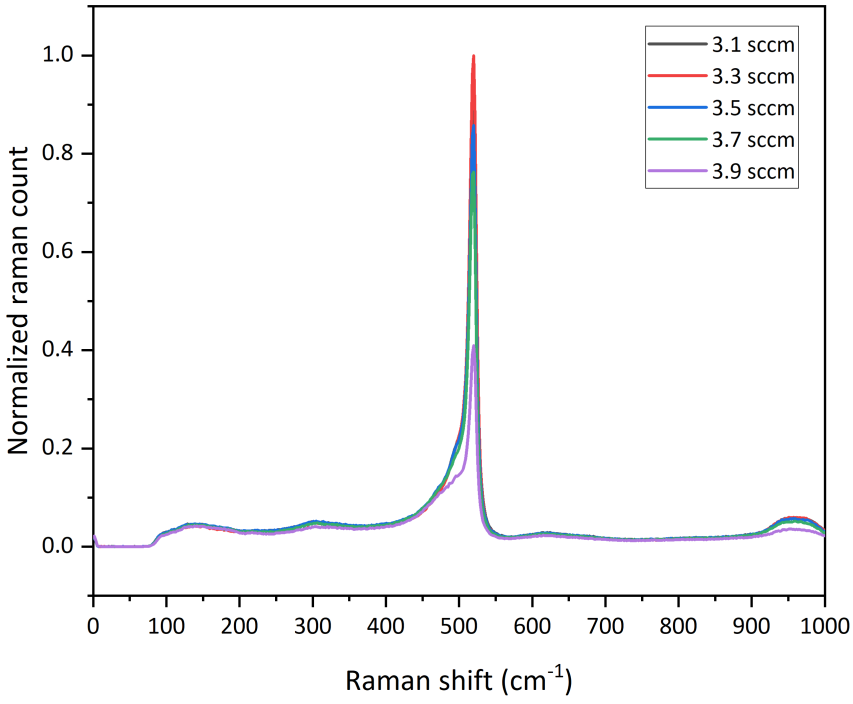

Figure 5.26: Normalized raman v/s raman shift for the varying silane flow rate series measured using a green laser

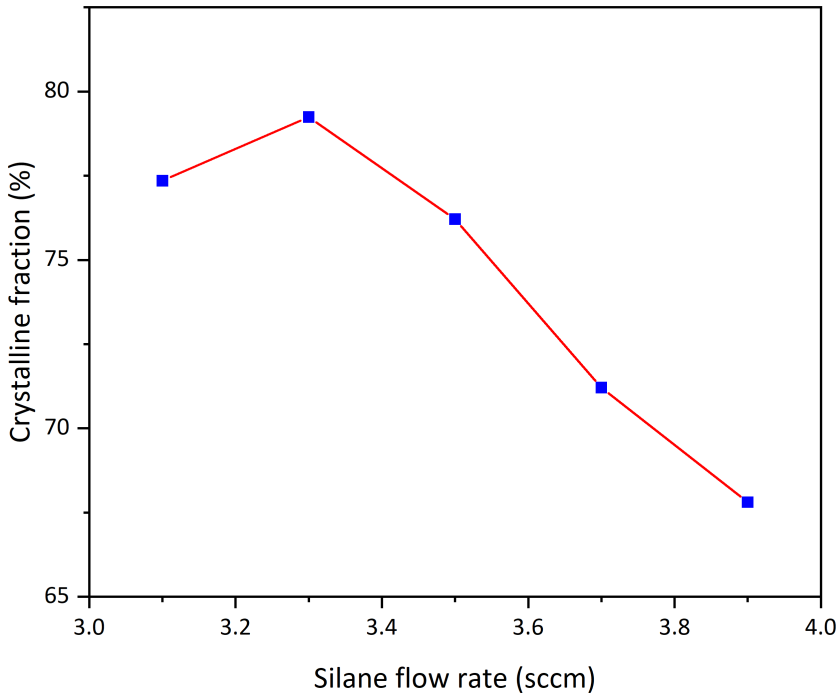

Figure 5.27: Crystalline fraction v/s silane flow rate for the varying silane flow rate series

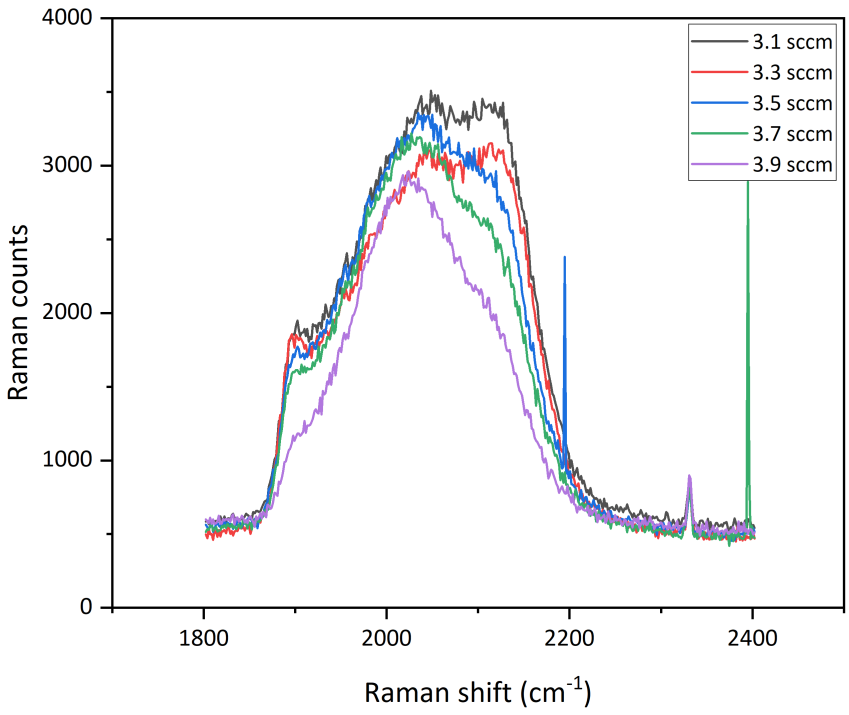

Figure 5.28: Raman counts v/s raman shift measured using a green laser for the varying silane flow rate series measured using a green laser

5.4. Processing cells at HyET solar

The p-i-n layers after deposition at TU Delft are taken to HyET solar for further processing to develop a finished solar cell. Several processing steps are performed for developing a cell module. Those steps are explained below.

5.4.1. Steps involved in the developing 1×5 cm^2 modules

The steps involved in fabricating modules is a bit different from the figure 1.3. These steps described in figure 1.3 involves the processing technique used at HyET solar for their production line. But the fabrication of 1×5 cm^2 cells is slightly different and the fabrication process is described below.

Laser scribing:
The cells after deposition at TU Delft are taken to HyET solar. The cells are first scribed to define the active area and the inactive area. The laser scribes namely P1, P2 and P4 are made. A TCO filler ink is then released at the P2 scribe to insulate the front and back contacts so that the holes and electrons are separately collected. Then a lift-off P3 ink is released to reduce the number of laser scribes as shown in figure 5.29.

Figure 5.29: Cross-sectional view of laser scribes P1,P2, P3, TCO fill ink at P2 ink and lift-off ink at P3 [24]

Sputtering:
The back contact is then deposited on top of the scribes by DC magnetron sputtering. The back contact consists of a back TCO made of 80nm thick AZO over which a 300nm thick Al back contact is sputtered. A schematic diagram of the cell after deposition can be seen in figure 5.30.

Figure 5.30: Cross-sectional view of back contact deposited on top of the scribes [24]

Removing lift-off ink:
After the back contact is sputtered the lift-off ink is removed. To remove the lift-off ink, first a layer of isopropanol (IPA) is poured into a petri dish and placed in the fume hood. Then the sample is placed in the petri dish with the back contact facing upwards. Then IPA is sprayed over the back contact and then a tissue soaked in IPA is placed over it. The cell in the petri dish is then placed under the fume hood for 10 minutes. After soaking the cell for 10 minutes in the fume hood, the lift-off ink is removed by gently rubbing the soaked tissue over the lift-off ink as shown in figure 5.31. After removing the lift-off ink, the cell is placed under the fume hood for drying.

Figure 5.31: Cross-sectional view of the cell after removing the lift-off ink [24]

Preparation of glue:
While the samples are kept for drying in the fume hood, a glue is prepared for laminating the sample. The glue consists of two components A and B. Component A is first placed in a speed mixer for 1.5 minutes at a speed of 2400 rpm to reduce its viscosity. Component A and B are mixed in a 20:1 ratio and placed inside the speed mixer again for 1.5 minutes at 2400 rpm.

Lamination:
The glue prepared in the previous step is then poured and spread over a lamination sheet. The sample is then placed over the glue. And the tissues are placed around the sample to prevent the glue from seeping through. The cell is then laminated using a hydraulic press. After the lamination, the samples are cut according to its dimension. The laminated cell configuration is shown below in figure 5.32

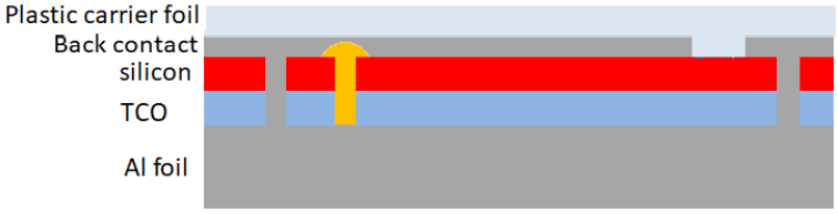

Figure 5.32: Cross-sectional view of the laminated cell [24]

Pre-etching:
The laminated cells are then pre-etched to remove 80 µm of the temporary Al substrate. The remaining 30 µm of Al substrate is removed after annealing. The solutions used for the pre-etch are as follows:

- 1.2M solution of NaOH, 5% w/w (mass of solute to mass of solution) ratio at 70°C.
- 0.92M solution of H_3PO_4, 9% w/w ratio at 70°C.
- Demi-water rinse bath

The NaOH is the main etching solution while H_3PO_4 is the acid bath used to remove the residues from etching. The demi-water is used for the final cleaning of the sample.

The sample is first dipped into the NaOH solution for approximately 6 minutes. After taking out the sample from the NaOH solution the sample is placed in the demi-water for 3 seconds before dipping the sample inside the H_3PO_4 solution for 15 seconds after which the sample is dipped back inside the demi-water bath for 3 seconds. The sample is then placed over running water and a tissue is used to clean the residues remaining on the surface from etching. The sample is then taken out of the fume hood and is placed outside for drying.

Annealing:
The pre-etched sample is sandwiched between 2 Al plates and placed into an oven for 20 minutes at 175 °C for annealing. This step is done to reduce the thermal shock on the cell layers as the temporary Al substrate is etched away. Failing to perform this step may lead to excessive cracks in the solar cell layers. After annealing, the cells are left to cool for at least 40 minutes.

Final etch:
Once the sample is cooled down after annealing, the samples are cut according to the required dimensions and cellophane tape is placed over the front contact to prevent them from etching. The sample is then placed into the same NaOH solution used during the first etch. The sample is kept inside the NaOH solution until the temporary Al substrate is completely etched away. After the temporary Al substrate is etched away, the sample is immediately taken out of the NaOH solution and dipped into the demi-water bath for 3 seconds. Then the sample is dipped into the H_3PO_4 solution for 15 seconds before dipping it back inside the demi-water bath for 3 seconds. The sample is then placed over running water and a tissue is used to remove the excess residue left on the surface of the sample after etching. The etched sample is then taken out of the fume hood and left out to dry. The final module obtained after the final etch is shown in figure 5.33.

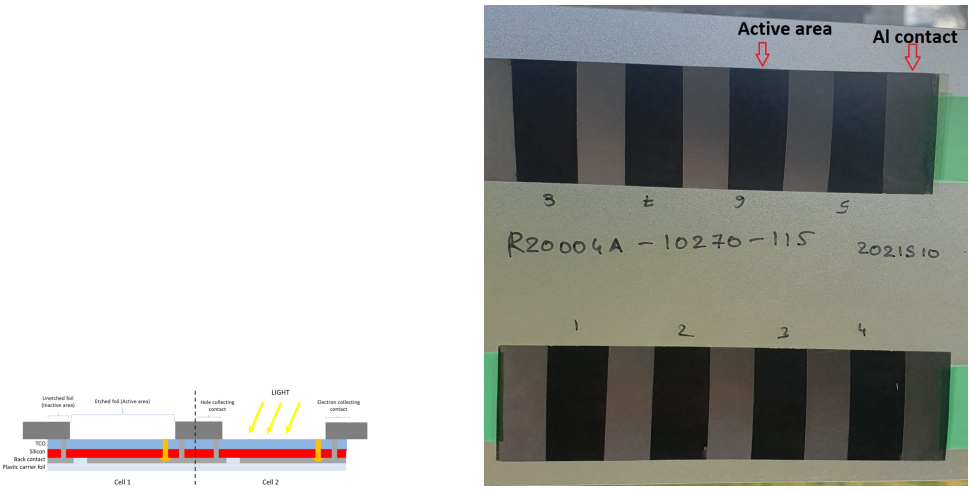

(a) (b)

Figure 5.33: Final processed module: (a) Cross-sectional view of the finished modules obtained [24] (b) labelled image of the processed modules

5.4.2. Steps involved in the creation of Super CoF cells

Since the previous technique was time-consuming and some processing steps had some bottlenecks due to the unavailability of the machines as they were used in the production line, a new technique to process cells had to be developed to reduce the bottlenecks. So, the super copper on foils (CoF) technique was used to process the cells. The processing is almost similar to 1×5 cm^2 modules developed, but some processing steps are different and are explained below.

Sputtering:
The cells are directly sputtered without scribing in this technique. First, an 80nm thick back TCO (AZO) is deposited. Then masks are placed over cells and then the back contact Al is sputtered. 20 cells can be deposited on a sample using the masks which contain 10 cells with an area of 0.99 cm^2 and the remaining samples have an area of 0.44 cm^2.

Copper as back contact:
Dark JV measurements are then performed on all the cells deposited and the cells which display diode behaviour are noted. The copper strips are then placed on the cells that display diode behaviour. The copper strips are placed in such a manner that the copper does not touch the temporary Al substrate. A plastic foil is placed underneath the copper strips to prevent the copper strips from contacting the temporary Al substrate.

The cells are again measured under the dark to check the diode behaviour. Then comes the preparation of glue, lamination and all the steps that follow are similar to steps followed after removing lift-off

ink in section 5.4.1. After lamination, the cells are cut according to their shape and then the first etch is performed. Then the cells are annealed after which the final etch is performed. The processed super CoF cells is shown in the figure 5.34. In this super CoF processing, the cells are measured under JV after every processing step, which makes it easier to analyze processing steps, and helps in further optimization of the process.

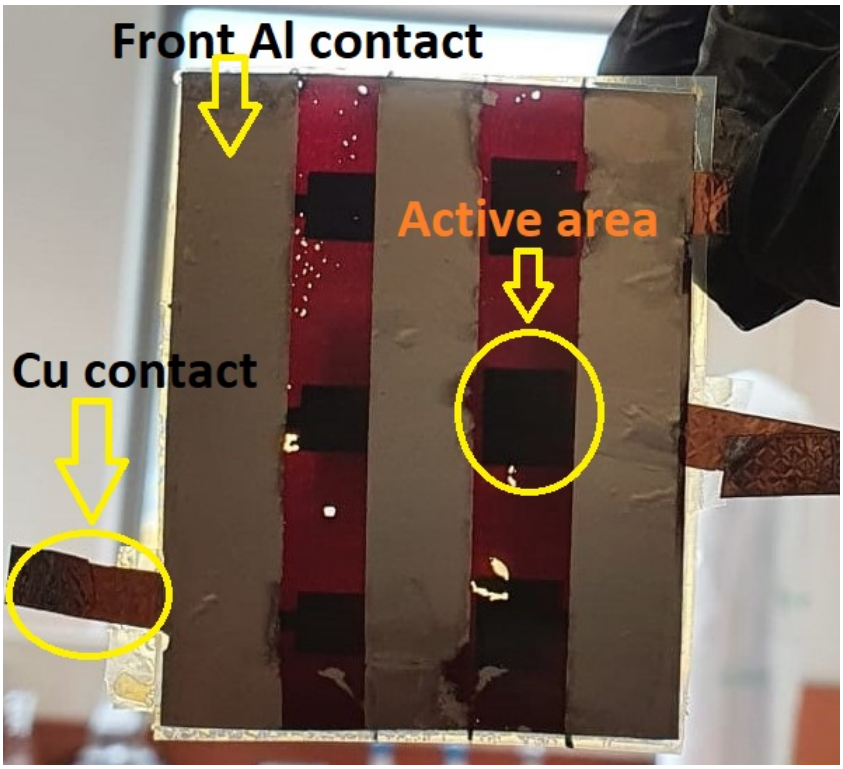

Figure 5.34: Labelled image of a processed super CoF sample

5.4.3. 40W thickness series

From the aforementioned results, the cell with a deposition power of 40W had an ideal crystalline fraction of 68.4% and the cell characteristics did not change with an increase in thickness of the i-layer. So, for processing the first set of cells at HyET, five cells with an i-layer thickness of 1 µm, 1.5 µm, 2µm, 2.5µm and 3 µm are deposited with a deposition power of 40W. Other deposition parameters are mentioned below in the table 5.5. The silane and hydrogen flow rates are kept constant at 3.3 and 120 sccm respectively.

Layer	Deposition time (s)	Temperature (°C)	Pressure (mbar)	Power (W)
p-layer	1800	300	2.2	12
n-layer	720	300	1.5	11
i-layer	2723-7070	300	4	40

Table 5.5: Power series deposition parameters

The cells are then processed into modules as described in section 5.4.1. Eight 1x5 cm^2 modules were developed per sample, and hence a total of 40 samples were developed. The cells are then electrically characterized using dark JV and illuminated JV.

The cells were first measured under dark to check if the cells display diode behaviour or if the cells are shunted. All the 40 samples measured using the dark JV setup were shunted and the respective

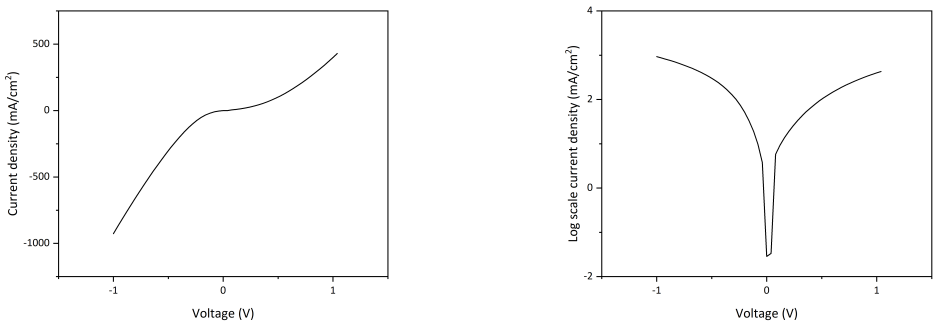

Figure 5.35: (a) Current density v/s voltage graph for the 40W thickness series (thickness: 2 µm) cell measured in dark, (b) Log scale current density v/s voltage graph for the 40W thickness series (thickness: 2 µm) cell measured in dark

curves obtained are shown in the figure 5.40. We can clearly see in the figure 5.35a at V = 0V the slope is very low. This indicates that shunt resistance is low. All the cells were shunted as the remaining modules also had a very low slope at V = 0V.

The cells are also measured under illumination and the results were recorded. The cell performance was very poor as they are shunted.

After the electrical characterization of these cells, it was clear that these cells were shunted. The cells are then optically characterized using SEM and raman to analyze cause of shunts. SEM imaging of these cells was performed to check if the final etch has destroyed any part of the sample which may have lead to shunts. But from the figure 5.36 the front TCO, silicon layer and the back TCO are clearly visible. The SEM imaging was difficult to perform and is not as clear as the SEM images of an unprocessed cell. The glue used for laminating the cells is conductive and scatters the reflected electron beam. Scattering leads to distorted images. To counter this efect, the incident electron beam was reduced to lower electron voltages of 1eV so that images can be viewed under the microscope. Since the cells in figure 5.36 were measured at low electron voltages the images are not as clear as the SEM images of the unprocessed cells which were viewed at higher incident electron voltages.

The raman measurements were also made to check the presence of silicon in the cells. The standard range measurements showed that the cells were crystalline as shown in figure 5.37. It can be clearly seen that there is only one peak at a wavenumber of 520 cm^{-1} and the cell is crystalline. It can be confirmed from the crystalline fraction calculation as shown in the figure 5.38. The cells are most definitely crystalline. The cells also have an optimal crystalline fraction which is used in device grade materials (approximately 60%) [8]. The crystalline fraction of the cell processed at 40W has a lower crystalline fraction than the crystalline fraction obtained for a 40W unprocessed cell in section 5.1.1.

Extended range raman measurements were made to check the stretching modes of hydrogen and the presence of silicon and its oxides. As shown in the figure 5.39 all the cells have a peak around 2050 cm^{-1} except the cell with 2.5 µm. This confirms the presence of silicon hydrogen. At a wavenumber around 2030 cm^{-1} the cells have a small peak which indicates the presence of silicon oxides. The cell with a thickness of 2.5 µm is crystallized completely, hence the peak is not visible.

The raman and the SEM results have shown that the cells have survived the final etch and the silicon layers and TCO is still present in the cell. So, the shunts are not caused due to etching.

5.4.4. Analysis of deposition

The processed cells were shunted and the etching also did not damage the cell. To analyze what is causing the shunts, first the deposition was analyzed to check if the cells have diode behaviour or if the cells are shunted right after the deposition. This is done by depositing smaller back contacts with masks as shown in figure 5.40. The deposition parameters are similar to the parameters in table 5.5. After the deposition of the p-i-n layers on top of the Al substrate cells, back TCO (AZO:80nm) and back

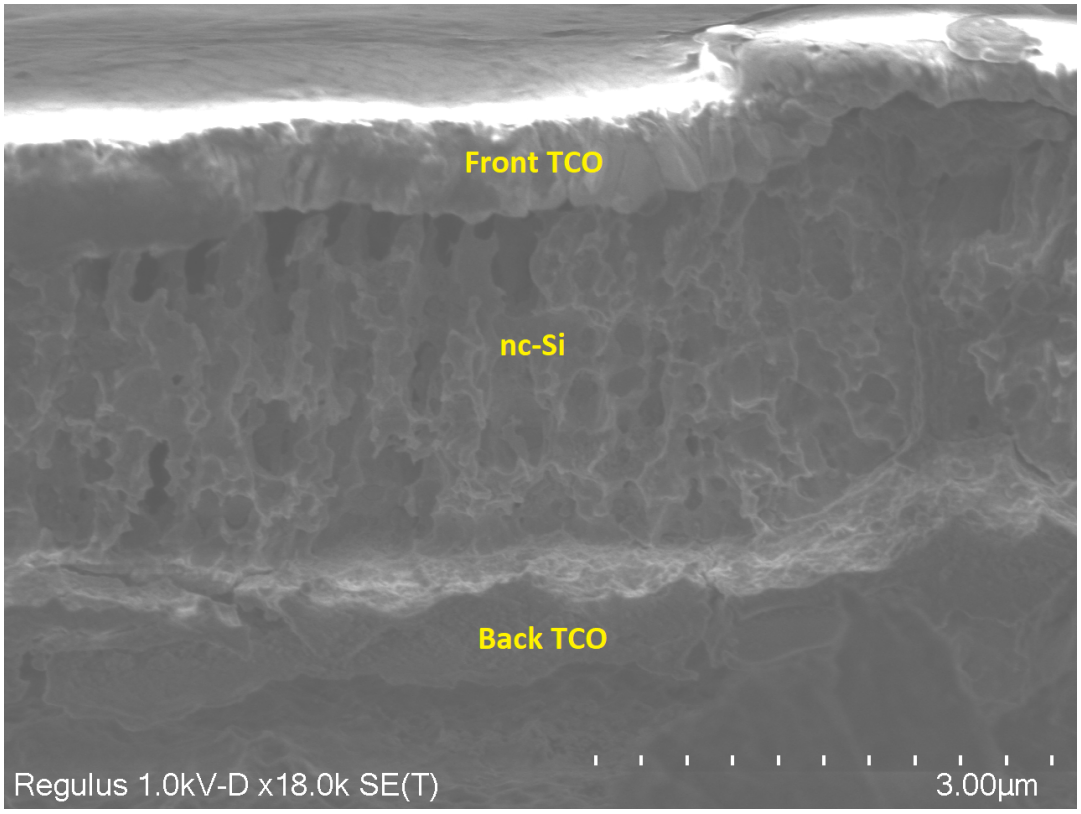

Figure 5.36: Labelled SEM image of a processed cell

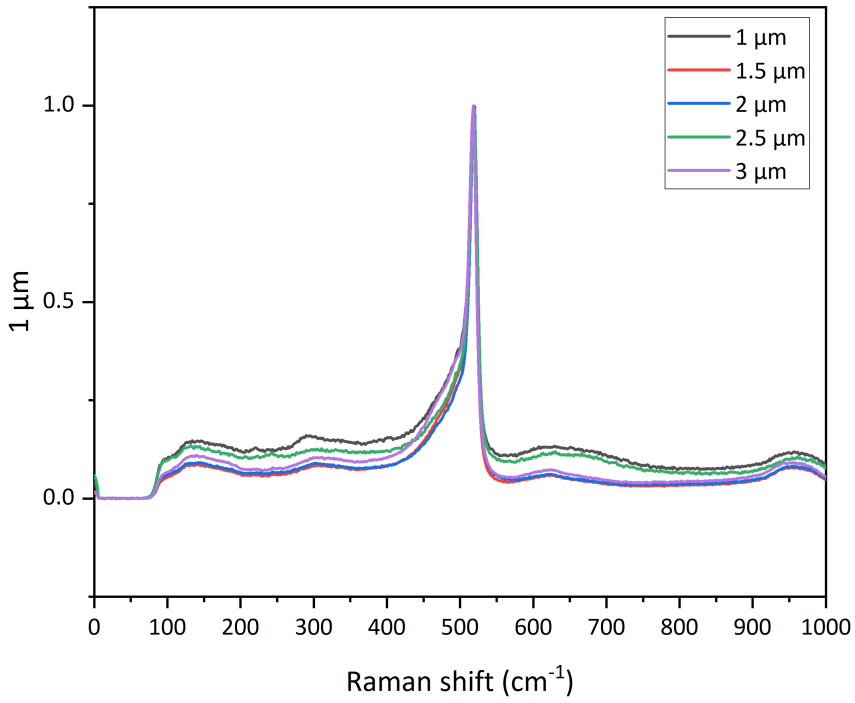

Figure 5.37: Normalized raman counts v/s raman shift for the 40W thickness series of processed cells measured using a green laser

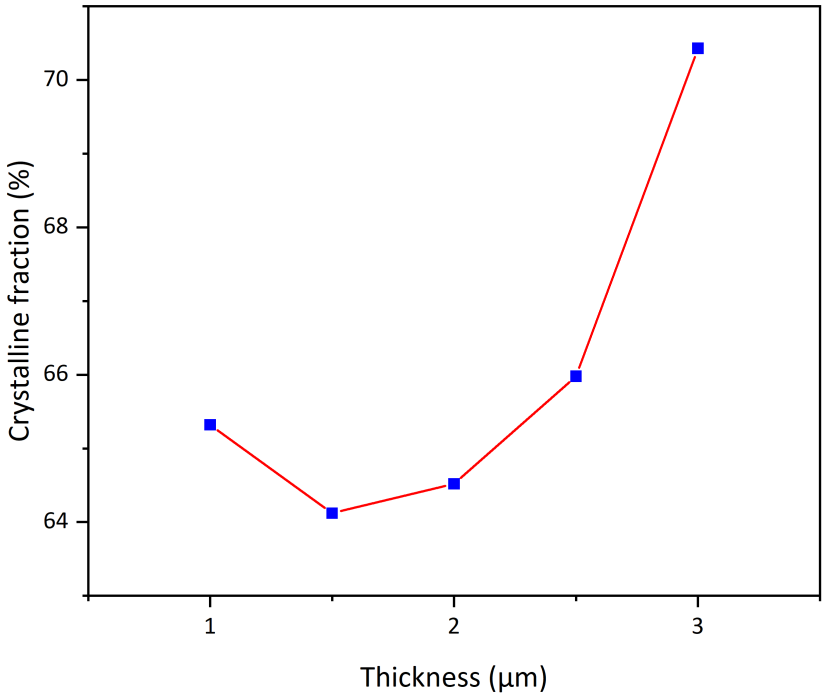

Figure 5.38: Crystalline fraction v/s thickness for the 40W thickness series of processed cells

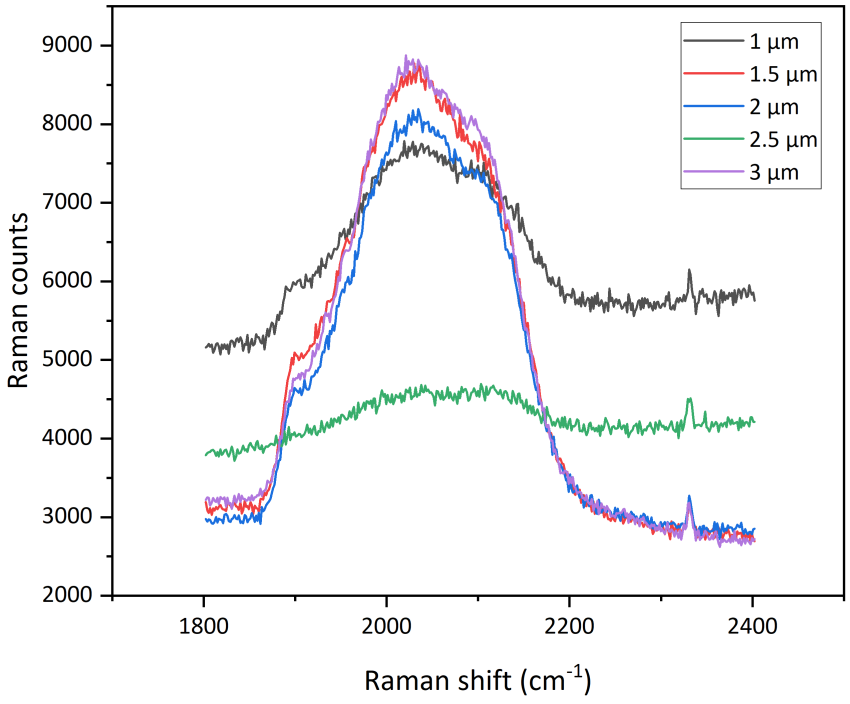

Figure 5.39: Raman counts v/s raman shift for the 40W thickness series of processed cells measured using a green laser

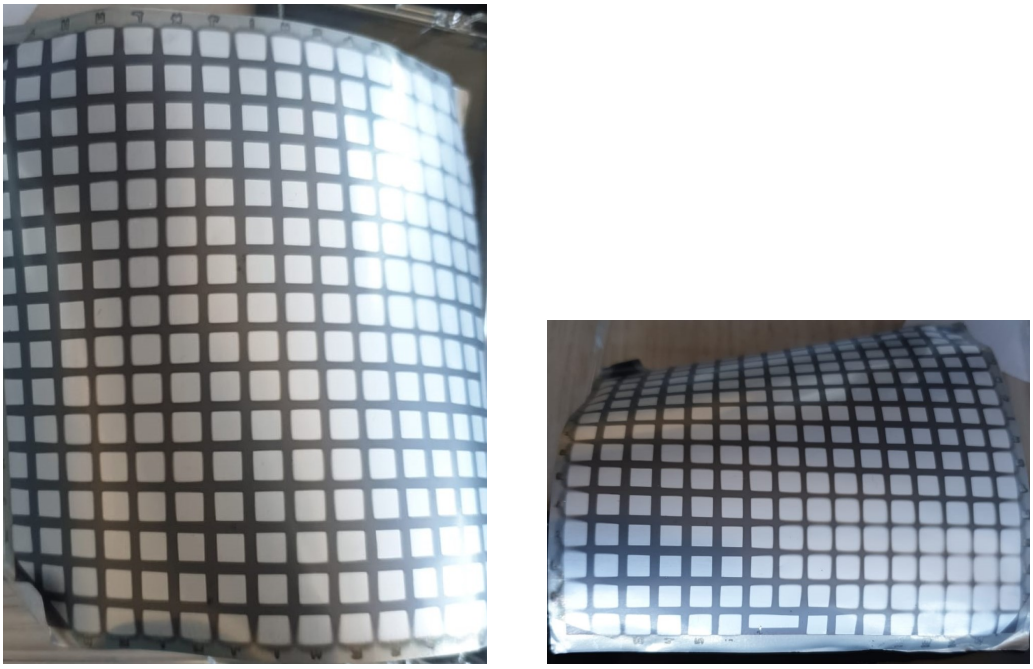

(a) (b)

Figure 5.40: Images of masks used to deposit back contacts to check diode

contact Al was sputtered (300nm). The cells after the deposition of back contacts are measured in dark.

Most of the cells measured in dark were shunted. Only two out of 392 cells deposited displayed diode behaviour as shown in figure 5.41. Almost all of the cells were shunted. Hence, the shunts are caused due to deposition of the p,i or n layer.

Some deposition parameters have to be changed to remove the shunts. The presence of nc-SiO_x:H visible in the raman measurements may have been the reason for shunts. So cells with amorphous n-layers (a-Si:H) were deposited with diodes to check if varying the n-layer configuration reduces the shunts. Different configurations for the n-layer deposition were carried out as shown in figure 5.42. The deposition parameters for p, i and n crystalline layers deposited are the same as per the parameters mentioned in table 5.5. The deposition parameters for the amorphous n-layer deposited is mentioned in table 5.6.

Layer	Deposition time (s)	Temperature (°C)	Pressure (mbar)	Power (W)
n-layer	825	300	0.6	4

Table 5.6: Amorphous n-layer deposition parameters

Similarly back contacts were deposited with masks for these configurations with amorphous n-layers. The cells were measured under dark to check their electrical properties. The cell configurations with crystalline n layer had lot of shunts and the rest of the cells had a breakdown which may be due to a problem with the machine rather than the cells. Most of the cells with just an amorphous n-layer also had a lot of shunts but 3 out of 192 cells displayed diode behaviour as shown in figure 5.43.

To further analyze the error in deposition, the thickness of the amorphous n-layer in the p-i-n(a) configuration cell was increased to 80nm. The new configuration deposited is shown in figure 5.44. The deposition parameters are similar to the parameters mentioned in the table 5.6 except for the deposition time in the n-layer, to account for the increase in thickness of deposition. The back TCO and Al were deposited with masks. The cells were measured under dark and almost half of the cells displayed diode behaviour as shown in figure 5.45 and the rest of the cells were shunted.

Since half the cells displayed diode behaviour when measured in the dark, the cells with the same deposition parameters were deposited and processed using the super CoF technique as mentioned in

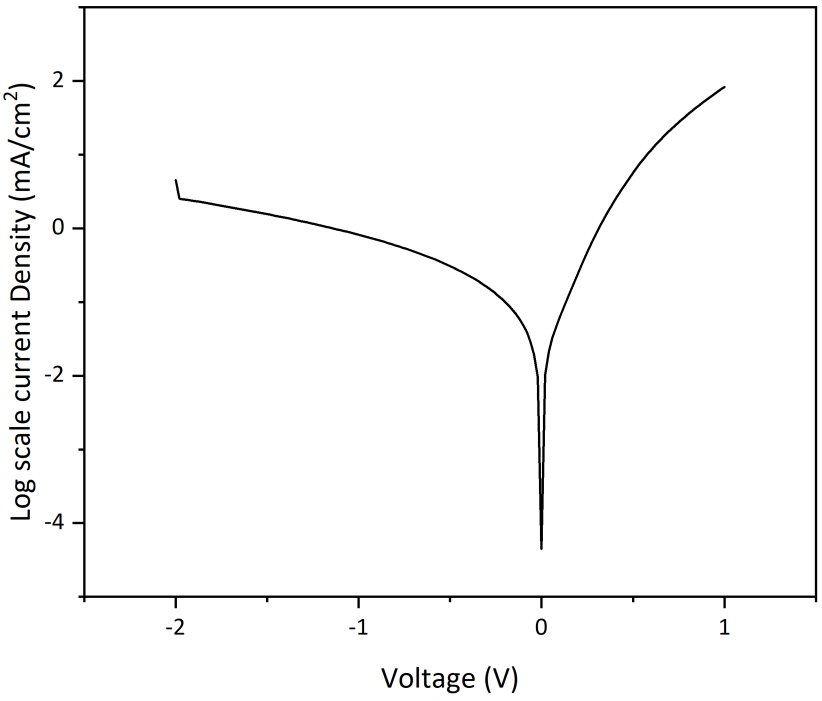

Figure 5.41: Dark JV curves of the crystalline silicon cells deposited with back contact masks

section 5.4.2. 20 cells were deposited in this sample. The sample was measured in dark after every processing step. 7 out of 20 cells deposited displayed diode behaviour initially as shown in figure 5.46a, the remaining cells were shunted. Even after all the processing steps, the cells that displayed diode behaviour initially continued to do so even after the final etch. The dark JV curves obtained for the cells before and after processing are shown in figure 5.46.

The JV measurements were then made under illumination at AM1.5 spectrum and the following results were unsatisfactory. Very low short circuit current and shunt resistance was obtained . Quantum efficiency measurements were also made for these cells to analyze the spectral response of the cell. The EQE vs wavelength curves obtained for most of the cells were similar and as shown in figure 5.47.

After some positive results with a thicker amorphous n-layer, the thickness of the n-layer was reduced to 60 and 30nm and some cells were processed. Cells were deposited using the same parameters as mentioned in table 5.5 and 5.6. Only the deposition time was changed according to the desired thickness. These cells were processed using the same super CoF processing steps. All the cells with a-n-layer thickness of 30nm were shunted when measured under dark while only 2 out of 20 cells displayed diode behaviour for the sample with a n-layer thickness of 60nm. Hence the cells that display diode behaviour in dark increases with the increase in the thickness of the amorphous n-layer. Further analysis performed on improving the electrical performance of the cell is mentioned in the appendix A.3.

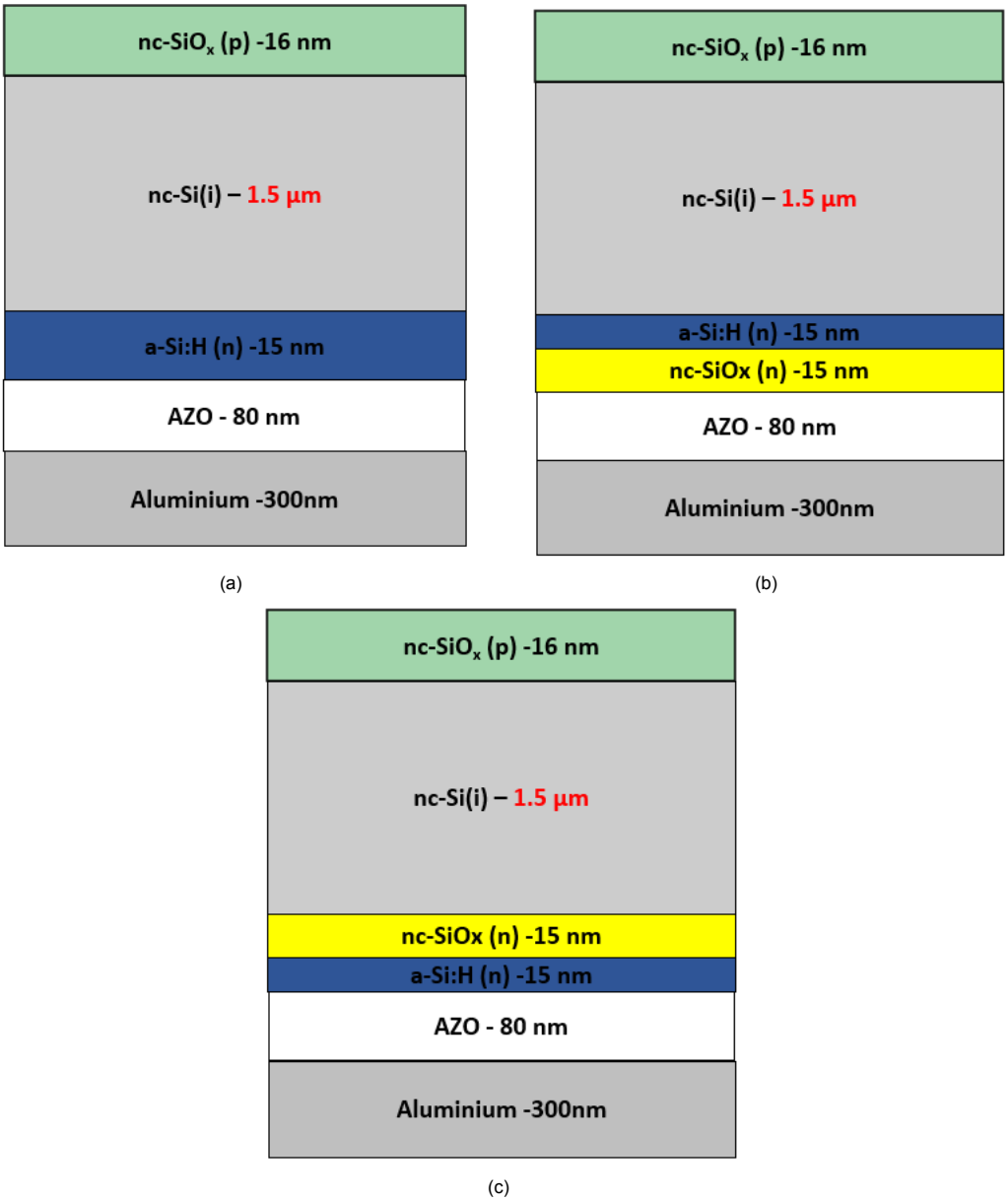

Figure 5.42: Cell deposition configurations of crystalline silicon used for analyzing the deposition: (a)p-i-n(a) (b) p-i-n(a-nc) (c) p-i-n(nc-a) configuration [42]

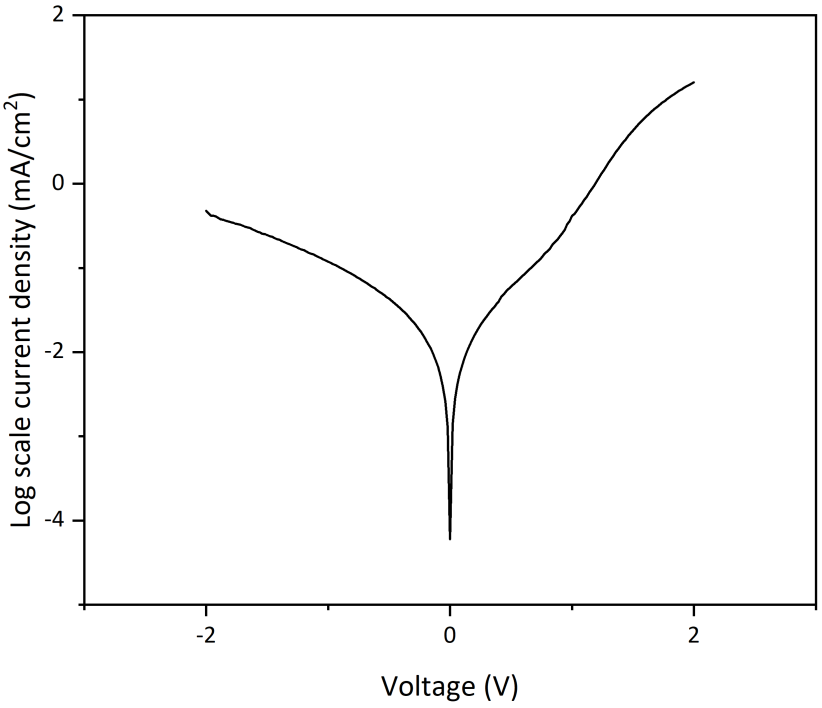

Figure 5.43: Dark JV curve of the p-i-n(a) cell with diode behaviour

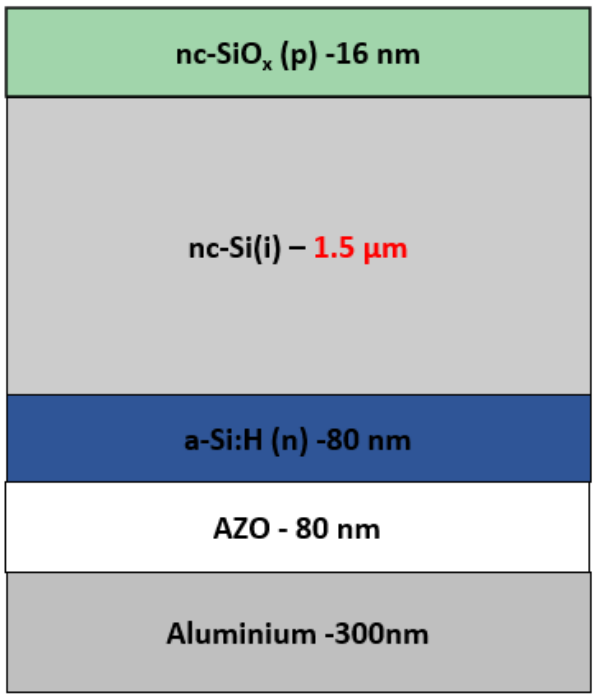

Figure 5.44: Cell configuration of p-i-n(a) crystalline silicon cell

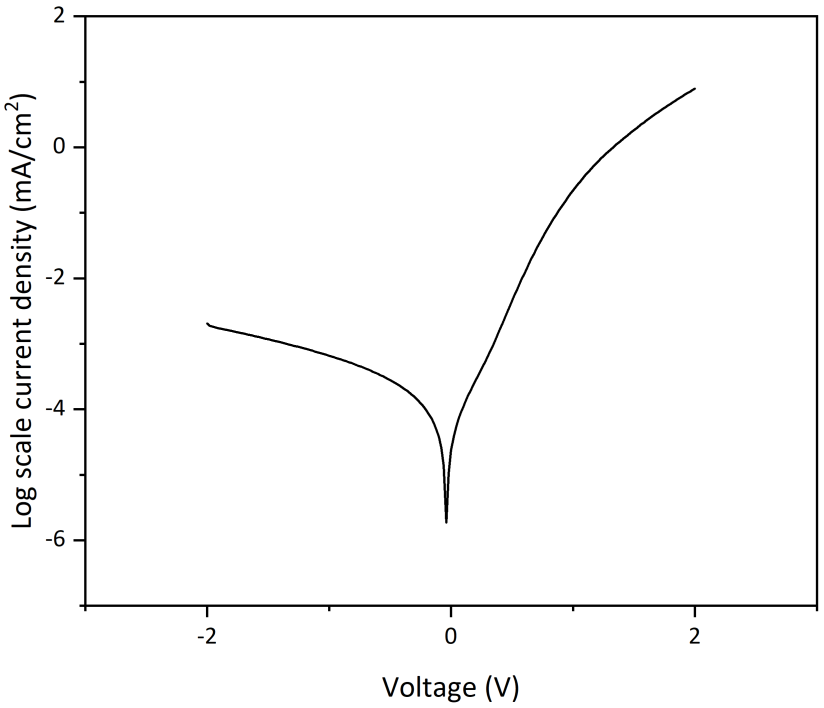

Figure 5.45: Dark JV of crystalline cells with p-i-n(a) configuration, with an n-layer thickness of 80nm

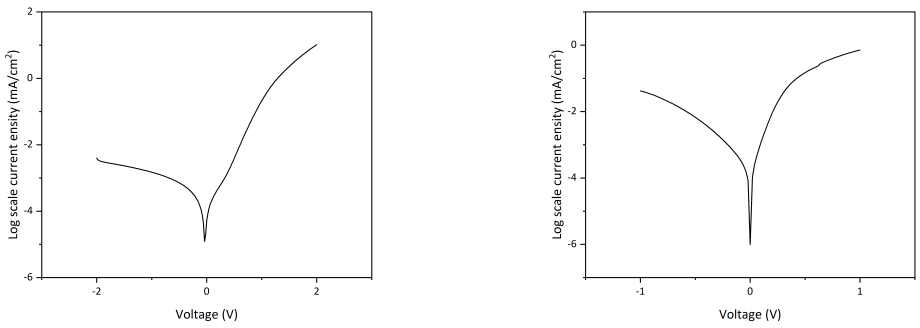

(a) (b)

Figure 5.46: Dark JV of crystalline super CoF cells with p-i-n(a) configuration, with an n-layer thickness of 80nm: (a) Dark JV before lamination (b) Dark JV after final etch

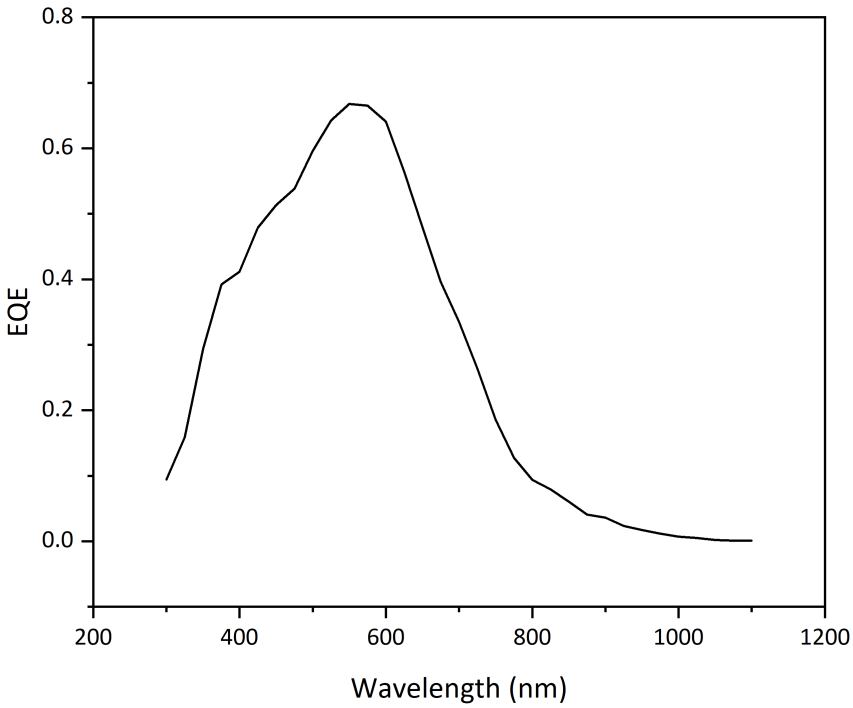

Figure 5.47: EQE v/s wavelength of the super CoF cells with p-i-n(a) configuration, with an n-layer thickness of 80nm

6

Conclusion and recommendations

In this thesis work, nanocrystalline silicon single-junction thin-film solar cells have been developed and the deposition parameters have been optimized. The key findings from this thesis study are summarized in this chapter and are in accordance with the research questions established in section 2. Section 6.1 presents the key conclusions, followed by section 6.2 where recommendations for future research on crystalline thin-film single-junction devices on Al substrate is discussed.

6.1. Conclusion

The first objective was to determine the optimal RF power of deposition for the intrinsic layer in a crystalline single junction cell. The depositions were performed from an RF power of 25W till 80W. From the standard range raman measurements made using a green laser, it was observed that at an RF power of 25W, the cells were amorphous in nature. As the deposition power reaches 40W there is a transition from amorphous to crystalline material. Hence, another set of experiments were performed with the deposition power ranging from 35-45W. The transition from amorphous to crystalline material happens at 38W but the cell with 40W deposition power had the optimal crystalline fraction. The deposition rates of the cells were also measured to find the optimal RF power of deposition with high deposition rates. The deposition rate increased with an increase in deposition power. Ideally, a cell with the highest deposition power (80W) would have the optimum deposition rate. But the cell at 80W has a very high crystalline fraction which is not ideal for producing device grade materials. Hence, the optimum deposition power was chosen to be 40W which had an ideal crystalline fraction and high deposition rates of 0.41 nm/s. For the aforementioned depositions, standard range raman measurements were made using a green laser on those cells. The corresponding crystalline fraction was calculated from the raman measurements and it was observed that with the increase in RF power of deposition the crystalline fraction also increases. The cells with 25W power of deposition had a very low crystalline fraction of 3.2%. There is an exponential shift in the crystalline fraction to 53.4% for a deposition power of 30W. The crystalline fraction then has a lower rate of increase due to increase in deposition power. It can be concluded that with the increase in RF power of deposition, the cell crystalline fraction and deposition rate increase. The material properties also vary for a change in deposition power.

For the second objective, to analyze the change in cell characteristics for a change in cell thickness, cells with different thicknesses of intrinsic layer ranging from 0.5 µm and 2 µm were performed for a deposition power of 25W, 50W and 80W. The raman measurements were made in the standard range using a green laser for all thicknesses and the cell properties were similar for all the thicknesses for the respective RF power of deposition. The crystalline fraction calculated from the standard range raman measurements is also similar for all thicknesses for the respective deposition power. The deposition rates were also measured and even the deposition rates do not change with the increase in thickness. The stretching modes of hydrogen were measured by making extended range raman measurements

using a green laser. The stretching modes of hydrogen measured also did not change with the increase in thickness. Hence, increasing the cell thickness do not change any optical characteristics of the cell.

For the third objective, the change in cell characteristics with a change in the silane flow rate in the intrinsic layer was observed. The silane flow rate is varied from 3.1 sccm to 3.9 sccm while the hydrogen flow rate was kept constant at 120 sccm. The cells were characterized by making raman measurements using a green laser in the standard and extended range. The cell characteristics varied slightly in the standard range with an increase in silane flow rate. To confirm this, the crystalline fraction was also calculated. The crystalline fraction increased initially by varying the silane flow rate from 3.1 sccm to 3.3 sccm after which the crystalline fraction reduced for an increase in silane flow rate. The deposition rates also increase with an increase in silane flow rate. To conclude, the crystalline fraction and deposition rates change with a change in silane flow rate. Since the crystalline fraction change due to a change in silane flow rate, the material properties will also change with a change in silane flow rate in the i-layer.

For the fourth objective, the crystalline single-junction cells were never processed before on flexible Al substrates. The cells were processed into modules and the cells survived the final etch but they were shunted. To analyze the shunts, the back contact was deposited with masks to analyze the cell JV characteristics in dark. The cells turned out to be shunted. The cell deposition parameters were varied to check if changing the cell deposition in the n-layer changes the cell properties. Different configurations are deposited with the masks to analyze the cells under dark, and the cells were still shunted. The thickness of the n layer was then increased to 80nm to check if these cells display diode behaviour in dark. The cells displayed diode behaviour for a p(nc-SiO_x:H)-i(nc-Si:H)-n(a-Si:H) configuration with a n-layer thickness of 80nm. The JV characteristic of the cell under AM 1.5 illumination was unsatisfactory. So, the thickness of the n-layer was reduced to 60nm and 30nm as decreasing the size of the doped layer can improve the electrical performance of the cell. These cells measured under dark was shunted. So, the cells with a configuration of p(nc-SiO_x:H)-i(nc-Si:H)-n(a-Si:H) with an n-layer thickness of 80nm and i-layer thickness of 2 µm is the ideal cell deposition parameter for the single junction crystalline cells.

For the fifth objective, from the aforementioned optical characterization made for the thickness series, the crystalline fraction and deposition rate of the cell do not change with the thickness of the i-layer. So, the optimum cell thickness and deposition time are determined from the cell performance of the processed cells. The optimum thickness for the p-layer is 16nm with a deposition rate of 0.03 nm/s. The optimum i-layer thickness was determined to be 2 µm with a deposition rate of 0.41 nm/s. The optimum n-layer thickness is yet to be determined. But for the experiments performed within the time frame of this thesis, the optimum thickness of the amorphous n-layer was found to be 80 nm with a deposition rate of 0.097 nm/s.

6.2. Recommendations

In this section, some recommendations for future research on nc-Si single-junction cells are suggested. Owing to the lack of time available, these options could not be explored during the thesis research.

Firstly, the electrical properties of the single junction crystalline cell can be improved. In this thesis work, cells that display diode behaviour were created but the performance of the cell under illumination was poor. This may be due to the processing or the deposition as well. The deposition conditions apart from the deposition thickness have been optimized. Hence further optimizing the deposition thickness of layers can significantly improve the performance of the single junction cell which can be later implemented onto a tandem cell as the bottom layer.

Secondly, the processing techniques at HyET solar have to be critically analyzed. The copper contacts in the super CoF cells do not stick to the surface and most of the working cells does not seem to be connected post-processing. And the bottlenecks in processing the cells are very high. An alternate method to develop cells at TU Delft has to be implemented to further improve the research in this subject. Hence this can be implemented by depositing the back contact by metal evaporation using the same masks used at HyET. The new back contact consists of silver (300nm), chromium (30nm) and aluminium (800 nm) on top of the 80 nm AZO. This would reduce the processing time for the cells.

The cells can then be laminated, annealed and etched using the facilities available at TU Delft.

Finally, experiments on cells with high silane flow rate and high deposition power in the intrinsic layer can be analyzed. The cells with an ideal crystalline fraction (around 60%) can have higher deposition rates in comparison to the deposition rates obtained in the current production line by increasing the deposition power and silane flow rate until the ideal crystalline fraction is obtained.

A

Appendix

A.1. Power series

For the power series performed as mentioned in section 5.1 some extra measurements were made which support the results mentioned in section 5.1. These results are mentioned below

A.1.1. Initial deposition

For the power series, raman measurements were initially made using raman spectroscopy with a beam splitter. There was a lot of noise that was recorded in the measurements. Raman measurements were also made for the same using a modular raman setup which is not ideal. The results obtained in the standard range for these cells are as shown in figure A.1. The results obtained from these standard range raman measurements are analogous to the results obtained in the raman results mentioned in section 5.1.1. At lower RF power of deposition, the cells are amorphous while the cells above 40W are crystalline. The crystalline fraction obtained from the measurements made with the raman spectroscopy used with a beam splitter is shown below in figure A.2. The crystalline fraction results are also similar.

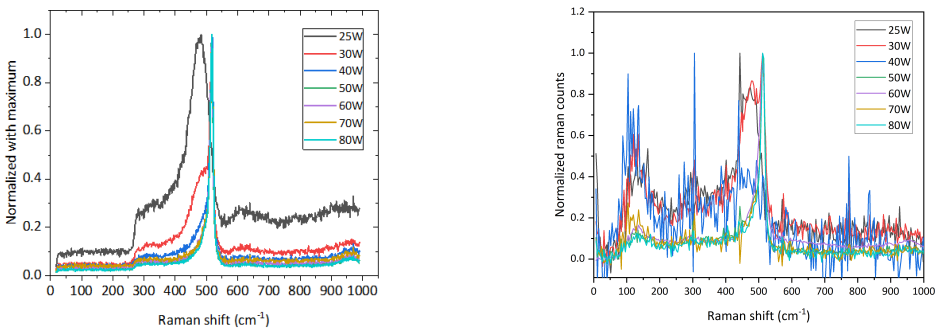

(a) (b)

Figure A.1: Standard range raman results measured using green laser: (a) Beam splitter raman (b) Modular raman

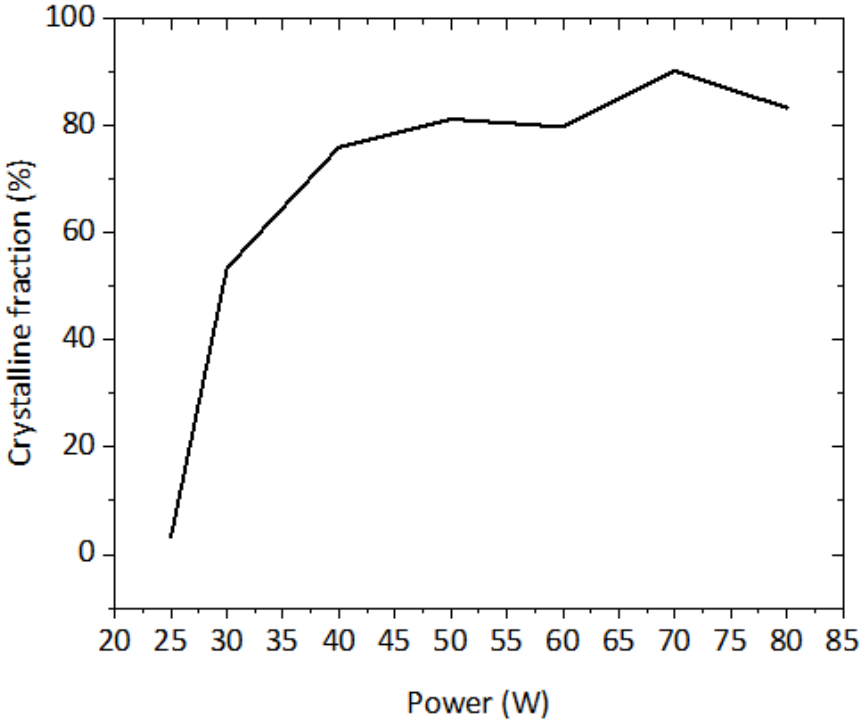

Figure A.2: Crystalline fraction v/s power of deposition for the power series measured using a beam splitter raman microscope

A.2. Thickness series

The standard range raman measurements were also made for the thickness series using a modular raman setup. The standard range raman results obtained for the thickness series are shown in figure A.3. The 25W,50W and 80W thickness series cell characteristics is similar to the cell characteristics obtained using raman as mentioned in section 5.2.

A.3. Processed cells

Apart from the experiments mentioned in section 5.4.4, some more depositions were made to analyze the shunts in the cell. Cells were alternatively deposited on Asahi glass to check if the shunts are caused due to the substrate. Simultaneously, depositions were made on temporary Al substrate as well. Simultaneous depositions are performed to compare the deposition on different substrates. The front TCO was already deposited on the Asahi glass. First, a thin line of Al (300nm) was deposited on one side of the glass (TCO side) as front contact. Later the crystalline silicon with configuration p-i-n(a) is deposited on top of the TCO and front contact. The deposition parameters are similar to the parameters mentioned in table 5.5 and 5.6. For glass, different back contacts were deposited than the standard AZO (80nm) and Al (300nm). The back contacts for glass is deposited using metal evaporation and it contains 300nm of silver, 30nm of chromium and 800nm of aluminium. The cell deposited on glass is shown in figure A.4.Similar back contacts were also deposited on the Al substrate. The cells were then measured under dark and almost all the cells were shunted or had very low current density.

The cells were then deposited using the p-i-n superstrate configuration with a crystalline n-layer. depositions were made on Asahi glass and Al substrate. The cell deposition parameters are similar

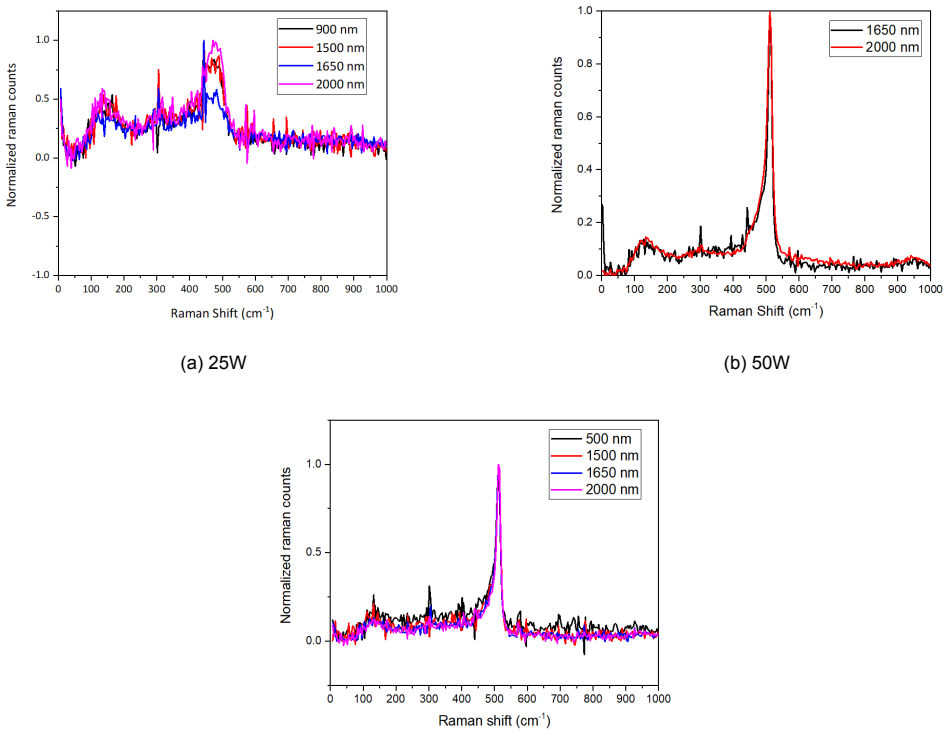

(a) 25W

(b) 50W

(c) 80W

Figure A.3: Standard range raman results measured using green laser: (a) 25W thickness series (b) 50W thickness series (c) 80W thickness series

to the deposition parameters in the aforementioned table 5.5. The aforementioned deposition of front and back contacts were deposited again as described. The crystalline p-i-n deposited on Asahi glass exhibited diode behaviour when measured under dark as shown in figure A.5. The quantum efficiency of the cell was also measured and the quantum efficiency v/s wavelength graph obtained is as seen in figure A.6.

Even varying the substrate did not improve the cell significantly. Hence, another set of experiments were performed using Asahi and Al substrate. A varying silane flow rate series at 50W as explained in section 5.3 was performed. The cells were deposited in p-i-n(a) superstrate configuration. The deposition parameters are explained below in table A.1 and the silane flow rate varied from 3.1 sccm to 3.9 sccm. All the cells deposited were measured under dark and all of them were shunted. Even the EQE and reflectance measurements were insignificant.

Layer	Deposition time (s)	Temperature (°C)	Pressure (mbar)	Power (W)
p-layer	1800	300	2.2	12
n-layer	825	300	0.6	4
i-layer	3810	300	4	50

Table A.1: Silane flow rate series deposition parameters

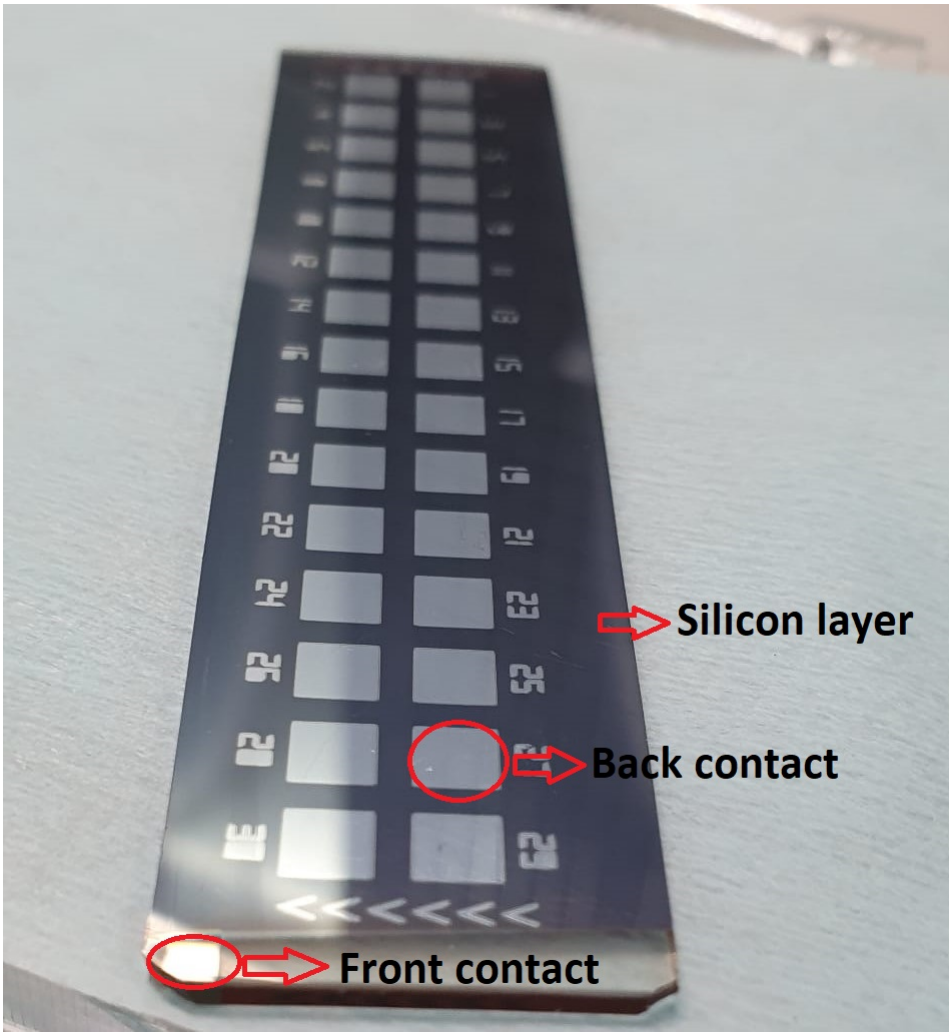

Figure A.4: Labelled image of a thin-film cell deposited on asahi glass

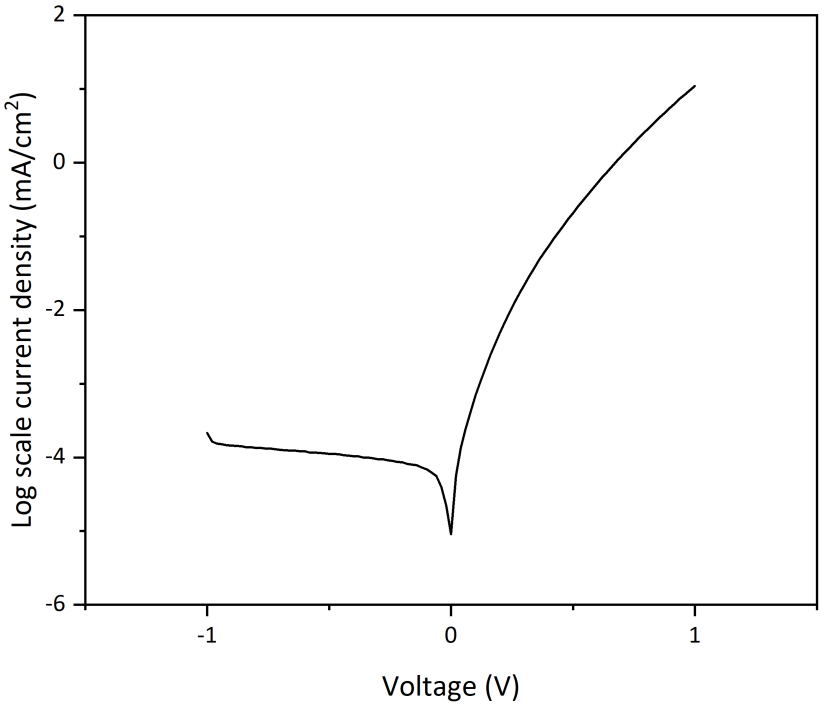

Figure A.5: log scale current density v/s voltage for p-i-n cell deposited on Asahi glass

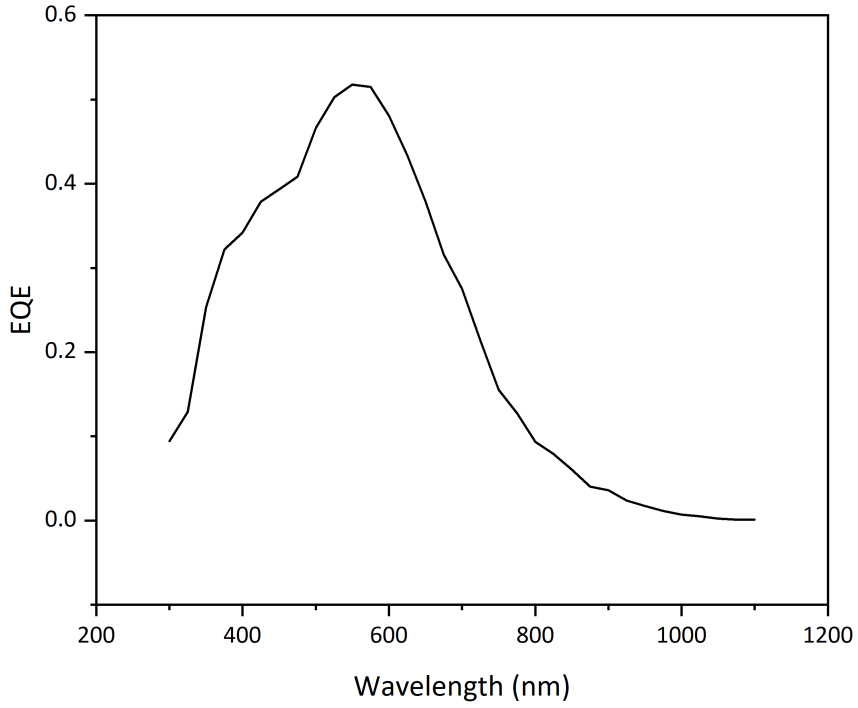

Figure A.6: EQE v/s wavelength of Asahi glass

Bibliography

[1] *Institute of analysis for global security*. [Online]. Available: http://www.iags.org/geopolitics.html (visited on 06/18/2021).

[2] *International renewable energy agency*. [Online]. Available: https://www.irena.org/solar (visited on 04/18/2021).

[3] *International renewable energy agency*. [Online]. Available: https://www.irena.org/Statistics/View-Data-by-Topic/Costs/Solar-Costs (visited on 04/18/2021).

[4] T. D. Lee and A. U. Ebong, *A review of thin film solar cell technologies and challenges*, 2017. DOI: https://doi.org/10.1016/j.rser.2016.12.028. [Online]. Available: https://www.sciencedirect.com/science/article/pii/S136403211631070X.

[5] *Advantages make thin film solar panels shine*. [Online]. Available: https://solartown.com/learning/solar-panels/advantages-make-thin-film-solar-panels-shine/ (visited on 06/06/2021).

[6] K. Jäger, J. Lenssen, P. Veltman, and E. Hamers, "Large-area production of highly efficient flexible light-weight thin-film silicon pv modules," Oct. 2013. DOI: 10.4229/28thEUPVSEC2013-3BO.5.5.

[7] H. S. BV, *Lp3 interconnection process*, 2019.

[8] A. Smets, K. Jäger, O. Isabella, R. van Swaaij, and M. Zeman, *Solar Energy: The physics and engineering of photovoltaic conversion, technologies and systems*, English. UIT Cambridge Limited, 2016, ISBN: 978-1-906860-32-5.

[9] *Overview and Classification | Physics in a Nutshell*. [Online]. Available: https://www.physics-in-a-nutshell.com/article/1/overview-and-classification (visited on 06/02/2021).

[10] L. Houben, M. Luysberg, P. Hapke, R. Carius, F. Finger, and H. Wagner, "Structural properties of microcrystalline silicon in the transition from highly crystalline to amorphous growth," *Philosophical Magazine A*, vol. 77, no. 6, pp. 1447–1460, 1998. DOI: 10.1080/01418619808214262. eprint: https://doi.org/10.1080/01418619808214262. [Online]. Available: https://doi.org/10.1080/01418619808214262.

[11] O. Vetterl, F. Finger, R. Carius, P. Hapke, L. Houben, O. Kluth, A. Lambertz, A. Mück, B. Rech, and H. Wagner, "Intrinsic microcrystalline silicon: A new material for photovoltaics," *Solar Energy Materials and Solar Cells*, vol. 62, no. 1, pp. 97–108, 2000, ISSN: 0927-0248. DOI: https://doi.org/10.1016/S0927-0248(99)00140-3.

[12] K. L. Chopra, P. D. Paulson, and V. Dutta, "Thin-film solar cells: An overview," *Progress in Photovoltaics: Research and Applications*, vol. 12, no. 2-3, pp. 69–92, 2004. DOI: https://doi.org/10.1002/pip.541. eprint: https://onlinelibrary.wiley.com/doi/pdf/10.1002/pip.541. [Online]. Available: https://onlinelibrary.wiley.com/doi/abs/10.1002/pip.541.

[13] E. Fortunato, D. Ginley, H. Hosono, and D. C. Paine, "Transparent conducting oxides for photovoltaics," *MRS Bulletin*, vol. 32, no. 3, pp. 242–247, Jan. 2007, ISSN: 08837694. DOI: 10.1557/mrs2007.29. [Online]. Available: www.mrs.org/bulletin.

[14] S. N. Agbo, "Growth and Characterization of Thin Film Nanocrystalline Silicon Materials and Solar Cells," Tech. Rep., Mar. 2012. [Online]. Available: https://repository.tudelft.nl/islandora/object/uuid:aa1f5549-c354-4030-8459-5086f41e2b19/datastream/OBJ.

[15] H. Tan, E. Moulin, F. Si, J.-W. Schüttauf, M. Stuckelberger, O. Isabella, F. Haug, C. Ballif, M. Zeman, and A. Smets, "Highly transparent modulated surface textured front electrodes for high-efficiency multijunction thin-film silicon solar cells," English, *Progress in Photovoltaics: research and applications*, vol. 23, no. 8, pp. 949–963, 2015, Harvest, ISSN: 1062-7995. DOI: 10.1002/pip.2639.

[16] S. Usui and M. Kikuchi, "Properties of heavily doped GDSi with low resistivity," *Journal of Non-Crystalline Solids*, vol. 34, no. 1, pp. 1–11, Aug. 1979, ISSN: 00223093. DOI: 10.1016/0022-3093(79)90002-4.

[17] *Cadmium telluride | department of energy*. [Online]. Available: https://www.energy.gov/eere/solar/cadmium-telluride (visited on 06/06/2021).

[18] S.-H. Wei, S. Zhang, and A. Zunger, "Effects of na on the electrical and structural properties of cuinse$_2$," *Journal of Applied Physics*, vol. 85, pp. 7214–7218, 1999.

[19] M. Nakamura, K. Yamaguchi, Y. Kimoto, Y. Yasaki, T. Kato, and H. Sugimoto, "Cd-free cu(in,ga)(se,s)2 thin-film solar cell with record efficiency of 23.35%," *IEEE Journal of Photovoltaics*, vol. 9, pp. 1863–1867, Sep. 2019. DOI: 10.1109/JPHOTOV.2019.2937218.

[20] A. Lambertz, F. Finger, R. E. Schropp, U. Rau, and V. Smirnov, "Preparation and measurement of highly efficient a-Si:H single junction solar cells and the advantages of μc-SiOx:H n-layers," *Progress in Photovoltaics: Research and Applications*, vol. 23, no. 8, pp. 939–948, Aug. 2015, ISSN: 1099159X. DOI: 10.1002/pip.2629. [Online]. Available: https://onlinelibrary-wiley-com.tudelft.idm.oclc.org/doi/full/10.1002/pip.2629%20https://onlinelibrary-wiley-com.tudelft.idm.oclc.org/doi/abs/10.1002/pip.2629%20https://onlinelibrary-wiley-com.tudelft.idm.oclc.org/doi/10.1002/pip.2629.

[21] P. Torres, J. Meier, M. Goetz, N. Beck, U. Kroll, H. Keppner, and A. Shah, "Microcrystalline silicon solar cells at higher deposition rates by the vhf-gd," *Mater. Res. Soc. Symp. Proc.*, vol. 452, Jan. 2011. DOI: 10.1557/PROC-452-883.

[22] F. Meillaud, M. Boccard, G. Bugnon, M. Despeisse, S. Hänni, F. J. Haug, J. Persoz, J. W. Schüttauf, M. Stuckelberger, and C. Ballif, *Recent advances and remaining challenges in thin-film silicon photovoltaic technology*, Sep. 2015. DOI: 10.1016/j.mattod.2015.03.002.

[23] R. v. S. Arno Smets, *Et4377: Photovoltaic technologies: State-of-the-art thin-film si technology - part 2*, https://brightspace.tudelft.nl/d2l/le/content/197100/viewContent/1595033/View, 2020.

[24] S. B. Nawaratne, "Nanocrystalline silicon solar cells on flexible al substrates nanocrystalline silicon solar cells on flexible," no. May, 2020.

[25] P. M. Martin, "Handbook of Deposition Technologies for Films and Coatings : Science, Applications and Technology.," p. 931, 2009.

[26] N. K. Jain, M. Sawant, and S. H. Nikam, "Metal Deposition: Plasma-Based Processes," *Encyclopedia of Plasma Technology*, no. September 2020, pp. 722–740, 2017. DOI: 10.1081/e-eplt-120053919.

[27] A. Bleakie and D. Djurdjanovic, "Dynamic Feature Monitoring Technique Applied to Thin Film Deposition Processes in an Industrial PECVD Tool," *ASME 2011 International Manufacturing Science and Engineering Conference, MSEC 2011*, vol. 2, pp. 215–224, Sep. 2011. DOI: 10.1115/MSEC2011-50041.

[28] A. Gordijn, "Microcrystalline silicon for thin-film solar cells," 2005.

[29] P. Mondal and D. Das, "Preferential (220) crystalline growth in nanocrystalline silicon films from 27.12 mhz sih4 plasma for applications in solar cells," *RSC Adv.*, vol. 5, pp. 54 011–54 018, 67 2015. DOI: 10.1039/C5RA07781H. [Online]. Available: http://dx.doi.org/10.1039/C5RA07781H.

[30] N. Jain, M. Sawant, S. Nikam, and S. Jhavar, "Metal deposition: Plasma-based processes," in. Jan. 2016, p. 19. DOI: 10.1081/E-EPLT-120053919.

[31] *Charles Coloumb laboratoire*. [Online]. Available: https://coulomb.umontpellier.fr/RF-magnetron-sputtering?lang=fr (visited on 06/17/2021).

[32] P. Babal, "Doped nanocrystalline silicon oxide for use as (intermediate) reflecting layers in thin-film silicon solar cells," *Ph.D. Thesis, Delft University of Technology, The Netherlands*, 2014. [Online]. Available: https://repository.tudelft.nl/islandora/object/uuid%5C%3A448b63f4-2128-409e-bbd8-866e720116ed.

[33] *Angstorm engineering*. [Online]. Available: https://angstromengineering.com/tech/resistive-thermal-evaporation/aluminum-evaporation/ (visited on 06/17/2021).

[34] T. Deschaines, J. Hodkiewicz, and P. Henson, "Characterization of amorphous and microcrystalline silicon using raman spectroscopy," 2009.

[35] A. H. M. Smets, T. Matsui, and M. Kondo, "Infrared analysis of the bulk silicon-hydrogen bonds as an optimization tool for high-rate deposition of microcrystalline silicon solar cells," 2008. DOI: 10.1063/1.2837536.

[36] C. Smit, R. A. C. M. M. Van Swaaij, H. Donker, A. M. H. N. Petit, W. M. M. Kessels, and M. C. M. Van De Sanden, "Determining the material structure of microcrystalline silicon from raman spectra articles you may be interested in," *Journal of Applied Physics*, vol. 94, p. 3582, 2003. DOI: 10.1063/1.1596364. [Online]. Available: https://doi.org/10.1063/1.1596364.

[37] *Scanning Electron Microscopy (SEM)*. [Online]. Available: https://serc.carleton.edu/research_education/geochemsheets/techniques/SEM.html (visited on 06/06/2021).

[38] *How do electron microscopes work? - Explain that Stuff*. [Online]. Available: https://www.explainthatstuff.com/electronmicroscopes.html (visited on 06/17/2021).

[39] W. Ananda, "External quantum efficiency measurement of solar cell," *QiR 2017 - 2017 15th International Conference on Quality in Research (QiR): International Symposium on Electrical and Computer Engineering*, vol. 2017-December, pp. 450–456, Dec. 2017. DOI: 10.1109/QIR.2017.8168528.

[40] T. Matsui, M. Tsukiji, H. Saika, T. Toyama, and H. Okamoto, "Influence of substrate texture on microstructure and photovoltaic performances of thin film polycrystalline silicon solar cells," *Journal of Non-Crystalline Solids*, vol. 299-302, no. PART 2, pp. 1152–1156, Apr. 2002. DOI: 10.1016/S0022-3093(01)01083-3.

[41] *Integrating Sphere Fundamentals and Applications*. [Online]. Available: https://www.newport.com/t/integrating-sphere-fundamentals-and-applications (visited on 06/11/2021).

[42] G. Padmakumar, "Fabrication analysis of a-si:h/µc-si:h tandem solar cell on flexible aluminium substrates," no. August, 2021.